DISS. ETH NO. 18560

Mesoscopic Cavity QED with a Single Quantum Dot

A dissertation submitted to

ETH ZURICH

for the degree of

Doctor of Sciences

presented by

Martin Winger

Dipl. Phys. ETH
ETH Zürich

born 24th of September 1982

citizen of Austria

accepted on the recommendation of:

Prof. Dr. Ataç Imamoğlu, examiner
Prof. Dr. Vincenzo Savona, co-examiner

2009

To my parents

Nature uses only the longest threads to weave her patterns, so that each small piece of her fabric reveals the organization of the entire tapestry.

Richard P. Feynman

Summary

This dissertation investigates phenomena of cavity quantum electrodynamics using a system in which a single self-assembled InAs quantum dot (QD) is coupled to the fundamental mode of a photonic crystal resonator. In contrast to clean atomic-physics realizations of cavity QED, this system is embedded in a complex solid-state environment, which in consequence leads to novel effects.

This thesis demonstrates the coupling of photonic crystal cavities to single quantum dots in a fully deterministic fashion. An atomic force microscope is used to map the position of the QDs on the semiconductor chip. Based on this information, cavities are fabricated around the QDs to ensure maximal overlap of the emitter with the cavity. For the in-situ control of the cavity wavelength a cryogenic gas adsorption technique is implemented. The investigation of the system by photoluminescence spectroscopy reveals that the system obeys the conditions of the strong coupling regime. The QD-cavity system displays the expected quantum anharmonic behavior characteristic of a two-level emitter strongly coupled to a cavity mode.

Studying the strong coupling behavior of various QD transitions in photoluminescence, the excitonic fine structure of the QD states is investigated. It is demonstrated that the interaction with the cavity mode is a useful spectroscopic tool for the investigation of basic QD properties. In particular, the technique reveals a novel coupling mechanism between dark and bright exciton configurations that is mediated by the combined action of nuclear spins and the confined light field.

Cavity modes containing QDs exhibit strong emission in photoluminescence even if the cavity mode is far detuned from any discrete optical transition of the QD. Here, we unambiguously demonstrate that this cavity-feeding effect can be related to the presence of a single QD in the cavity. A full model for off-resonant cavity emission is developed, in which the mesoscopic nature of QD confinement plays a central role in explaining the experiments. Using pump-power dependent photoluminescence spectroscopy and photon-correlation techniques, we explain the origin of cavity feeding: cavity mode excitation arises from QD states containing multiple electron-hole pairs that exhibit strong many-body interactions with the surrounding bulk system. Our model accounts for both the occurrence of off-resonant cavity emission and the surprising photon-correlation signatures found experimentally. Moreover, for small detunings we find that cavity feeding via acoustic phonons plays a key role.

Finally, this work implements a novel resonant spectroscopy technique for more refined optical investigation of our cavity-QED system. In a first experiment, vacuum Rabi splittings for several QD transitions are observed. However, the presence of an uncoupled cavity peak on resonance opens up new questions and hints at new and hitherto unexplored phenomena of solid-state cavity QED.

Zusammenfassung

Diese Dissertation untersucht Effekte der Resonator-Quantenelektrodynamik anhand eines Systems, in welchem ein einzelner selbst-organisierter InAs-Quantenpunkt an die fundamentale Schwingungsmode eines photonischen Kristallresonators koppelt. Im Gegensatz zu sauberen Implementationen in der Atomphysik ist dieses System in eine komplexe Festkörperumgebung eingebettet, wodurch sich neuartige physikalische Effekte ergeben.

Diese Arbeit demonstriert die vollständig deterministische Kopplung photonischer Kristallresonatoren an einzelne Quantenpunkte. Mithilfe eines Rasterkraftmikroskops lassen sich die exakten Positionen der Quantenpunkte auf dem Halbleiterchip bestimmen. Ausgehend von den extrahierten Koordinaten werden die Resonatoren um die Quantenpunkte so positioniert, dass sich ein maximaler Überlapp zwischen dem Resonatorfeld und dem Quantenpunkt ergibt. Um im Experiment die Wellenlänge des Resonatorfeldes an die optischen Übergänge des Quantenpunktes anzupassen, wurde ein Verfahren entwickelt, das auf kryogener Gasadsorption basiert. Die Untersuchung des Quantenpunkt-Resonator-Systems mittels Photolumineszenz-Spektroskopie zeigt, dass das System die Kriterien der starken Emitter-Resonator-Kopplung erfüllt. Darüber hinaus weist das Emitter-Resonator-System das charakteristische anharmonische Verhalten eines Zwei-Niveau Emitters auf, das an einen Resonator koppelt.

Die Untersuchung der Resonator-Emissionsspektren verschiedener Übergänge des Quantenpunktes erlaubt zudem die Untersuchung der Feinstruktur der Exzitonen-Zustände. Es wird gezeigt, dass die Wechselwirkung mit dem Resonatorfeld ein nützliches spektroskopisches Hilfsmittel zur Untersuchung der Eigenschaften des Quantenpunkts darstellt. Insbesondere erlaubt uns diese Technik, einen neuartigen Kopplungsmechanismus zwischen exzitonischen Hell- und Dunkelzuständen zu identifizieren, welcher durch die gemeinsame Wechselwirkung mit den Kernspins und dem Resonatorfeld zustande kommt.

Hohlraumresonatoren mit integrierten Quantenpunkten weisen starke Emission in Photolumineszenz auf, selbst wenn der Resonator weit von den optischen Übergängen des Quantenpunkts verstimmt ist. In dieser Arbeit wird gezeigt, dass dieser Effekt durch die Präsenz lediglich eines einzelnen Quantenpunktes zustande kommt. Zudem wird ein vollständiges Modell zur Erklärung dieses Effekts entwickelt, in welchem die mesoskopische Struktur des Quantenpunktpotenzials eine wesentliche Rolle spielt. Mithilfe von Photolumineszenz-Spektroskopie in Abhängigkeit der Pumpleistung und Photonen-Korrelations-Messungen, wird das Auftreten der weit verstimmten Resonatorlumineszenz mit Zuständen in Verbindung gebracht, in welchen der Quantenpunkt mehrere Elektron-Loch-Paare enthält, die ihrerseits starken Wechselwirkungen mit dem umgebenden Festkörpersystem unterliegen. Das vorgestellte Modell erklärt sowohl das Auftreten der nicht-resonanten Resonatorlumineszenz als auch die experimentell beobachteten nicht-intuitiven Quantenkorrelationen

der Photonen. Ausserdem zeigt sich, dass für kleine Verstimmungen die Wechselwirkung mit akustischen Gitterschwingungen eine entscheidende Rolle für die nichtresonante Resonatorlumineszenz spielt.

Schliesslich wird in dieser Arbeit ein neuartiges Verfahren entwickelt, das die resonante Spektroskopie der hier vorgestellten Systeme zum Ziel hat. In einem ersten Experiment wurde das Vakuum-Rabi-Splitting verschiedener Quantenpunkt-Übergänge untersucht. Das unerwartete Auftreten der ungekoppelten Resonatormode wirft neue Fragen auf und zeugt von neuen, bisher unbekannten Phänomenen in der Festkörper-basierten Resonator-Quantenelektrodynamik.

Contents

Summary v

Zusammenfassung vii

Contents ix

Abbreviations xi

1. Introduction 1

2. Solid State Cavity Quantum Electrodynamics 5
- 2.1. Cavity Quantum Electrodynamics . . . 5
  - 2.1.1. The Jaynes Cummings Model . . . 5
  - 2.1.2. Weak and Strong Coupling . . . 8
- 2.2. The Emitter Part: Self-Assembled Quantum Dots . . . 11
  - 2.2.1. Quantum Dot Growth . . . 11
  - 2.2.2. Quantum Dot Level Structure . . . 12
  - 2.2.3. Exciton States . . . 15
- 2.3. The Cavity Part: Photonic Crystal Microcavities . . . 18
  - 2.3.1. General Overview of Typical Microcavities . . . 18
  - 2.3.2. Photonic Crystal Cavities . . . 20
  - 2.3.3. Design and Fabrication . . . 21

3. Experimental Methods 25
- 3.1. Photoluminescence Spectroscopy . . . 25
  - 3.1.1. Excitation and Intra-Dot Relaxation . . . 27
  - 3.1.2. A Typical Quantum Dot PL Spectrum . . . 27
  - 3.1.3. Time-Correlated Single-Photon Counting . . . 29
  - 3.1.4. Photon Auto-Correlation Measurements . . . 31
  - 3.1.5. Photon Cross-Correlation Measurements . . . 32
- 3.2. Experimental Setup . . . 34
  - 3.2.1. Cryogenics . . . 34
  - 3.2.2. Confocal microscopy . . . 35
  - 3.2.3. Detection Apparatus and Time-Correlated Measurements . . . 36

4. Implementation of a Single QD-Cavity System 39
- 4.1. Spatial Positioning . . . 39
- 4.2. Spectral Tuning . . . 45
  - 4.2.1. Digital Etching . . . 46
  - 4.2.2. Tuning by Gas Adsorption . . . 47

5. Observation of Strong Coupling 51
5.1. Vacuum Rabi Splitting . . . 52
5.2. Modification of Lifetime . . . 55
5.3. Quantum Nature . . . 57

6. Cavity QED as a Tool for Quantum Dot Spectroscopy 61
6.1. Strong-Coupling PL for Different Excitons . . . 62
6.2. Dark Exciton coupling . . . 66
6.3. Influence of Angular Misalignment . . . 68

7. Cavity Feeding - The Effect of Off-Resonance Cavity Mode Emission 71
7.1. Phenomenology of Cavity Feeding . . . 71
  7.1.1. Off-Resonant PL Spectra . . . 71
  7.1.2. Photon Correlation Measurements . . . 73
7.2. A Model for Cavity Feeding . . . 75
  7.2.1. General Considerations . . . 75
  7.2.2. Theoretical Modeling . . . 82
  7.2.3. Photon Correlations . . . 84
7.3. Cavity Feeding Mediated by Acoustic Phonons . . . 88
  7.3.1. Photon Correlations in the Phonon-Feeding Regime . . . 94

8. Resonant Scattering Spectroscopy 97
8.1. Reflection Spectrum of a PC Cavity . . . 98
8.2. Crossed-Polarization Resonant Scattering . . . 100
8.3. Observation of Vacuum Rabi Splitting . . . 101
8.4. Broadband Resonant Scattering . . . 105

9. Conclusion and Outlook 109

A. Optical Setup A

Bibliography I

List of Publications XIII

Acknowledgements XV

Curriculum Vitae XVII

List of Figures XIX

Index XXI

Abbreviations

a	Photonic crystal lattice constant
n	Index of refraction
r	Photonic crystal hole radius
t	Photonic crystal membrane thickness
δ	Fine-structure splitting of the X^0
δ_0	Bright-dark splitting of the X^0
λ_{cav}	Cavity mode wavelength
λ_{ex}	Excitation wavelength in PL
λ_{x}	Exciton wavelength
AFM	Atomic force microscope
APD	Avalanche photodiode
FDTD	Finite difference time domain
HBT	Hanbury-Brown Twiss
PC	Photonic crystal
PL	Photoluminescence
P_{ex}	Excitation power on sample surface
P_{sat}	Saturation power of the QD
Q	Cavity quality factor
QD	Quantum dot
RS	Resonant scattering
SEM	Scanning electron microscope
SK	Stranski-Krastanow
SPCM	Single-photon counting module
TCSPC	Time-correlated single photon counting
V_{eff}	Cavity mode effective mode volume
X^0	Neutral exciton
XX^0	Biexciton
X^{1+}	Single positively charged exciton
X^{1-}	Single negatively charged exciton

$c = 299458792$ m/s	Speed of light
$h = 4.13566733$ μeV ns	Planck's constant
$\hbar = 0.65821189$ μeV ns	reduced Planck's constant
$\epsilon_0 = 8.85418781762 \cdot 10^{-12}$ As/Vm	permittivity of vacuum

GaAs	Gallium arsenide
InAs	Indium arsenide
AlGaAs	Aluminium gallium arsenide
N_2	Nitrogen

1. Introduction

The field of cavity quantum electrodynamics (cavity QED) studies the quantum mechanical interaction of emitters with the electromagnetic field in a cavity [1–3]. At its heart lies the description of experiments in which the quantized nature of the field becomes important, e.g. under circumstances where the system dynamics changes upon addition or removal of only a single photon. The role of the cavity lies in the enhancement of the coupling between emitter and field, resulting in a significant modification of the radiative emitter dynamics. Dependent on the balance between the coherent emitter-cavity coupling g and the cavity loss rate κ, relaxation of the emitter can be enhanced and can ultimately become reversible in the strong-coupling regime: here, the energy oscillates back and forth between emitter and cavity in a coherent way. Besides being a test bed for fundamental properties of quantum mechanics, cavity QED also provides a promising route towards the implementation of several key quantum information tasks, like the realization of a coherent atom-photon interface [4], or the implementation of a universal scheme for quantum computation [5].

The most fundamental system of cavity QED consists of a two-level atom coupled to a single mode of the quantized electromagnetic field inside an optical cavity. The main challenge in experimentally observing cavity QED phenomena lies in the construction of a system in which the coherent coupling strength g becomes comparable to or larger than the decoherence rates of the system. Typically, this requires the design of cavities with substantial quality factors Q, but at the same time small mode volume V_{eff}, since $g \propto V_{\text{eff}}^{-1/2}$. In the first landmark experiments, this was achieved by directing Rydberg atoms through a microwave cavity, resulting in vacuum Rabi oscillations between atomic states of different principal quantum number n [3]. With Rydberg atoms large oscillator strengths and thus large coupling constants g can be achieved. Moreover, typical transition energies lie in the microwave regime, where superconducting mirrors for the construction of cavities with extremely high Q are available. Besides proofing the basic principles of cavity QED, this system recently also allowed for the direct observation of quantum jumps between different photon number states in the cavity [6]. Further cavity QED experiments involved cesium atoms released from a magneto-optical trap that traverse the field of an optical cavity [7–9] or a Bose-Einstein condensate coupled to a cavity [10].

However, atom-based experiments typically rely on sophisticated cooling and trapping schemes in order to ensure good spatial alignment of the atom with the cavity mode, thus rendering the observation of cavity-QED effects using atoms a technically challenging task. With the advent both of solid-state based single emitters and monolithic microcavities, large efforts have been made to implement on-chip integrated cavity-QED systems in the solid state for which the complications arising from atomic motion are naturally avoided. In the microwave domain, this has been successfully demonstrated using superconducting qubits coupled to transmission-line resonators [11, 12].

In the optical frequency domain, one of the most promising systems for studying cavity QED in the solid state is provided by a self-assembled semiconductor quantum dot (QD) coupled to a microcavity. Due to their narrow emission lines and quasi-atom like behavior QDs are of great importance for solid-state based quantum optics. Moreover, since their optical emission shows close to perfect photon antibunching [13, 14], they can be regarded as single quantum emitters. As such, they have allowed for the conduction of key quantum optical experiments like the observation of Rabi oscillations [15] or the coherent manipulation of excitons [16]. The possibility of controlled QD charging with extra carriers [17] furthermore allows for the study of single electron [18, 19] or hole [20, 21] spins by optical means that exhibit ultra-long spin-coherence times [22]. Aimed at the implementation of single qubit gates, coherent spin control has been demonstrated in single QDs [23].

For performing cavity-QED experiments, a suitable cavity system has to be identified to which single QDs can be coupled. Although coupling to external Fabry-Pérot cavities is in principle possible [24], an on-chip cavity QED structure based on *integrated* microcavities is clearly desirable. The most common examples for such structures are micropillars, microdisks, or photonic-crystal defect cavities. In such structures, Purcell effect [25–27] and strong coupling have been observed [28–30], making them promising candidates for future applications of cavity QED.

In this work, we study a system made of a single QD coupled to the fundamental mode of a deterministically positioned photonic-crystal defect (PC) nanocavity. These cavities provide a promising platform for nano-optics since they confine light close to the fundamental limit while allowing for extraordinary high Q factors [31]. Moreover, the resonance frequency of these cavities can be tuned easily by etching or gas adsorption techniques [32–35].

This thesis is organized as follows: Chap. 2 sets the stage for the experiments presented in this work by giving an introduction to the basics of cavity QED (Sec. 2.1). Moreover, the fundamental physics of the building blocks used for the solid-state based cavity-QED device studied in this work are described. Sec. 2.2 gives an introduction to quantum dots and Sec. 2.3 discusses the basic features of photonic crystal defect microcavities.

Chapter 3 describes the experimental tools used for the investigation of our QD-cavity systems and their experimental implementation.

The implementation of a QD-cavity system is subject to two main technical challenges: on the one hand good relative alignment between the QD and the cavity is required, while on the other hand good spectral coupling between an optical transition of the QD and the field of the cavity mode is needed. Chapter 4 describes the procedures that allow for the reliable implementation of these features in our system.

The dynamics of the successfully implemented QD-cavity systems is analyzed in detail in Chap. 5. The fabricated devices operate in the strong-coupling regime of cavity QED and exhibit genuine quantum dynamics. Moreover, the fine structure of different excitonic transitions of the QD is analyzed using the coherent interaction with the cavity mode in Chap. 6.

A key feature of QD-based cavity-QED systems that has been discovered in the context of the work presented in Chap. 5 is the surprising and at the time entirely unexpected effect of efficient excitation of a cavity mode by means of only a single quantum dot even when the latter is far off-resonance from the cavity mode. The physical mechanisms behind this effect are elucidated further in Chap. 7.

Finally, Chap. 8 presents the implementation of resonant spectroscopy on QD-cavity systems - a key element for more involved quantum optical experiments in these systems.

2. Solid State Cavity Quantum Electrodynamics

The experimental system studied in this thesis is a solid state based cavity QED structure comprised of a single self-assembled InAs quantum dot coupled to the fundamental mode of a photonic crystal defect nanocavity. The aim of the current chapter is on the one hand to provide a basic introduction to the field of cavity QED, which is done in Sec. 2.1.1, and on the other hand to give an overview of the physics underlying the fundamental building blocks of the devices studied in this thesis. Section 2.2 discuses the physical properties of quantum dots, and Sec. 2.3.2 gives a brief account of the physics and technology behind photonic crystal defect microcavities.

2.1. Cavity Quantum Electrodynamics

2.1.1. The Jaynes Cummings Model

The goal of this chapter is the discussion of the dynamics of a single atom coupled to the electromagnetic field of an optical cavity, as schematically depicted in Fig. 2.1. We restrict our description to two internal states of the atom — the ground state $|g\rangle$ and an excited state $|e\rangle$ — and consider a single mode of the quantized intra-cavity electromagnetic field described by the annihilation operator $\hat{a}$. The free system Hamiltonian describing the atom and field degrees of freedom is given by

$$\hat{H}_0 = \hbar\omega_a\hat{\sigma}_+\hat{\sigma}_- + \hbar\omega_c\hat{a}^\dagger\hat{a}, \tag{2.1}$$

where $\hbar\omega_a$ is the atomic energy level spacing, $\omega_c/2\pi$ refers to the cavity mode resonance frequency, and $\hat{\sigma}_- = \hat{\sigma}_+^\dagger = |g\rangle\langle e|$ is the atomic lowering operator. The atom-field coupling is described in terms of an interaction Hamiltonian $\hat{H}_I$, such that the total system Hamiltonian reads

$$\hat{H} = \hat{H}_0 + \hat{H}_I. \tag{2.2}$$

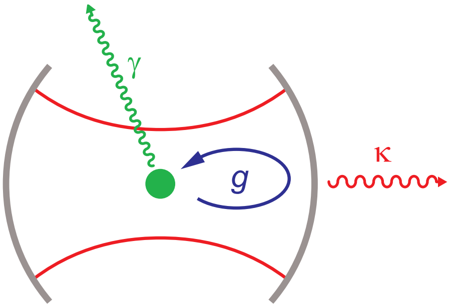

Figure 2.1.: The basic system of cavity QED. A single atom is coherently coupled to a cavity mode with interaction strength g. The system is subject to optical losses of the cavity mode (at rate κ) and spontaneous emission of the atom (at rate γ) into optical modes outside the cavity.

The interaction Hamiltonian $\hat{H}_I$ is in turn obtained from the standard $\boldsymbol{p} \cdot \boldsymbol{A}$ interaction Hamiltonian by making the Power-Zienau-Woolley transformation, and the dipole approximation, yielding the dipole interaction Hamiltonian [36, 37]

$$\hat{H}_I = -e\hat{\boldsymbol{r}} \cdot \hat{\boldsymbol{E}}(\boldsymbol{r}_a), \tag{2.3}$$

where e is the unit charge, $\hat{\boldsymbol{r}}$ is the position operator of the electron, and $\boldsymbol{r}_a$ is the location of the atom within the cavity. The operator of the electric field $\hat{\boldsymbol{E}}(\boldsymbol{r})$ is written in second quantized form as

$$\hat{\boldsymbol{E}}(\boldsymbol{r}) = \sqrt{\frac{\hbar\omega_c}{2\epsilon_0 n^2 V_{\text{eff}}}} \left(\boldsymbol{\varphi}(\boldsymbol{r})\hat{a} + \boldsymbol{\varphi}^*(\boldsymbol{r})\hat{a}^\dagger\right). \tag{2.4}$$

The square-root term in this expression refers to the electric field created by a single photon in the cavity and $\boldsymbol{\varphi}(\boldsymbol{r})$ denotes the spatial function of the cavity field which describes the local field polarization and the relative field amplitude. It is normalized such that $|\boldsymbol{\varphi}(\boldsymbol{r}_{\text{max}})| = 1$ at the location of the cavity field maximum $\boldsymbol{r}_{\text{max}}$, where the structure has a refractive index of n. The effective mode volume V_{eff} is defined as

$$V_{\text{eff}} = \frac{1}{n^2} \iiint n\left(\boldsymbol{r}\right)^2 \left|\boldsymbol{\varphi}(\boldsymbol{r})\right|^2 \mathrm{d}^3 r \tag{2.5}$$

and gives a measure of how strongly the light is confined within the cavity. V_{eff} corresponds to the volume of an equivalent cavity under Born-Von Karman periodic boundary conditions that would provide the same electric field per photon at the QD location [38]. Moreover, the dipole operator $e\hat{\boldsymbol{r}}$ can be expanded in the basis of the atomic eigenstates $\{|g\rangle, |e\rangle\}$ as

$$e\hat{\boldsymbol{r}} = \boldsymbol{d}_{\text{eg}} \left(|g\rangle\langle e| + |e\rangle\langle g|\right), \tag{2.6}$$

with the dipole matrix element $\boldsymbol{d}_{\text{eg}} = \langle e|e\hat{\boldsymbol{r}}|g\rangle$. By substituting Eq. (2.4) and Eq. (2.6) into Eq. (2.3) and by making the rotating wave approximation one arrives at the famous Jaynes-Cummings Hamiltonian [39]

$$\hat{H}_I = \hbar g \left(\hat{\sigma}_+ \hat{a} + \hat{\sigma}_- \hat{a}^\dagger\right), \tag{2.7}$$

where g denotes the coherent atom-field coupling given by

$$g = \sqrt{\frac{\omega_c}{2\hbar\epsilon_0 n^2 V_{\text{eff}}}}\, \boldsymbol{d}_{\text{eg}} \cdot \boldsymbol{\varphi}(\boldsymbol{r}_a). \tag{2.8}$$

From this relation it is clear that the strength of the coherent coupling between atom and field depends on their relative spatial alignment $\boldsymbol{\varphi}(\boldsymbol{r}_a)$, the alignment of the polarization axes of the atomic dipole and the cavity field, and the mode volume of the cavity. In particular, $g \propto V_{\text{eff}}^{-1/2}$, such that g can be increased by confining the cavity field to a small effective mode volume.

The total Hamiltonian $\hat{H}$ can readily be diagonalized to give the eigenenergies

$$\begin{aligned} \hbar\omega_o &= 0 \qquad (2.9) \\ \hbar\omega_n^{\pm} &= n\hbar\omega_c + \hbar\frac{\omega_c - \omega_a}{2} \pm \hbar\sqrt{ng^2 + \frac{(\omega_c - \omega_a)^2}{4}}, \qquad n \geq 1 \qquad (2.10) \end{aligned}$$

and the *polaritonic* eigenstates

$$\begin{aligned} |\Phi_o\rangle &= 0; \\ |\Phi_n^+\rangle &= \sin\theta_n|e, n-1\rangle + \cos\theta_n|g, n\rangle, \\ |\Phi_n^-\rangle &= \cos\theta_n|e, n-1\rangle - \sin\theta_n|g, n\rangle, \qquad n \geq 1 \end{aligned} \tag{2.11}$$

where the atom-field states are denoted as $|a, f\rangle = |\text{atom}\rangle \otimes |\text{field}\rangle$. Here the field can occupy any of the Fock-states $|n\rangle$ with $n \geq 0$, in which the cavity mode is populated by n photons. Clearly, the *polariton* states in Eq. (2.11) are hybridized (entangled) states of the atom-field system, with a mixing angle θ_n given by $\tan 2\theta_n = \frac{g\sqrt{n}}{\omega_c - \omega_a}$. This feature is particularly pronounced when the cavity is on resonance with the atomic transition, i.e. for $\omega_a = \omega_c$. In this case the system eigenstates

$$|\Phi_n^{\pm}\rangle = \frac{1}{\sqrt{2}}\left(|g, n\rangle \pm |e, n-1\rangle\right) \tag{2.12}$$

are maximally entangled atom-field states that for each n form a pair of energy levels split by $2\hbar g\sqrt{n}$.

This situation is schematically depicted in Fig. 2.2a-b for the lowest excitation manifold ($n = 1$). Resonant coupling of the atomic eigenstate $|e, 0_c\rangle$ to the field eigenstate $|g, 1_c\rangle$ (Fig. 2.2a) leads to the formation of two polaritons that show a *vacuum Rabi splitting* energy of $2\hbar g$ (Fig. 2.2b). This is in exact analogy to normal mode splitting induced by the dressing of an atomic transition by a strong laser beam. In contrast, here the splitting is induced by the electric field of only a single photon.

The occurrence of vacuum Rabi splitting on resonance leads to a distinct anti-crossing, when sweeping the cavity mode frequency across resonance with the atomic transition. Figure 2.2c shows the eigenenergies $\omega_1^{\pm}$ of the lowest polariton branch as a function of detuning between the cavity field and the atomic transition $\omega_c - \omega_a$. While for significant detuning the two eigenstates have predominantly cavity- or atom-like character, the two states get mixed on resonance, thereby forming the polariton states in Eq. (2.12).

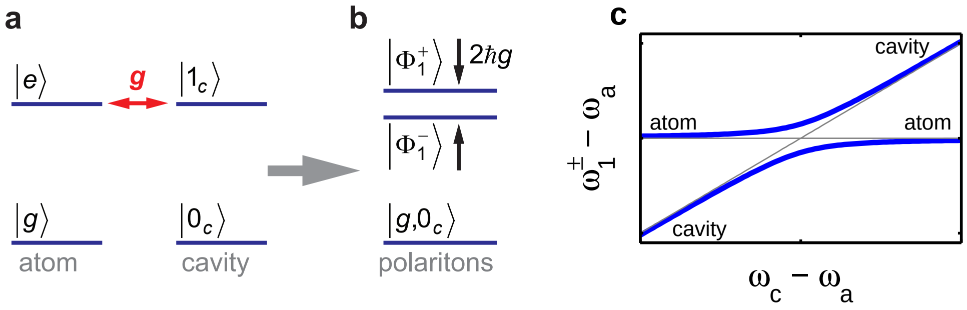

Figure 2.2.: System eigenstates on resonance. **a**, Eigenstates of the uncoupled system for $\omega_c = \omega_a$. **b**, Eigenstates of the coupled cavity system, showing the lowest polariton states $|\Phi_1^{\pm}\rangle$ split by $2\hbar g$. **c**, Calculated eigenfrequencies $\omega_1^{\pm}$ of the lowest polariton branches when tuning the cavity mode across resonance. On resonance a characteristic anticrossing occurs.

2.1.2. Weak and Strong Coupling

The Hamiltonian description in Eq. (2.7) is valid for a closed system that is not subject to any form of decoherence. In any real-world implementation however, dissipation obscures the ideal behavior presented above. The main loss mechanisms for an atom-cavity system are described by the relaxation rate of the atom due to spontaneous emission into electromagnetic field modes other than the cavity mode (γ) and the photon loss rate of the cavity mode (κ). The latter is linked to the quality-factor (Q factor) of the cavity via

$$\kappa = \frac{\omega_c}{Q} \tag{2.13}$$

and describes the exponential ring-down of the intra-cavity field intensity $I(t) = I_0 e^{-\kappa t}$. Depending on the balance between the coherent coupling rate g and the dissipation rates γ and κ the system is said to be in the *weak* or in the *strong coupling* regime. In the former case, g acts as a perturbation on the atom-cavity system, while in the latter case the coherent evolution g dominates over the incoherent losses κ, γ, such that the description of the system in terms of the dressed states presented in Sec. 2.1.1 is justified.

A mathematical treatment of the dissipative system can be obtained by using the master equation formalism, in which one considers a differential equation for the time evolution of the system density matrix $r\hat{h}o$:

$$\begin{aligned}\frac{d}{dt}\hat{\rho} = \frac{1}{i\hbar}[\hat{H}, \hat{\rho}] \quad &+ \quad \frac{\gamma}{2}\left(2\hat{\sigma}_-\hat{\rho}\hat{\sigma}_+ - \hat{\sigma}_+\hat{\sigma}_-\hat{\rho} - \hat{\rho}\hat{\sigma}_+\hat{\sigma}_-\right)\\ &+ \quad \frac{\kappa}{2}\left(2\hat{a}\hat{\rho}\hat{a}^\dagger - \hat{a}^\dagger\hat{a}\hat{\rho} - \hat{\rho}\hat{a}^\dagger\hat{a}\right)\\ &+ \quad \gamma_d\left(\hat{\sigma}_z\hat{\rho}\hat{\sigma}_z - \hat{\rho}\right).\end{aligned} \tag{2.14}$$

Here the last term on the right-hand side includes dephasing of the emitter at rate γ_d. In the following, we will restrict our discussion to the limit of zero dephasing

$\gamma_d = 0$, as this turns out to be a reasonable approximation for many experiments using quantum dots[1].

For the case of a simple two-level system coupled to a cavity mode in the weak excitation regime one can restrict the Hilbert space of the system to $\{|g,0\rangle, |e,0\rangle, |g,1\rangle\}$. In this case, Eq. (2.14) can be solved analytically [41] to yield the emission spectrum on resonance (i.e. for $\omega_c = \omega_a$)

$$S(\omega) \propto \left| \frac{\Omega_+ - \omega_a + i\frac{\kappa}{2}}{\omega - \Omega_+} - \frac{\Omega_- - \omega_a + i\frac{\kappa}{2}}{\omega - \Omega_-} \right|^2 , \tag{2.15}$$

with the complex eigen-frequencies

$$\Omega_\pm + i\frac{\Gamma_\pm}{2} = \omega_a - \frac{i}{4}(\kappa + \gamma) \pm \sqrt{g^2 - \left(\frac{\gamma - \kappa}{4}\right)^2} . \tag{2.16}$$

The distinction between the weak and the strong coupling regime can now be made by the sign of the expression in the square root in Eq. (2.16).

Weak Coupling The weak coupling regime, where $g < \gamma, \kappa$, is further divided into the *bad emitter* and the *bad cavity* regime, depending on which of the loss rates dominates. Typically, in QD-based systems the latter is realized, such that $\kappa \gg \gamma$. In this regime, the complex eigen-frequencies of the system are those of an atom-like state Ω_a and a cavity-like state Ω_c:

$$\Omega_a + i\Gamma_a/2 = \omega_a - i\left(\frac{\gamma}{2} + \frac{2g^2}{\kappa}\right) \tag{2.17}$$

$$\Omega_c + i\Gamma_c/2 = \omega_c - i\frac{\kappa}{2}. \tag{2.18}$$

From Eq. (2.17) it can be seen that the decay rate of the atom is modified to

$$\Gamma_a = \gamma\left(1 + \frac{4g^2}{\kappa\gamma}\right) = \gamma\,(1 + F_P) \tag{2.19}$$

with the *Purcell* factor $F_P = 4g^2/\kappa\gamma$. The net effect of the cavity is thus to increase the density of states of the electromagnetic field at the cavity resonance frequency, which leads to an increases of the atomic spontaneous emission rate — an effect known as the *Purcell effect*. The regime characterized by

$$\gamma \ll \frac{4g^2}{\kappa} \ll \kappa \tag{2.20}$$

is hence referred to as the *Purcell regime*. From the Wigner-Weisskopf theory of spontaneous emission [42] it follows that

$$\gamma = \frac{\omega_a^3}{3\pi\hbar\epsilon_0 c^3}\left(\boldsymbol{d}_{\mathrm{eg}} \cdot \boldsymbol{\varphi}(\boldsymbol{r}_a)\right)^2 . \tag{2.21}$$

Substituting this and Eq. (2.8) into Eq. (2.19) one obtains the relation

$$F_P = \frac{3}{4\pi}\frac{Q}{V}\left(\frac{\lambda}{n}\right)^3 , \tag{2.22}$$

i.e. the Purcell factor depends only on the cavity parameter $\frac{Q}{V}$, which in turn represents a figure of merit for achieving large Purcell enhancement [38, 41, 43].

---

[1] An experimental study of the role of polariton dephasing is given in [40].

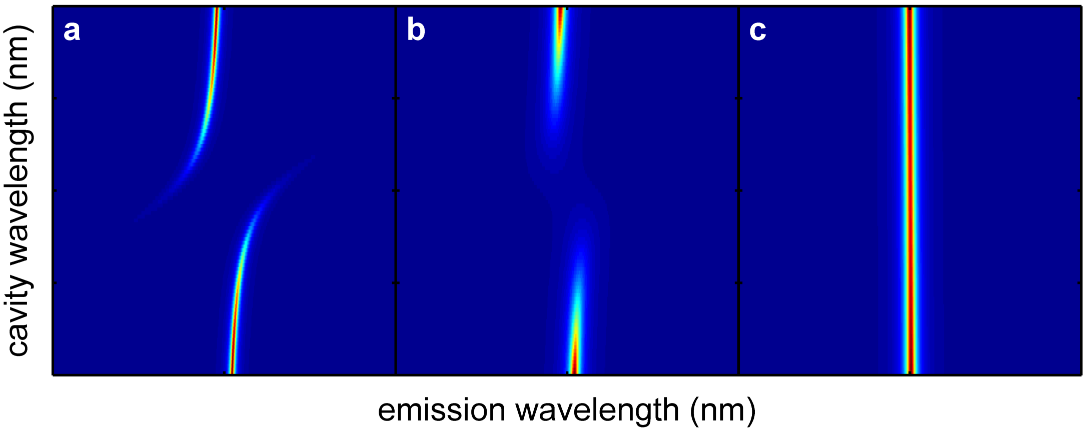

Figure 2.3.: Simulated PL spectra in the weak and the strong coupling regimes. Normalized to the atom eigenfrequency $\omega_a = 1$, the assumed system parameters are $g = 0.15$, $\gamma = 0.01$, $P = 0.001$, and $\kappa = 0.06$ (**a**), $\kappa = 0.6$ (**b**), and $\kappa = 6$ (**c**).

Strong Coupling For $g > |\gamma - \kappa|/4$ the emission spectrum of a weakly driven system consists of two lines separated by the polariton splitting

$$\Delta\omega_1 = 2\hbar\sqrt{g^2 - \left(\frac{\gamma-\kappa}{4}\right)^2}, \tag{2.23}$$

each having a linewidth of $(\gamma + \kappa)/2$. The effect of losses is thus to (a) slightly diminish the vacuum Rabi splitting and (b) to cause a finite linewidth of the polariton states. The calculated linewidth is intuitively clear from the nature of the polaritonic states $|\Phi_1^{\pm}\rangle$: having half atom and half cavity-like character, the states decay at a rate given by the arithmetic mean of the decay rates of each channel.

Since in the strong coupling regime the vacuum Rabi splitting exceeds the linewidth of the individual polaritonic states, a characteristic anticrossing — for a loss-free system shown in Fig. 2.2 — becomes visible in this regime. Figure 2.3 shows simulated[2] PL spectra of a two-level atom coupled to a cavity mode when the atomic degree of freedom is weakly excited by an incoherent pump at rate P[3] and the cavity mode frequency is swept across resonance with the atomic transition. While in Fig. 2.3a the system operates in the strong coupling regime with $\kappa = 0.4\,g$, Fig. 2.3b shows the situation of a larger cavity decay rate with $\kappa = 4\,g$, and in Fig. 2.3c the system is far in the weak coupling regime with $\kappa = 40\,g$. Clearly the qualitative behavior of the curves change when moving from weak to strong coupling: in the weak coupling regime the PL spectrum only shows the emission from the atomic transition and no obvious effect can be seen when the cavity is tuned across. In the strong coupling regime on the other hand, a distinct anticrossing appears, indicative of the formation of polaritons on resonance.

---

[2] The simulation relies on a time evolution of the master equation Eq.(2.14), which is accomplished by use of the *Quantum Optics and Computation Toolbox for MATLAB* [44].

[3] The incoherent pump is included by adding the Lindblad term $\frac{P}{2}\left(2\hat{\sigma}_+\hat{\rho}\hat{\sigma}_- - \hat{\sigma}_-\hat{\sigma}_+\hat{\rho} - \hat{\rho}\hat{\sigma}_-\hat{\sigma}_+\right)$ to the master equation Eq.(2.14).

As discussed previously, in order to enter the strong coupling regime, g has to exceed the loss rates γ and κ. From Eq. (2.8) it can be seen that $g \propto V_{\mathrm{eff}}^{-1/2}$, such that the figure of merit for a cavity to allow for strong coupling is $\frac{Q}{\sqrt{V}}$, thus demanding a cavity of small mode volume together with a high Q factor.

2.2. The Emitter Part: Self-Assembled Quantum Dots

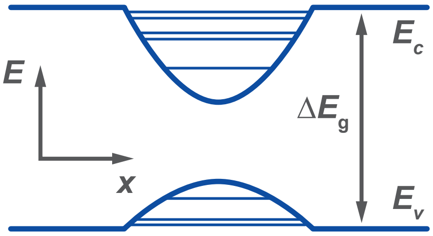

Figure 2.4.: QD level scheme showing the spatial variation of the conduction and valence band energies.

Self-assembled quantum dots provide a generic implementation of an atom-like emitter embedded in a solid-state environment and hence have received major attention in recent years.

Confinement of electrons and/or holes in low-dimensional semiconductor systems is achieved via an appropriate arrangement of materials having different bandgap energies. In the self-assembled QDs studied here, a region of Indium Arsenide (InAs) is embedded into a Gallium Arsenide (GaAs) host matrix. The bandgap energy of InAs ($\Delta E_{\mathrm{g}} = 0.36$ eV) is significantly smaller than that of GaAs ($\Delta E_{\mathrm{g}} = 1.43$ eV), such that the landscape of the conduction and valence bands created by the QD forms an effective attractive potential for the envelope part of the Bloch wavefunctions of both electrons and holes, as schematically indicated in Fig. 2.4. The resulting discrete states with wavefunctions strongly localized to the InAs region give rise to characteristic narrow optical transitions that resemble the emission spectra of real atoms - a feature reflected in the commonly used term *artificial atom*. This, together with the occurrence of close to perfect photon antibunching [45] makes self-assembled QDs one of the most prominent systems in solid-state quantum optics research.

2.2.1. Quantum Dot Growth

Although several attempts have been made to create quantum dots by lithographic means, the strongest carrier confinement interestingly arises in structures that form naturally in a strain-driven phase transition that was studied as early as 1939 by Stranski and von Krastanow [46]. The Stranski-Krastanow (SK) mechanism is a process that allows for elastic relaxation of a strained epitaxial layer formed when combining materials of different lattice constant. In the case of the InAs/GaAs material system, the lattice constant of InAs is $\sim 7\%$ larger than that of GaAs, such that a thin film of InAs grown on a GaAs substrate is under compressive strain. This situation is schematically illustrated in the top panel of Fig. 2.5. When continuing growth, after a certain critical thickness (~ 1.6 monolayers) the strain relaxes elastically by forming localized unstrained InAs islands superimposed on a rough *wetting layer* (middle panel of Fig. 2.5). Upon capping the islands with GaAs (bottom panel in Fig. 2.5), these islands form the QD [47] with typical lateral dimensions of $\sim$20 nm and a typical height of $\sim$5 nm. Naturally, the nucleation of

QDs in the Stranski-Krastanow transition occurs at random locations on the sample surface.

Growth of InAs and GaAs proceeds monolayer-by-monolayer using molecular beam epitaxy (MBE). For this technique, the sample is inserted into an ultrahigh-vacuum chamber and heated to a relatively high process temperature. Thin films then crystallize on the substrate surface by the adsorption of material from thermal-energy molecular or atomic beams formed of the constituent elements. The beam flux is determined by the temperature of the sources, which can in turn be used to steer the growth rate. Moreover, the molecular beams can easily be turned on and off by mechanical shutters in front of the sources.

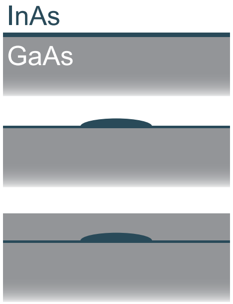

Figure 2.5.: SK growth

The MBE technique does not only allow for ultra-precise control of the grown layer thickness, but also provides the significant advantage of in-situ monitoring of the microscopic surface structure of the epitaxial layer during growth by using the *reflection high-energy electron diffraction* (RHEED) technique. A RHEED pattern is obtained by directing an electron beam to the sample surface at grazing incidence and by measuring the reflected beam on a phosphorescent screen. The RHEED diffraction pattern provides information on the surface structure and in particular allows for the determination of surface roughness. This enables in-situ monitoring of QD formation during growth [48].

The central emission energy of InAs/GaAs QDs grown in the Stranski-Krastanow mode lies in the mid-infrared with wavelengths typically larger than $\sim 1\,050$ nm. In this spectral region, Si-based photodetectors do not work, and InGaAs-based devices suffer from substantially higher noise levels than their Si-based counterparts. This is particularly true for CCD cameras and single-photon counting modules, which did not even exist for the corresponding emission window in the early days of QD research. In order to benefit from the advantages of Si-based optoelectronics, it is therefore desirable to shift the QD emission energy to the near infrared. This can be achieved by using the *partially covered islands* (PCI) technique that makes use of additional annealing steps during QD overgrowth [49]. After a few monolayers, the growth of the GaAs capping layer is interrupted, thus allowing for diffusion of the QD material. After a certain waiting time, the overgrowth is resumed, leaving a QD of reduced height. The shallower QD confinement leads to a confined ground state of higher energy, thus resulting in higher energy exciton transitions of the QD.

2.2.2. Quantum Dot Level Structure

InAs/GaAs QDs typically consist of $\sim 10^5$ atoms and exhibit an approximately lens-shaped material distribution that is distorted strongly due to material interdiffusion during annealing and overgrowth. Nonetheless, QDs exhibit unusually sharp optical transitions despite their rather complicated solid-state environment that gives rise to strain and lattice vibration effects. However, since the exact shape of the confinement potential is subject to strong variations from dot to dot and since the Coulomb interaction between carriers is significant, the ab-initio calculation of the QD level spectrum is in general a highly non-trivial task that demands for involved numerical techniques. Nevertheless, one can derive the basic symmetry

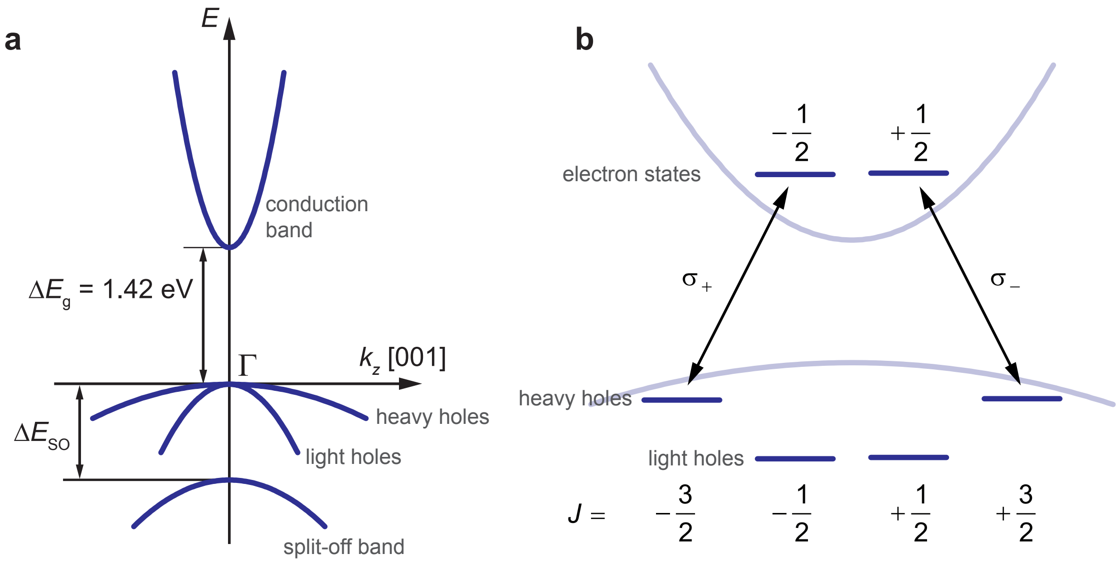

Figure 2.6.: QD-level structure. **a**, Band-structure of GaAs for electron propagation in the z ([001]) direction. **b**, QD single particle levels, hybridizing from the conduction- and valence-band states of GaAs. The circularly polarized optical transitions are indicated by the diagonal arrows.

principles of the confined QD states by relatively straightforward arguments from the band-structure of GaAs, which is schematically shown in Fig. 2.6a. GaAs is a direct semiconductor that crystallizes in the zincblende structure and has a bandgap energy of $\Delta E_{\mathrm{g}} = 1.43$ eV, which lies in the near infrared. Figure 2.6a shows a schematic of the GaAs band structure around the Γ point ($\boldsymbol{k} = 0$) for propagation in the [001] (z) direction (the typical growth direction). The band structure of InAs is qualitatively comparable to that of GaAs, yet with different values of the band splittings and curvatures. For small k_z the bands follow to a good approximation a parabolic dispersion relation, such that the carrier motion can be described in terms of an effective mass m^*. The lattice-periodic part of the conduction-band Bloch-wavefunction exhibits s-type symmetry, which results in two-fold spin-degeneracy of the conduction-band states with $(S, S_z) = (\frac{1}{2}, \pm\frac{1}{2})$. The valence band states hybridize from p-type tight binding orbitals and thus carry an angular momentum of $L = 1$ at $\boldsymbol{k} = 0$. Including spin, this results in the formation of states with total angular momentum $(J, J_z) = (\frac{3}{2}, \pm\frac{3}{2})$, $(\frac{3}{2}, \pm\frac{1}{2})$, and $(\frac{1}{2}, \pm\frac{1}{2})$. The strong spin-orbit interaction in GaAs leads to a splitting of the $J = \frac{3}{2}$ and the $J = \frac{1}{2}$ states into two distinct bands: the $J = \frac{1}{2}$ states are shifted by $E_{\mathrm{SO}} = 0.34$ eV to lower energy, thus forming the *split-off band*, as shown in Fig. 2.6a. The highest energy valence band states hence have an angular momentum of $J = \frac{3}{2}$ and are four-fold degenerate at $\boldsymbol{k} = 0$.

Theoretically, the band dispersion for $\boldsymbol{k} \neq 0$ around the Γ point can be described perturbatively in $\boldsymbol{k}\cdot\boldsymbol{p}$ theory using the *Luttinger Hamiltonian* [50]

$$\hat{H}=\gamma_1\frac{\hbar^2\hat{\boldsymbol{k}}^2}{2m_0}-\frac{\hbar^2}{9m_0}\sum_{i,j}\left[\gamma_3-\left(\gamma_3-\gamma_2\right)\delta_{ij}\right]\left[3\hat{k}_i\hat{k}_j-\delta_{ij}\hat{\boldsymbol{k}}^2\right]\left[\frac{3}{2}\left(\hat{J}_i\hat{J}_j+\hat{J}_j\hat{J}_i\right)-\delta_{ij}\hat{J}^2\right], \tag{2.24}$$

with the experimentally extracted Luttinger parameters γ_i. Typical values are {6.85, 2.1, 2.9} for GaAs and {19.67, 8.37, 9.29} for InAs. From this, one finds that the conduction band dispersion follows an isotropic parabolic dispersion with an effective mass of $m^*_{e,\mathrm{GaAs}}\approx 0.07\,m_e$ for GaAs and $m^*_{e,\mathrm{InAs}}\approx 0.16\,m_e$ for InAs. The situation for the valence band is slightly more complicated: along the growth direction (the crystalline [001] or z direction) it separates into two distinct bands of different curvature correponding to different effective masses, which depend on the z projection of the total angular momentum $|J_z|$: the states with $J_z=\pm\frac{3}{2}$ form the *heavy-hole band* with an effective mass of $m^*_{\mathrm{HH,InAs}}\approx 0.41\,m_e$ in InAs, while the $J_z=\pm\frac{1}{2}$ states form the *light hole band* with $m^*_{\mathrm{LH,InAs}}\approx 0.026\,m_e$. For propagation perpendicular to the growth direction, i.e. for wavevectors $\boldsymbol{k}_\perp$, the characters of the effective masses of the $J_z=\pm\frac{3}{2}$ and the $J_z=\pm\frac{1}{2}$ bands are interchanged.

When introducing one-dimensional carrier confinement by creating an InAs quantum well grown in the z direction, the degeneracy at $\boldsymbol{k}=0$ is lifted. Qualitatively this can be understood by considering a one-dimensional quantum well with infinitely high barriers, for which the ground state energy is given by

$$E_0=\frac{\hbar^2\pi^2}{2m^*a^2}, \tag{2.25}$$

where a is the width of the quantum well. From this it follows that different effective masses m^* result in different ground state energies, such that the heavy-hole band eventually has higher energy than the light-hole band at the Γ point. For the values of the effective masses given above this results in a heavy-light hole splitting on the order of $\sim$500 meV for a 5 nm thick quantum well. For in-plane propagation with $\boldsymbol{k}_\perp\neq 0$ on the other hand, the effective mass of the $J_z=\pm\frac{3}{2}$ band becomes smaller than that of the $J_z=\pm\frac{1}{2}$ band, such that there occurs a characteristic anticrossing of the heavy and light-hole bands for a finite $\boldsymbol{k}_\perp$. As a result, J_z is only a good quantum number exactly at the Γ point, as the heavy and light-hole bands attain mixed $J_z=\frac{3}{2}$ and $J_z=\frac{1}{2}$ character at the location of the anticrossing.

In a QD, the in-plane motion of electrons and hole is further confined, leading to the occurrence of discrete single-particle levels. In the QDs studied in this work, the confinement along the z direction is much stronger than the in-plane confinement, such that one typically models these QDs with a sharp step-wise potential in the growth direction and a weak parabolic confinement in-plane, as schematically indicated in Fig. 2.4. The QD single particle states can therefore be considered as superpositions of different $\boldsymbol{k}_\perp$ quantum well states, the wavefunction symmetries of which they retain. Figure 2.6b shows the relevant ground state single-particle levels of electrons and holes arising from these arguments. The conduction band ground state consists of the two degenerate states $|S_z=\pm\frac{1}{2}\rangle$, while the highest energy valence band states $|J_z=\pm\frac{3}{2}\rangle$ have predominantly heavy-hole character with a total angular momentum projection of $J_Z = \pm\frac{3}{2}$[4]. The light-hole states $|J_z = \pm\frac{1}{2}\rangle$ are split-off in energy by at least several meV and can usually be neglected in optical experiments.

The spin configurations of electrons and holes in this level structure give rise to characteristic selection rules for optical dipole transitions. The $|J_z = \pm\frac{3}{2}\rangle$ states can be coupled to the $|J_z = \pm\frac{1}{2}\rangle$ states via a photon of $\sigma_\pm$ circular polarization. However, these selection rules are lifted to a certain extent, since the anticrossing of the heavy and light-hole bands for $\boldsymbol{k}_\perp \neq 0$ results in a finite heavy-light-hole mixing: the quantum well valence band wavefunctions the QD states hybridize from have mixed $J_z = \pm\frac{3}{2}$ and $J_z = \pm\frac{1}{2}$ character for $\boldsymbol{k}_\perp \neq 0$, such that the QD heavy hole states attain a finite admixture of $|J_z = \pm\frac{1}{2}\rangle$ states, typically on the order of $\sim 10^{-3}$. As a result, the optical selection rules are lifted to a certain extent, which led to the experimental observation of *spin-pumping* [18].

The levels depicted in Fig. 2.6b correspond to the orbital ground states in the QD confinement potential and exhibit envelope wavefunctions of s-type symmetry. In addition there is a series of excited single particle states with p- or d-wave character of the in-plane wavefunction envelope (not shown in Fig. 2.6b). Due to the small QD height, excited states for propagation in the z direction are usually not confined.

2.2.3. Exciton States

Starting from the QD single particle levels described in Sec. 2.2.2, excitation of the system occurs by filling these states successively with electrons and holes. Configurations involving electron-hole pairs confined within the QD are then referred to as *excitons*, whereas it has to be mentioned that this terminology is not entirely correct in the sense of excitons in bulk semiconductor systems. In the latter an exciton corresponds to a bound state of an electron-hole pair that is formed due to the attractive Coulomb interaction between the two participating carriers, in contrast to a free electron-hole pair. In QDs however, binding of the two constituent carriers is enforced by the external confinement potential and not by the direct interaction between the carriers itself. The QD potential here provides the dominant energy scale. Nonetheless, on the energy scale of the exciton linewidth, the mutual Coulomb interactions between carriers in the QD are significant due to the small confinement length scale of $\sim$20 nm being in fact comparable to the bulk GaAs excitonic Bohr radius $a^*_{\mathrm{B,GaAs}} \sim 10$ nm. As a result, different charge configurations of QD excitons exhibit significantly different transition energies. The following section gives an overview of typical QD excitonic configurations.

The Neutral Exciton The most generic optically excited QD state is that of a neutral exciton (X^0), in which a single electron-hole pair is captured within the QD. From the single particle states shown in Fig. 2.6b one can see that both the electron and the hole have access to two possible spin configurations: the electron can occupy one of the states $|S_z = \pm\frac{1}{2}\rangle$, the hole one out of $|J_z = \pm\frac{3}{2}\rangle$. As a result, there are four different excitonic configurations, corresponding to the total angular

---

[4] Due to the anisotropic confinement potential of the QD, the total angular momentum J is not a good quantum number. On the other hand, J_z is conserved due to the in-plane rotational symmetry of the QD.

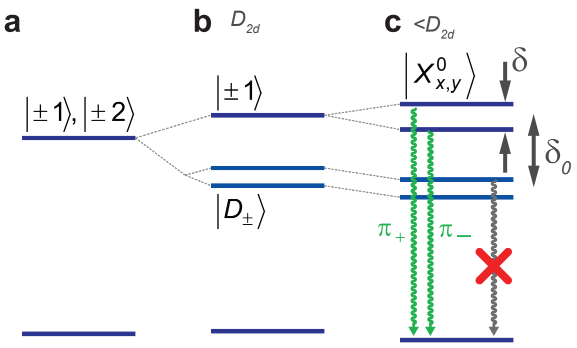

Figure 2.7.: X^0 level scheme. **a**, Degenerate exciton levels in the absence of electron-hole exchange interaction. **b**, Fine-structure splitting due to the combined effect of short- and long-range electron-hole exchange interaction for a QD exhibiting in-plane rotational symmetry D_{2d}. **c**, Fine-structure of a QD with broken in-plane rotational symmetry.

momentum projections $M = S_z + J_z = \pm 1, \pm 2$. The recombination of the $|\pm 2\rangle$ states requires an angular momentum transfer of $2\hbar$, such that they cannot undergo optical dipole transitions and are hence called *dark excitons*. The $|\pm 1\rangle$ states on the other hand can decay optically and give rise to the X^0 optical transition of the QD.

In the picture of the single-particle levels introduced in Fig. 2.6b, the four excitonic states $M = \pm 1, \pm 2$ are degenerate (Fig. 2.7a). However, due to interactions between the carriers, this degeneracy is lifted. The main interaction giving rise to this *fine structure* of the X^0 is the exchange interaction between the electron and the hole that couples their different spin configurations [51]. Generally, the exchange interaction can be divided into a short-range part that is sensitive to the symmetries of the underlying lattice, and into a long-range part that is sensitive to the geometry of the envelope part of the excitonic wavefunction. Due to the asymmetry of the underlying crystal, the effect of the short-range exchange interaction is (a) to introduce a splitting between the bright and the dark manifolds and (b) to lift the degeneracy of the two dark states $|\pm 2\rangle$, mixing them into the new eigenstates

$$|D_\pm\rangle = \frac{1}{\sqrt{2}} \left(|+2\rangle \pm |-2\rangle \right). \tag{2.26}$$

The long-range exchange interaction contributes to the splitting of the bright and the dark excitons, such that one typically measures a dark-bright splitting of $\delta_0 \sim 100$–$200\ \mu$eV (see Fig. 2.7b). Furthermore, it introduces a mixing of the bright excitons $|\pm 1\rangle$ in QDs for which the in-plane rotational symmetry D_{2d} is broken. Typically, the latter is the case for the QDs employed here, such that the mixed eigenstates of the X^0 are

$$|X^0_{x,y}\rangle = \frac{1}{\sqrt{2}} \left(|+1\rangle \pm |-1\rangle \right). \tag{2.27}$$

These states are split by the x-y or *fine-structure splitting* $\delta \sim 10$–$30\ \mu$eV and give rise to two transition dipoles oriented along orthogonal directions in the QD plane. Accordingly, the optical decay from the states $|X^0_{x,y}\rangle$ results in two emission lines of orthogonal linear polarization, split by δ (see Fig. 2.7c).

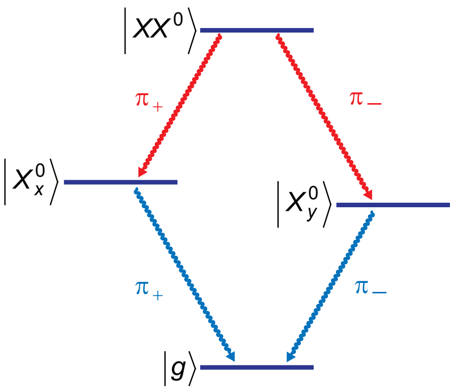

Figure 2.8.: XX^0 level scheme. Due to the double occupancy of both electron and hole QD states, the XX^0 forms a single quantum state. Decay occurs to the $|X^0_{\mathrm{x,y}}\rangle$ states of the X^0, such that the XX^0 and the X^0 together naturally form a radiative cascade ideally exhibiting perfect polarization correlation.

It has to be remarked that even in the case of perfect D_{2d} symmetry a finite fine-structure splitting of the X^0 remains, due to the coupling of the exciton to the piezoelectric potential that arises from the shear strain imposed by the lattice mismatch between InAs and GaAs [52, 53]. In light of this, the occurrence of a finite fine-structure splitting is rather the rule than the exception. Nonetheless, several works have recently presented methods to modify the magnitude and even the sign of the x-y splitting δ, either by changing the shape of the QD confinement potential using thermal annealing [52], or by applying a magnetic field [54].

The Neutral Biexciton The biexciton (XX^0) is a state in which two electron-hole pairs are present within the QD. Due to the complicated Coulomb-interaction between the four carriers involved, the XX^0 typically shows a net binding energy leading to a redshift of the XX^0 line of $\sim$1.5–2.5 nm with respect to the X^0. As in the XX^0 both the electrons and the holes occupy a spin-singlet state, this state does not have any degeneracy. However, since optical decay of an electron-hole pair here leaves another electron-hole pair behind, the final state of XX^0 decay is one of the fine-structure split states $|X^0_{x,y}\rangle$, such that the XX^0 and the X^0 form a radiative cascade as shown in Fig. 2.8. Accordingly, the XX^0 luminescence also exhibits a fine-structure splitting of δ.

In particular, the polarization of the X^0 and the XX^0 emission are nearly perfectly correlated. In the case of zero fine-structure splitting δ, XX^0 emission hence leads to the formation of a polarization entangled state of the emitted photons [55]. However, in the case of finite δ, the emission energy provides a which-path information that destroys the polarization entanglement [56]. Circumventing this problem with the goal of implementing an on-demand entangled-photon source has recently been demonstrated [52, 57, 58].

Trion States While the X^0 and the XX^0 states contain an equal number of electrons and holes, states carrying a net charge are referred to as *trion* states. In the case of a single electron (hole) resident in the QD, optical excitation can occur to the single negatively (positively) charged X^{1-} (X^{1+}) state. In the latter, two electrons (holes) occupy a spin-singlet state, such that these states are not subject to exchange interaction. The same is true for the single spin state of the electron (hole) in the ground state (Kramers degeneracy). Both the X^{1+} and the X^{1-} therefore result in a doubly degenerate — and therefore unpolarized — emission line[5].

Typically, the X^{1-} shows a characteristic redshift of ~ 3.5–4.5 nm with respect to the X^0, indicative of the fact that the binding energy between the additional electron and the hole dominates over the electron-electron repulsion. The situation is reverse for the X^{1+}, which in our samples typically shows a blueshift of ~ 0.5–2 nm with respect to the X^0. This can be interpreted by the Coulomb-interaction between the two holes overcoming the mutual electron-hole binding energy. While the X^{1-}–X^0 energy splitting is very reproducible from dot to dot, the shift between the X^{1+} and the X^0 is subject to much stronger variations for different dots [61].

The trion transitions are of great interest for the implementation of various quantum information tasks, as their ground states contain an isolated single spin that can be optically initialized [18], manipulated [23], and read-out [19] by means of optical transitions to the trion states. This provides a route towards the implementation of quantum information processing tasks using electron (or hole) spins confined in a QD.

Higher Charged Excitons While in the states discussed up to now only the lowest-energy states of the QD are populated, there is a large variety of excited states of the QD. When loading additional charges into the QD beyond the $X^{1\pm}$, higher excited single-particle levels of the QD are populated that correspond to orbital states exhibiting p-shell character perpendicular to the growth direction. Each of the higher charged states $X^{n\pm}$ exhibits a characteristic energy shift, the magnitude of which shows a behavior reminiscent of shell-filling following Hund's rules in real atoms [17]. Moreover, these transitions typically show a rich fine structure, due to the occurrence of different spin configurations both of the initial and final states [17, 62].

2.3. The Cavity Part: Photonic Crystal Microcavities

2.3.1. General Overview of Typical Microcavities

As discussed in Sec. 2.1.2, the figure of merit for achieving strong emitter-cavity coupling in a cavity QED system is given by $Q/\sqrt{V_{\text{eff}}}$. Hence, in order to enter the strong coupling regime the key technical challenge is the implementation of a cavity structure that confines photons for a sufficiently long time in order to increase the light-matter interaction, i.e. the Q factor of the cavity should be large. At the same time it is naturally desirable to reduce the mode volume V_{eff} as much as possible, in order to allow for a large coherent coupling strength g.

---

[5] Experimental studies revealing the different fine structures of the X^0 and the X^{1-} can be found in [59, 60]

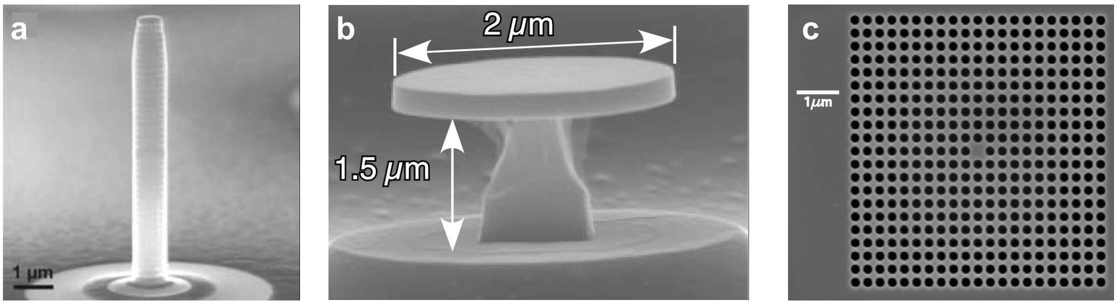

Figure 2.9.: SEM picture of different types of microcavities. **a**, SEM image of a micropillar cavity, taken from [29]. **b**, SEM image of a microdisk, taken from [30]. **c**, An S1 photonic crystal defect cavity, taken from [65].

Standard Fabry-Pérot cavities relying on two parallel highly reflective mirrors indeed do allow for large quality factors, however, typically the spatial arrangement of the mirrors results in an excessively large mode-volume. To circumvent this problem, several microcavity-designs have been developed for solid-state cavity QED in recent years that allow for a systematic reduction of V_{eff} and moreover have the benefit of being fully integrated in the sample chip. All these designs rely upon the reflection at dielectric interfaces formed between different semiconductor materials or between the GaAs matrix and ambient air or vacuum[6].

The most basic example of a semiconductor microcavity is a micropillar cavity (Fig. 2.9a), which essentially implements a microscopic version of a Fabry-Pérot type resonator: on a semiconductor substrate a parallel pair of distributed Bragg-reflectors (DBRs) is grown, spaced by a single cavity mode wavelength in order to form a one-dimensional cavity. Light confinement in the lateral dimensions is then achieved by etching a small pillar out of the DBR-structure. Typical mode-volumes lie in the range of $\sim 20\left(\frac{\lambda}{n}\right)^3$ with quality factors on the order of $Q \sim 10\,000 - 30\,000$ [66, 67]. A major drawback, however, is the lack of a practical tuning mechanism other than changing the refractive index of the entire structure by tuning the temperature.

An alternative cavity design that allows for even smaller mode-volumes are microdisc cavities, as shown in Fig. 2.9b. These structures consist of a small disc of semiconductor material residing on a small pillar that attaches them to the substrate. Light is confined in *whispering gallery modes*, which exist along the edge of the disk. As a result, the light travels in orbit-like modes around the microdisk. The term whispering gallery mode relates to so-called whispering galleries of certain buildings in which it is possible to perceive whispers at extraordinary distances. One of the most prominent examples for a whispering gallery is that of St. Paul's cathedral in London, first studied by the late Lord Rayleigh [68, 69]. An optical analog of this situation is typically fabricated in semiconductors with diameters on the order of a few μm and a thickness of ~ 200 nm. Microdisk cavities typically allow for Q factors of several tens of thousands and mode volumes on the order of ~ 10 cubic wavelengths [30, 70].

---

[6] A general review of different types of microcavities can be found in [63], a review of microcavities for semiconductor quantum optics can be found in [64].

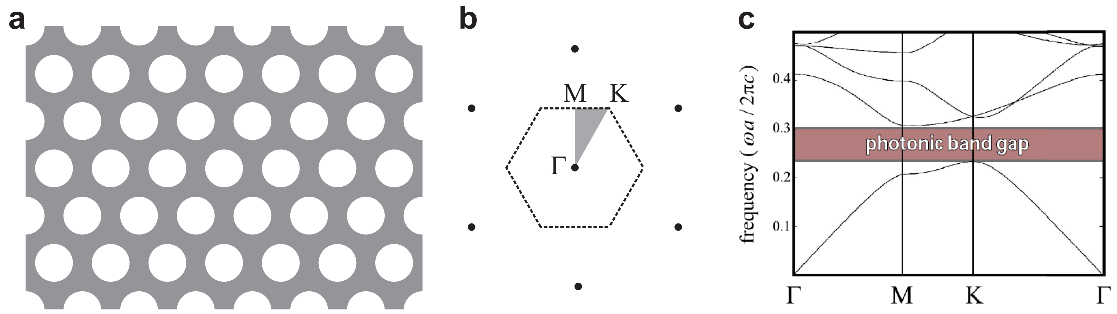

Figure 2.10.: Triangular-lattice photonic crystal. **a**, Schematic layout of a triangular-lattice PC. **b**, Reciprocal lattice of the triangular lattice showing the first Brillouin zone and the important symmetry points. **c**, Band diagram for light propagation in the triangular lattice PC along the path enclosed by the gray shaded area in **b** (Graph taken from [65]).

A more sophisticated cavity design principle is the one realized in *photonic crystal* (PC) defect cavities (Fig. 2.9c). A photonic crystal is a periodic arrangement of a dielectric that allows for strong modification of light propagation via distributed Bragg reflection. Interestingly, such structures even occur naturally, e.g. in the wings of certain butterflies where they result in shimmering and iridescent coloring [71]. Making use of the dispersive properties of photonic crystals, one can construct optical cavities that allow for light confinement at the fundamentally smallest scale in a dielectric environment, which is on the order of a single cubic reduced wavelength $(\lambda/n)^3$. Moreover — at least in principle — Q factors up to several millions can be achieved in such structures [31]. Section 2.3.2 discusses the basic operation principles of photonic crystal cavities in more detail.

2.3.2. Photonic Crystal Cavities

Photonic crystals were introduced to the field of nanophotonics in 1987 by two groundbreaking works discussing the role of light localization [72] and the modification of the spontaneous emission rate of an emitter in periodic dielectric structures [73]. They have been used for a large variety of experiments, including lasing [74–77], optical switches [78, 79], channel-drop filters [80], and cavity QED [26, 28, 81–83].

PCs are formed by a periodic modulation of the refractive index of the host material. A generic example of a 2D photonic crystal is shown in Fig. 2.10, where a triangular lattice of circularly shaped holes is drilled into a dielectric substrate such as GaAs. Maxwell's equation for a structure with spatially varying dielectric constant $\epsilon(\boldsymbol{r})$ can be transformed to an eigenvalue problem in the magnetic field $\boldsymbol{H}(\boldsymbol{r})$ [84]

$$\nabla \times \left(\frac{1}{\epsilon(\boldsymbol{r})} \nabla \times \boldsymbol{H}(\boldsymbol{r}) \right) = \left(\frac{\omega}{c} \right)^2 \boldsymbol{H}(\boldsymbol{r}). \tag{2.28}$$

The dielectric function $\epsilon\left(\boldsymbol{r}\right)$ here exhibits the lattice symmetry $\epsilon\left(\boldsymbol{r}+\boldsymbol{a}_i\right) = \epsilon\left(\boldsymbol{r}\right)$ for any lattice vector $\boldsymbol{a}_i$ of the PC. This symmetry relation hence also applies to the differential operator on the left hand side in Eq. (2.28). Therefore, in analogy to electronic propagation in a solid-state matrix, a Bloch-theorem can be formulated for the eigenvalue problem Eq. (2.28). This results in the formation of a band-structure for the dispersion relation $\omega(\boldsymbol{k})$ of light within the photonic crystal. Fig. 2.10c shows the dispersion relation of the 2D triangular-lattice PC depicted in Fig. 2.10a along the key symmetry lines of the inverse triangular lattice as shown in Fig. 2.10b. By appropriately choosing the lattice constant a and the hole radius r, one can ensure the presence of a *photonic bandgap* for light propagation within the PC, as indicated by the red shaded area in Fig. 2.10c.

The presence of the photonic bandgap prohibits the propagation of light having a frequency within the gap, which results in strong reflection for all in-plane $\boldsymbol{k}$ vectors. Acting like a highly reflective in-plane mirror, this structure hence suggests the construction of a cavity in a very straightforward way: introducing a defect into the crystal that is hence surrounded by a highly reflective two-dimensional mirror that prohibits light propagation away from the defect region results naturally in a cavity-like structure. Practically, this can either occur by changing the size or the shape of certain holes, or by entirely removing one or more holes. In perfect analogy to lattice defects in a semiconductor structure, the PC defect gives rise to a few discrete states within the photonic bandgap that have a field distribution strongly bound to the defect region [85]. These defect states hence comprise cavity modes that confine light propagation in two dimensions.

Extending this logic to the three-dimensional case, it is possible to reach full confinement of light for all propagation directions. Naturally, however, the fabrication of a three-dimensionally periodic dielectric structure at the nano-scale is subject to strong technological limitations. Typically one therefore circumvents this problem by defining a 2D PC in a thin membrane, such that total internal reflection (TIR) provides confinement in the third spatial direction. The interplay between in-plane DBR confinement and the out-of-plane confinement induced by TIR can then be tailored such as to provide for full three-dimensional confinement of light at least for one polarization setting.

In practice, there is a large variety of possible PC defect geometries. The most generic example is that of a single missing hole in a square lattice, usually referred to as an S1 cavity. An SEM image of such a structure can be seen in Fig. 2.9c. Similarly, an H1 cavity is given by a single missing hole in a triangular lattice. Although it provides an ultra-small mode volume on the order of $V_{\text{eff}} \sim \left(\frac{\lambda}{n}\right)^3$ the use of this cavity for strong-coupling cavity QED is rather limited, since it only supports an intrinsic Q-factor of several hundred [65]. A more refined design is that of an L3 cavity, in which a linear defect of three missing holes is introduced into a triangular PC. Figure 2.11a shows an SEM image of an L3 cavity fabricated in a GaAs membrane, taken from [65]. The theoretical Q factor of this structure is $\sim$4 000, however, after a few slight modifications to the holes closest to the defect along the L3 line, a theoretical Q factor of $\sim 300\,000$ can be achieved, while maintaining an ultra-low mode volume of $V_{\text{eff}} \sim 0.7 \left(\frac{\lambda}{n}\right)^3$ [86].

2.3.3. Design and Fabrication

The design of PC cavity structures typically relies upon the numerical solution of Maxwell's equations for the given dielectric structure defined by the spatially vary-

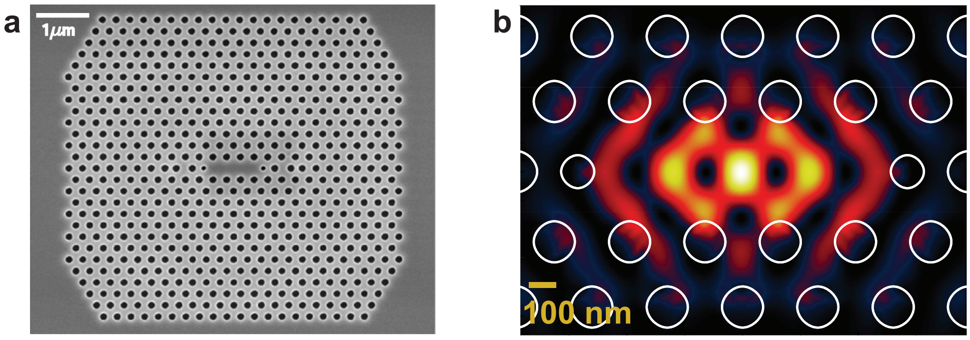

Figure 2.11.: The L3 microcavity. **a**, SEM picture of an L3 cavity fabricated in a GaAs membrane. **b**, Electric field distribution of the fundamental L3 cavity mode showing the spatial variation of the cavity electric field intensity $|\boldsymbol{E}(\boldsymbol{r})|^2$ obtained from an FDTD simulation. The white circles indicate the structural layout of the cavity. The L3 fundamental cavity mode exhibits a field distribution strongly localized in the center of the defect.

ing dielectric constant $\epsilon(\boldsymbol{r})$. To this end there are essentially two basic paradigms. The guided-mode expansion (GME) method [87, 88] solves Maxwell's equations numerically in a basis of guided modes of an effective homogeneous waveguide that represents the PC membrane. In essence, this method diagonalizes the eigenvalue problem given in Eq. (2.28). The finite-difference time domain (FDTD) method [74, 89, 90] on the other hand relies on the numerical time-propagation of the electromagnetic field and hence provides a simulation of an experiment, in which the optical system is appropriately excited by an oscillating source and the time-evolution of the electromagnetic field is monitored. For the latter technique there exist commercially available software packages, e.g. from Lumerical Computer Solutions Inc.

Figure 2.11b shows the result of an FDTD simulation of the intra-cavity field of the L3 cavity (Graph taken from [65]), together with the structural layout of the cavity (white circles). The simulation shows the distribution of the electric field intensity $|\boldsymbol{E}(\boldsymbol{r})|^2$ in a false-color plot, where the intensity ranges from zero (black) to a maximum (white), going through blue, red, and yellow. Obviously, the cavity field is strongly localized to the defect center and exhibits a distinctive maximum at its center. In order to maximize the cavity Q factor, several modifications to the simple L3 defect consisting of three missing holes can be done. The essential goal of these modifications is to redistribute the $\boldsymbol{k}$ vectors of the intra-cavity field from within to outside the light cone. The latter is defined as the portion of $\boldsymbol{k}$ space that corresponds to propagation directions that do not undergo total internal reflection at the semiconductor-air interface and can hence leave the cavity in vertical direction [91]. The portion of the Fourier transform of the cavity field that lies within the light cone thus gives rise to losses out of the PC plane and therefore crucially determines the achievable Q factor. By an appropriate modification of the cavity geometry, Fourier components within the light cone can be reduced, resulting in an increased Q factor. In the case of the L3 cavity, the main modifications lie in slight shifts of the holes surrounding the L3 defect along the line direction (see Fig. 2.11) [86]. After these modifications, theoretically a Q factor of $Q \sim 300\,000$ can be achieved.

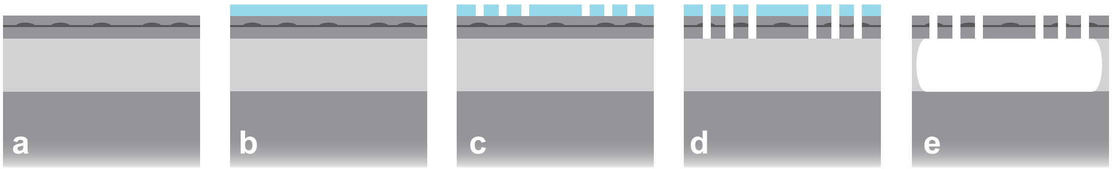

Figure 2.12.: Cavity fabrication procedure. **a**, Semiconductor heterostructure used for cavity fabrication. **b**, Deposition of e-beam resist on the sample surface. **c**, Writing of the PC pattern using electron-beam lithography in the resist layer. **d**, Transfer of the resist pattern into the GaAs by ICP etching. **e**, Underetch of the membrane by hydrofluoric acid.

However, the experimentally realized Q factors are approximately one order of magnitude lower than those predicted by the simulations. In fact, a similar effect can be observed in microdisk cavities. From a detailed study of Q factors in different spectral regimes, it has been shown that the discrepancy between experimentally observed and theoretically predicted Q factors is reduced the further the cavity wavelength is separated from the bandgap of the semiconductor host material. As a result, cavities fabricated in the mid-infrared or the telecom wavelength range reveal an experimental Q factor that is much closer to the theoretical prediction. Although the detailed microscopic mechanisms underlying this effect are not well understood at this point, the current understanding is that the experimental Q is diminished due to background absorption from deep electron and hole defect states in the material and from surface states formed at the GaAs-air interface [92].

In order to fabricate active PC cavities with QDs, an appropriate heterostructure design has to be used in which a layer of QDs is embedded in the center of the cavity membrane, and which furthermore allows for the formation of a free-standing PC membrane. A typical layout of such a heterostructure — usually grown by molecular beam epitaxy — can be seen in Fig. 2.12a. The structure consists of the following layers: on top of the GaAs substrate, an approximately 1 μeV thick sacrificial layer of $Al_{0.7}Ga_{0.3}As$ is grown that is later removed in order to form a free-standing cavity membrane. On top of the sacrificial layer, a 126 nm thick layer is deposited that eventually corresponds to the cavity membrane. In the center of this membrane a single low-density layer of InAs QDs is incorporated.

Once the heterostructure is grown, cavity fabrication proceeds according to the steps indicated in Fig. 2.12b–e. The PC pattern is written in a mask of polymer resist like PMMA or ZEP using electron-beam lithography. This pattern is then transferred into the GaAs host material using an anisotropic dry-etching process that allows for *drilling* holes with straight side-walls. For the structures used in this work, this is accomplished by using an inductively-coupled Plasma (ICP) etching procedure, in which the sample is immersed into a probe chamber where a Plasma of reactive gases is ignited by strong oscillating electric and magnetic fields. During this procedure, the chemical composition of the reactive gases, the process temperature, and the amplitude of the driving fields have to be adjusted in order to achieve the formation of straight sidewalls in the PC membrane. Upon transfer of the PC pattern into the GaAs membrane, the remaining e-beam resist is removed. In order to create a free-standing cavity membrane, the sacrificial $Al_{0.7}Ga_{0.3}As$ material underneath the PC pattern is removed by selective etching in hydrofluoric (HF) acid.

In the present work we use PC defect nanocavities in the L3 configuration as described above. Due to the pronounced field maximum in the center of the L3 defect it is desirable to embed a QD at this very location, in order to experimentally achieve the best coupling. Chapter 4 describes the technological processes employed to this end.

3. Experimental Methods

For the spectroscopic investigation of semiconductor nanostructures, there exist two basic principles: in *luminescence* measurements the emission of a system is analyzed upon some initial excitation process. In *resonant scattering* (RS) schemes on the other hand, one measures the interaction of the system with a resonant probe laser beam. While the former technique allows for visualizing the allowed optical transitions of a system in a parallel manner, the latter in principle allows for the coherent manipulation of the QD states.

In semiconductor spectroscopy, one of the most commonly used techniques is *photoluminescence* spectroscopy (PL), a luminescence technique in which the system is excited by an off-resonant pump laser. This chapter provides a detailed overview of the main technique used in this work: micro-photoluminescence spectroscopy at cryogenic temperatures (Sec. 3.1) in combination with various detection schemes. Section 3.2 moreover discusses their experimental implementation.

3.1. Photoluminescence Spectroscopy

The basic operation principle of a photoluminescence experiment is shown in Fig. 3.1: a pump laser tuned to the vicinity of the GaAs bandgap excites free carriers that relax non-radiatively into the QD states, from which they recombine optically. The resulting luminescence is collected and spectrally analyzed in order to gain insights into the QD levels.

Experimentally, this is typically achieved in a confocal microscopy configuration, as illustrated in Fig. 3.2. An excitation laser beam (green) is focused to a diffraction limited spot on the sample by a high numerical-aperture objective lens. The luminescence created in the structure is then collected by the same microscope objective and subsequently directed to a detector. When using a system in reflection geometry one typically uses a beamsplitter with a large transmission-to-reflection ratio, such that only a small fraction of the collected light is lost. Moreover, the use of pinholes ensures collection from the same diffraction limited spot, the system is excited at, which is the basic principle of confocal microscopy. As a result, such a system can

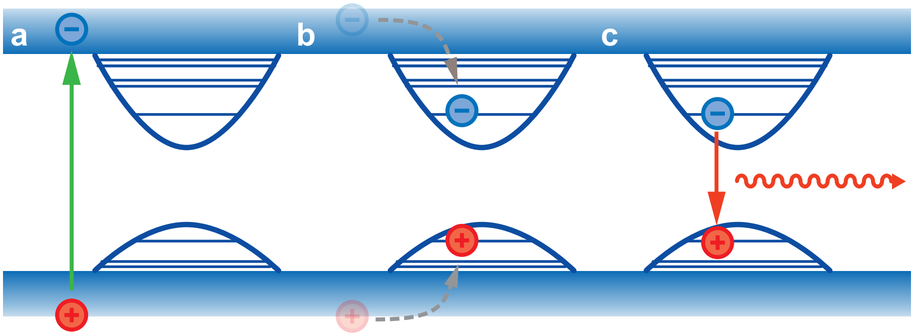

Figure 3.1.: Photoluminescence spectroscopy. **a**, Above bandgap excitation of free electron-hole pairs, **b**, Trapping of carriers in the QD and non-radiative relaxation into the QD states, **c**, Optical recombination of excitons, resulting in characteristic luminescence.

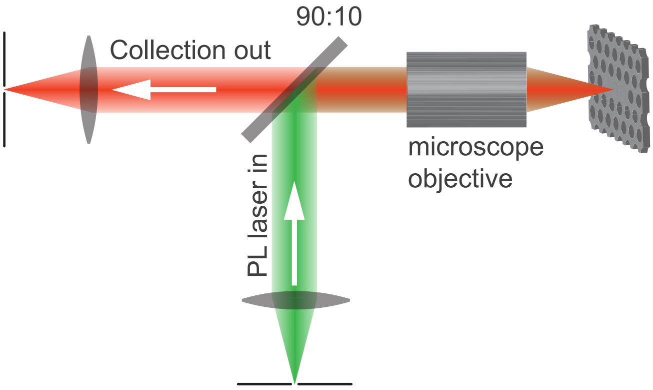

Figure 3.2.: A typical PL setup. The excitation laser is directed towards the sample via a beamsplitter and then focused to a diffraction limited spot using a high NA microscope objective. Luminescence from the same spot is then collected and directed to a detector.

exhibit a spatial resolution close to the diffraction limit, which allows for performing PL spectroscopy on single QDs for samples with sufficiently low QD density. This feature is reflected in the term *micro*-PL. Further details of the optical setup used in this work will be discussed in Sec. 3.2.2.

Naturally, in order to avoid thermal excitation of carriers in the QD single particle states, the sample has to be cooled to cryogenic temperatures. In fact, the InAs QDs employed in this work do not show luminescence for sample temperatures substantially higher than 50 K. This requires cryogenic techniques that allow for optical access to the sample at the same time. The experimental details of the cryo-system used in this work are discussed in detail in Sec. 3.2.1. The following subsections give a more detailed account of the physical mechanisms relevant for micro-PL spectroscopy.

3.1.1. Excitation and Intra-Dot Relaxation

Excitation of the system occurs optically by a laser that creates carriers in the material. This can either occur above the GaAs bandgap (i.e. for wavelengths shorter than 819 nm), such that free electron-hole pairs in the bulk GaAs are formed, or below the bandgap, in order to populate the excited states of the wetting layer. Typically, PL spectra of single QDs show a strong dependence on the excitation wavelength λ_{ex}. For most of the devices investigated here, excitation above the GaAs bandgap did not result in the occurrence of narrow emission lines. The PL spectra rather contained several broad features that are difficult to identify. However, we find that the QDs exhibit clean spectra with well-defined emission lines when pumping the system $\sim$ 10–30 nm below the bandgap. Nevertheless, the relative intensity balance of the lines typically shows a strong dependence on the precise value of λ_{ex}. Most likely, this is due to the presence of shallow acceptor states (mainly formed by C, Si, and Be dopants), such that varying λ_{ex} around the absorption band of these defects (usually around 830–840 nm) results in a charge imbalance of the carriers created in the structure, thus leading to preferred positive or negative charging of the QD [93]. This is manifested in a characteristic re-distribution of the QD-line intensities, when tuning λ_{ex}. Typically, in our experiments we search for a range of λ_{ex} for which the neutral exciton X^0 dominates the spectrum (typically around 834–840 nm).

Carrier relaxation from extended bulk or wetting-layer states into the QD single-particle states was long believed to be extremely inefficient in QDs. Due to the large level spacing of the confined QD states which is on the order of tens of meV, acoustic phonon emission plays a negligible role: since coupling of QD transitions to acoustic phonons can only occur for phonon wavevectors that do not exceed the inverse QD confinement length, phonon scattering is limited to transition energies up to a few meV. Longitudinal optical (LO) phonons in GaAs on the other hand show a weak dispersion and are in turn characterized by a narrow resonance centered around $\sim$ 35 meV. Therefore, LO-phonon coupling should only be possible for intraband-transitions with an energy in the narrow spectral range of the LO-phonon band. Following these arguments, the rate of intra-QD relaxation was initially expected to be very low, leading to a *phonon-bottleneck* [94]. However, it has been shown that this bottleneck is lifted due to the polaron effect [95, 96], which is based on the fact that coupling between LO phonons and QD intraband transitions cannot be treated in a perturbative fashion. In fact, the coupling energy between an LO phonon and an intraband transition of the QD is typically comparable to their mutual detuning, such that this coupling leads to the formation of *polaron* quasiparticles. LO phonons are in turn subject to strong anharmonic decay, such that the formed polarons can decay efficiently via their LO-phonon component. This leads to significant QD intraband relaxation rates on the order of 10^{11} s^{-1}, resulting in a rapid turn-on of QD luminescence upon excitation with an incident laser pulse.

3.1.2. A Typical Quantum Dot PL Spectrum

The optical recombination of QD excitons gives rise to a series of narrow optical transitions, corresponding to different initial and final charge configurations of the QD, as discussed in Sec. 2.2. Since the excitation process used in PL relies on the

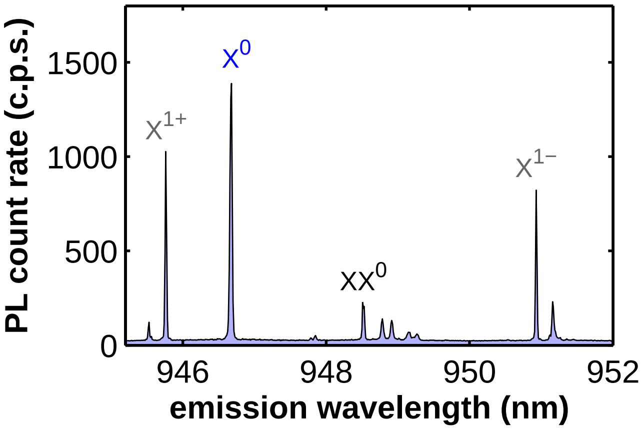

Figure 3.3.: PL spectrum of a single QD. The QD was excited at $\lambda_{\mathrm{ex}} = 838$ nm at a power of $P_{\mathrm{ex}} = 140$ nW. One can easily identify the neutral exciton X^0, the trion states X^{1+} and X^{1-}, and the neutral biexciton XX^0. As can be seen from the ordinate axis, typical count rates for these excitation conditions are on the order of several hundred per second.

random capture of single electrons and holes, a multitude of different charge configurations can be created in the QD with comparable probability, which leads to the co-existence of multiple emission lines in the PL spectrum. Figure 3.3 shows a typical example of a QD PL spectrum, as obtained from a QD using the setup described in Sec. 3.2. For this measurement, the QD was excited with a laser below bandgap at $\lambda_{\mathrm{ex}} = 838$ nm, which is close to the carbon acceptor states. The pump power was $P_{\mathrm{ex}} = 140$ nW. In this spectrum, a few discrete lines resulting from the optical recombination of different exciton configurations can be seen. The most prominent ones comprise the neutral exciton (X^0), the positively (X^{1+}) and negatively (X^{1-}) charged trion, and the neutral biexciton (XX^0). The identification of these lines is not a priori obvious, however it can occur by comparing the characteristic spectral distances between the lines with values reported in literature, or by pump power dependent or photon correlation measurements. Alternatively, the different QD lines can be distinguished by their different behavior, when strongly coupled to a cavity mode (Chap. 6).

The fine-structure splitting δ of the X^0 which was introduced in Sec. 2.2.3 typically lies below the spectral resolution of the spectrometer (~ 30 μeV in our case). The splitting between the X^0 and the X^{1-} which reflects the binding energy of the extra electron amounts to 4.2 nm in this device. As mentioned in Sec. 2.2.3, this value is fairly reproducible from dot to dot and provides a practical means of identifying the X^0 and the X^{1-}. In contrast, the hole-hole repulsion, dictating the splitting between the X^0 and the X^{1+}, can be subject to substantial variations for different QDs [61].

The peak labeled as XX^0 corresponds to emission from the neutral biexciton state, in which two electron-hole pairs are stored within the QD. The lines around the XX^0 correspond to differently charged biexcitonic states, where — besides the

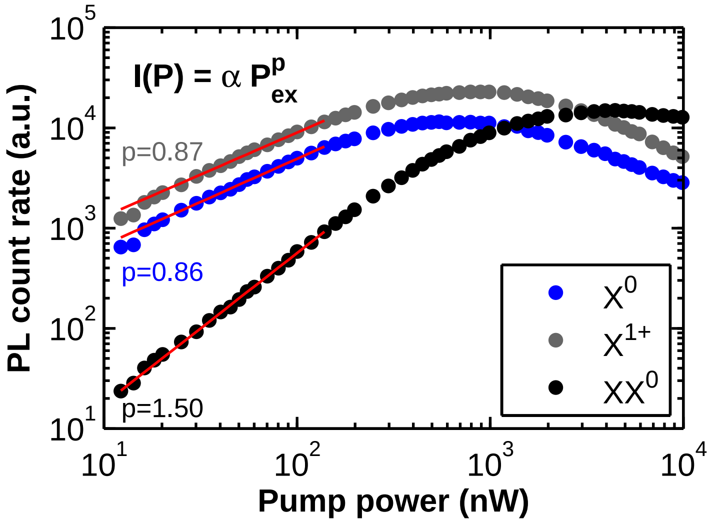

Figure 3.4.: PL pump power dependence. The integrated PL intensities of the X^0, the X^{1+}, and the XX^0 lines are shown as a function of excitation power. The solid lines are power-law fits to the data for powers well below saturation.

two excitons — extra electrons or holes are present in p-shell levels of the QD. Exciton or trion emission can easily be distinguished from biexcitonic lines by the characteristic dependence of their PL intensities on the power of the pump laser. States containing a single electron-hole pair ideally show a linear power-dependence, while biexcitonic configurations are characterized by a quadratic power-dependence. Figure 3.4 shows a pump-power dependence of a typical QD PL spectrum in a double logarithmic plot. Here PL spectra recorder for different pump powers were integrated in narrow spectral windows around the corresponding QD emission lines. From polynomial fits to the data we find that the X^0, X^{1+}, and X^{1-} states follow a power dependence $I \propto P_{ex}^p$ with $p \approx 0.9$, while the biexciton shows $p \approx 1.5$. The deviation from the ideal values ($p = 1$ and $p = 2$) is due to the presence of dark excitons and due to possible excitation of the XX^0 e.g. by electron capture from a X^{1+} state.

The acquisition of pump-power dependent PL data is a useful tool for distinguishing exciton lines stemming from different excitation manifolds of the QD. Moreover, we make extensive use of this technique when investigating coupled QD-cavity devices (see Chap. 7).

3.1.3. Time-Correlated Single-Photon Counting

While PL spectra like the one shown in Fig. 3.3 contain spectral information about the available and optically allowed transitions of the QD, they do not allow for any conclusions on the time dynamics of optical recombination in a QD. Exciton relaxation times can be measured by the technique of time-correlated single-photon counting (TCSPC). To this end, the QD is excited by a pulsed laser source and the PL of a filtered QD line is directed to a single-photon counting module (SPCM).

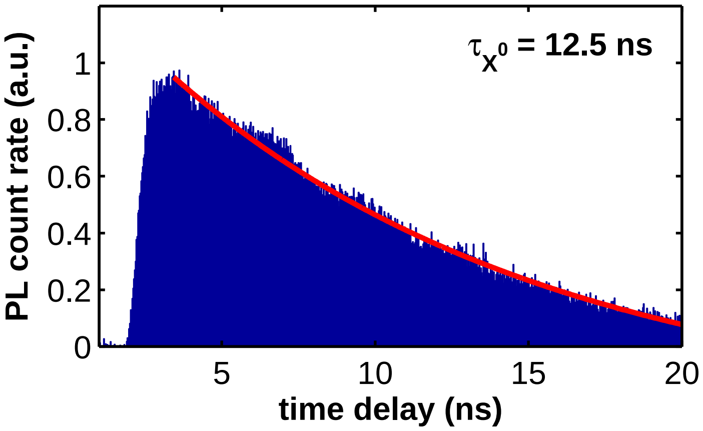

Figure 3.5.: TCSPC measurement on a QD neutral exciton. The data shows a luminescence decay curve of the X^0 line of a single QD. The curve can be fitted with an exponential decay of the form Eq. (3.1). The solid red line shows such a fit with a time constant of τ_{X^0}.

Typically one employs avalanche photodiodes (APDs) in Geiger mode (see Sec. 3.2.3) that provide voltage pulses when a single photon is detected. In TCSPC the time differences between the recorded photon detection events and the corresponding excitation pulse are registered and stored in a histogram that shows the number of coincidences as a function of their time delay. In this way one obtains a luminescence decay curve that traces out the population of a certain excitonic state as a function of time. Fig. 3.5 shows the result of such a measurement, performed on the X^0 emission line of a QD embedded in a photonic crystal. This *luminescence decay curve* shows the averaged PL intensity as a function of the time delay after excitation. Clearly, the PL intensity here undergoes exponential decay upon initial excitation by a laser pulse of $\sim$1 ps duration[1] centered at $\lambda_{\text{ex}} = 780$ nm[2].

The decay of the X^0 luminescence can be fitted with an exponential decay curve of the form

$$I_{X^0}(t) = I_{\text{dark}} + I_{X^0}^{(0)} \exp\left(-\frac{t-t_0}{\tau_{X^0}}\right). \tag{3.1}$$

In this expression, I_{dark} refers to the background signal arising from APD dark counts. For the data shown in Fig. 3.5, the best fit is obtained for a time constant of $\tau_{X^0} = 12.5$ ns (red line). The rising edge of the curve corresponds to the timescale of excitation of the X^0 upon absorption of the excitation laser pulse. This timescale reflects that of intra-dot relaxation as discussed in Sec. 3.1.1 and is typically faster than the timing resolution of our experimental system.

---

[1] This timescale is much shorter than both the timescales of intraband relaxation within the QD and the timing resolution of the detection apparatus, which is on the order of $\sim$100 ps.

[2] This TCSPC trace was obtained using the pulsed laser diode with switchable repetition rate described in App. A. This was one of the few devices that showed “clean” PL spectra when excited above bandgap.

3.1.4. Photon Auto-Correlation Measurements

A widely-used technique in quantum optics is the measurement of intensity correlation functions, which enables conclusions on the classical or quantum nature of the underlying light source [36]. The normalized second-order (intensity) autocorrelation function for a single mode of the light field characterized by the wavevector $\boldsymbol{k}$ is defined as

$$g^{(2)}_{\boldsymbol{k}}(t,\tau) = \frac{\langle : \hat{I}_{\boldsymbol{k}}(t)\hat{I}_{\boldsymbol{k}}(t+\tau) : \rangle}{\langle \hat{I}_{\boldsymbol{k}}(t)\rangle^2}, \tag{3.2}$$

where $\hat{I} \propto \hat{a}^\dagger \hat{a}$ is the intensity operator of the field and ":" refers to normal operator ordering. In terms of the field annihilation operator $\hat{a}$ this reads

$$g^{(2)}_{\boldsymbol{k}}(t,\tau) = \frac{\langle \hat{a}^\dagger_{\boldsymbol{k}}(t)\hat{a}^\dagger_{\boldsymbol{k}}(t+\tau)\hat{a}_{\boldsymbol{k}}(t+\tau)\hat{a}_{\boldsymbol{k}}(t)\rangle}{\langle \hat{a}^\dagger_{\boldsymbol{k}}(t)\hat{a}_{\boldsymbol{k}}(t)\rangle^2}. \tag{3.3}$$

Experimentally, the ensemble average $\langle \ldots \rangle$ in Eq. (3.2) and Eq. (3.3) is replaced by a time average, corresponding to the accumulation of the signal $\hat{I}_{\boldsymbol{k}}(t)$ over a certain integration time that is typically much longer than the relevant timescales of the system dynamics. The correlation function can then be evaluated in steady state, and the t dependence of $g^{(2)}_{\boldsymbol{k}}(t,\tau)$ can be dropped.

Phenomenologically, $g^{(2)}_{\boldsymbol{k}}(t,\tau)$ gives a measure for the conditional probability of detecting a photon from mode $\boldsymbol{k}$ at time $t+\tau$, given that another photon has previously been measured at time t. For $\tau = 0$, $g^{(2)}_{\boldsymbol{k}}(0)$ thus gives the probability of measuring two photons in the same mode simultaneously. The case of $g^{(2)}_{\boldsymbol{k}}(\tau) = 1$ is referred to as *Poissonian statistics*, which means that the photon detection events are entirely uncorrelated, such that the probability of detecting a second photon does not change upon detection of the first photon. While for classical light sources $g^{(2)}_{\boldsymbol{k}}(\tau) \geq 1$, quantum emitters can show *sub-Poissonian* statistics with $g^{(2)}_{\boldsymbol{k}}(0) < 1$. The most extreme example of a non-cassical field state giving rise to sub-Poissonian statistics is that of a single-photon Fock state $|n\rangle = |1\rangle$. In this case, obviously $\langle 1|\hat{a}^\dagger\hat{a}^\dagger\hat{a}\hat{a}|1\rangle = 0$, a situation referred to as *antibunching*: due to the presence of merely a single photon in the observed mode of the field, the probability of detecting two photons simultaneously is zero.

The auto-correlation function $g^{(2)}(\tau)$ is usually measured using a Hanbury-Brown–Twiss setup as schematically shown in Fig. 3.6. Photons in the incident arm are split on a beam-splitter and then directed onto two photodetectors. Measurement of the product of the intensities at the two detectors yields $g^{(2)}(\tau)$. Hypothetically, to this end one could use two photodiodes that convert the incident light intensities to electrical currents $i(t)$ according to $i(t) \propto I(t)$, such that a measurement of the current product $\langle i_1(t)\, i_2(t+\tau)\rangle$ reveals an estimate of $g^{(2)}(\tau)$. Technically however, even the most sensitive linear photodiodes exhibit a background noise level that exceeds the signal created by a single photon by several orders of magnitude. Usually one therefore employs avalanche photodiodes (APDs) as introduced in Sec. 3.1.3. They provide the advantage of shot-noise limited operation. However, these devices do not allow for the distinction between single and multi-photon detection events, such that no information about the intensity $\langle \hat{I}(t)\rangle$ can be gained. Nonetheless, by using the HBT scheme it is possible to obtain an estimate of $g^{(2)}(\tau)$, following a

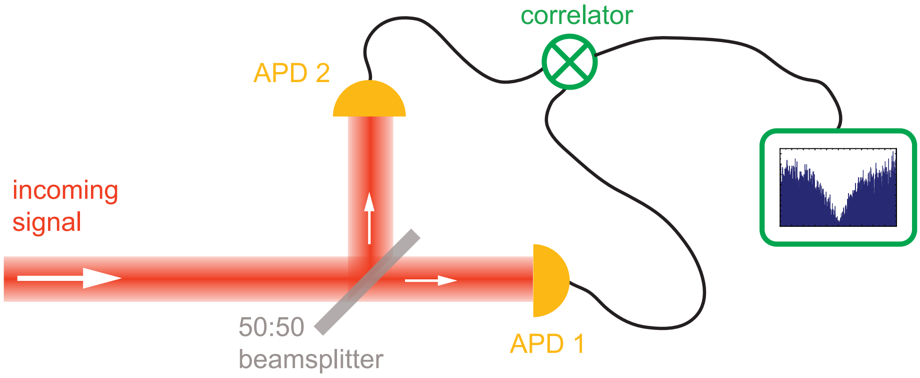

Figure 3.6.: Hanbury-Brown–Twiss setup. An incident field is split using a 50:50 beamsplitter. Each output is directed to a single-photon counting module. The arrival times of the corresponding photons are analyzed by the correlator.

similar approach as the one introduced above in the context of TCSPC. A correlation electronics measures time differences between coincidence photons detected on the two APDs and then accumulates a corresponding histogram that shows the number of registered coincidence events as a function of time delay. If the count rate of the two detectors is much smaller than the inverse width of the window of the investigated τ, this method leads to a good estimate of $g^{(2)}(\tau)$.

While in the first demonstration of antibunching, the focus was on the demonstration of the quantum nature of light itself [97], in the field of semiconductor quantum optics measurement of $g^{(2)}(\tau)$ has become a versatile tool for testing the single-emitter characteristics of a given light source. Comparable to the case of atoms, the emission of QDs shows a high degree of anti-bunching, rendering them nearly perfect single-photon sources [45]. Figure 3.7 displays a measured auto-correlation function $g^{(2)}_{X^0}(\tau)$ of the X^0 transition of a typical QD. The strong reduction of coincidence counts at zero time delay ($g^{(2)}(0) \approx 0.02$) is clearly visible. As this experiment has been conducted under continuous-wave excitation, coincidence photon counts can be detected, if their temporal separation exceeds the coherence time of the emitter. The recovery of coincidence counts on either side of $\tau = 0$ follows the characteristic exponential dependence

$$g^{(2)}_{X^0}(\tau) = 1 - \exp\left(-\frac{|\tau|}{\tau_{X^0}}\right) \tag{3.4}$$

with a timescale given by the emitter radiative lifetime τ_{X^0} in the limit of weak excitation. From a two-sided exponential fit to the data, we find $\tau_{X^0} \approx 6.9$ ns in this case.

3.1.5. Photon Cross-Correlation Measurements

Another useful technique that provides valuable insights into the time dynamics of different emission channels in the QD PL spectrum is provided by photon cross-correlation measurements. Here, one measures correlations between photon counts stemming from different modes of the emitted light field. A generic example in

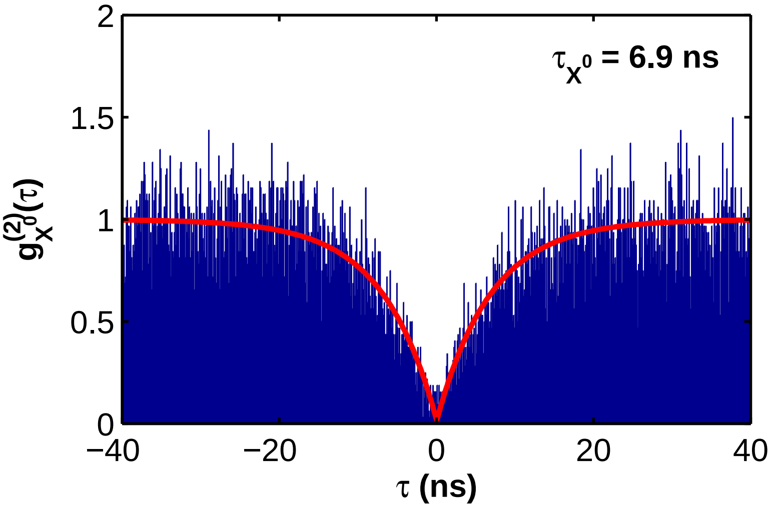

Figure 3.7.: X^0 auto-correlation. Normalized auto-correlation function $g^{(2)}_{X^0}(\tau)$ of the X^0 emission of a single QD, measured in a standard HBT setup as illustrated in Fig. 3.6. The curve exhibits strong *antibunching*, meaning that the rate of coincidence counts for $\tau = 0$ is strongly suppressed.

the case of QDs is the cross-correlation between biexciton (XX^0) and exciton (X^0) photons from a single QD, which naturally form a radiative cascade: as shown previously in Fig. 2.8, optical decay of the XX^0 occurs to an intermediate X^0 state, such that there exists a distinctive time-ordering of the two emission channels [98] that can be observed by photon cross-correlation measurements. The XX^0–X^0 cross-correlation function is defined as

$$g^{(2)}_{XX^0,X^0}(t,\tau) = \frac{\langle : \hat{I}_{XX^0}(t)\hat{I}_{X^0}(t+\tau) : \rangle}{\langle \hat{I}_{XX^0}(t)\rangle\langle \hat{I}_{X^0}(t+\tau)\rangle} \tag{3.5}$$

and gives the conditional probability of detecting a X^0 photon at time $t+\tau$ upon detection of a XX^0 photon at time t.

Experimentally, such a measurement is implemented by separating the two emission lines of the QD using a dispersive optical element, e.g. a diffraction grating, and directing them to two different single-photon counters. Exactly as in the case of the HBT scheme, one then constructs a histogram giving the temporal distribution of coincidence events.

A measured $g^{(2)}_{XX^0,X^0}(\tau)$ is displayed in Fig. 3.8. The distinct asymmetry reflects the cascading behavior of the XX^0–X^0 system. Positive τ on the time axis refers to X^0 detection upon XX^0 detection. Clearly, detection of a XX^0 photon at time $\tau = 0$ prepares the QD in the X^0 state, which leads to a significant enhancement of the X^0 detection probability. This is reflected in the large bunching peak for positive τ. Correspondingly, negative τ refers to XX^0 upon X^0 detection. Since the latter projects the QD in the ground state, the observation of a XX^0 photon requires re-excitation of the QD, resulting in the antibunching dip for negative time delays.

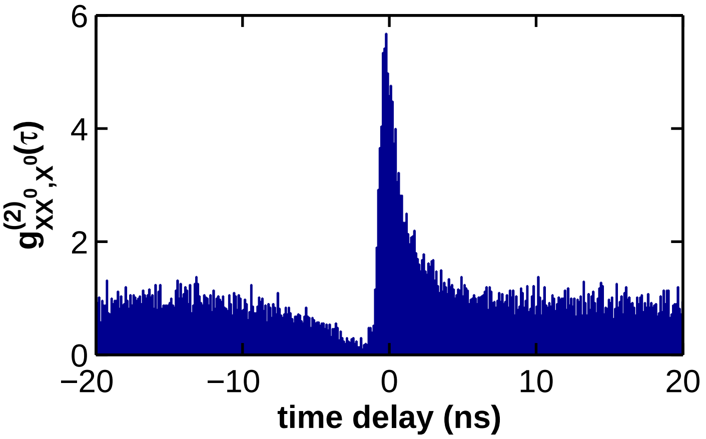

Figure 3.8.: **XX^0–X^0 cross-correlation measurement.** The asymmmetric shape of the correlation trace is related to the cascaded nature of XX^0 and X^0 emission. Positive (negative) time delays refer to X^0 detection after (before) XX^0 detection. Observation of a XX^0 photon projects the QD in the X^0 state, which results in the strong bunching peak for $\tau > 0$.

Observing features like the one shown in Fig. 3.8 provides valuable information for the understanding of time ordering of certain transitions in a QD, making cross-correlation measurements a valuable tool for QD research.

3.2. Experimental Setup

A major part of the work presented in this thesis involved the design and construction of an experimental apparatus that implements the techniques described in Sec. 3.1. In the course of this project, we developed two spectroscopy setups that are discussed in detail in the following sections.

3.2.1. Cryogenics

The heart of a setup for nanostructure investigation is a cryogenic environment for controlled cooling of the sample. In practice, there is a large variety of schemes for sample cooling, essentially all of them relying on the use of liquid ^{4}He that has a boiling point of $T = 4.2$ K at ambient pressure. For establishing thermal contact between the sample and a cryogenic reservoir, two main principles are used: the immersion of a sample chamber filled with ^{4}He exchange gas into a bath of liquid ^{4}He (bath cryostats), while the other possibility is to mount the sample in a high vacuum chamber with only the sample holder being cooled by a continuous flow of liquid ^{4}He. In the experiments presented here, we only make use of the second technique.

For the two setups constructed in our lab, two different types of flow cryostats were used: a Microstat®He flow cryostat by Oxford Instruments and a Konti-Cryostat-Mikro from CryoVac Low Temperature Technologies Inc. The former is a very straightforward device consisting of a cold-finger inserted into a vacuum chamber that allows for optical access to the sample. Cooling proceeds by insertion of a Helium transfer tube into the cold-finger and establishing a continuous flow of liquid ^{4}He. Since the sample is mounted in a fixed position within the cryostat, either the entire cryostat or the optics has to be mounted on a flexible stage, in order to access different regions on the sample chip. In fact, the distance between different QD-cavity devices on the samples used here can be as large as several millimeters, i.e. much larger than the field of view of the microscope objective. Here, we constructed a compact optical setup based on a Thorlabs cage system mounted on a three-axis positioner from Melles Griot. Although the cryostat can then be fixed on the optical table, the internal construction of the cryostat relying on a rigid mechanical connection between the cold-finger and the transfer tube does not allow for extremely high sample stability, such that significant sample drift poses a considerable limitation for most optical experiments. However, given the short cool-down times of this system, it provides an optimal setup for fast sample characterization.

In the Konti cryostat from CryoVac, the sample is mounted on a circular sample holder that is connected to the Helium inlet via a flexible tubing system. The apparatus is constructed such that the sample holder has a weak mechanical connection to the outside world, which increases the sample stability considerably. Furthermore, this system contains an integrated two-axis positioner for moving the sample within the cryostat. In this setup, the optics was constructed in a rigid and stable way on an optical breadboard.

3.2.2. Confocal microscopy

This section provides an overview of the optical setup used for the experiments presented in this thesis. While only the rigidly mounted setup used together with the CryoVac Konti cryostat is discussed, the system developed for the Microstat®He cryostat is built in an analogous fashion. A detailed account of the confocal microscopy setup used in this work is given in App. A.

For PL spectroscopy the sample is excited by an incident laser beam, and the luminescent light is collected for further analysis. In this work, this is implemented in a reflection geometry, in which the excitation light passes through the same microscope objective as the light collected from the sample (Fig. 3.2). Using a 90:10 beamsplitter ensures a signal loss of only 10%. Both the excitation and the collection arm are coupled to the laser source and the spectrometer, respectively, via single-mode optical fibers. Working with a fiber-based system does not only provide the advantage of increased flexibility when changing the excitation laser or the detection apparatus, but also allows for good spatial coherence of the signal. Since the emission (and the collection) profile of a single-mode fiber is close to an ideal Gaussian beam, the excitation laser is automatically spatially filtered, and the collection fiber naturally establishes a confocal microscope configuration by restricting the signal collection to a single diffraction-limited spot.

In order to obtain both maximum collection efficiency and high spatial resolution, we use a focusing optics with high numerical aperture (NA = 0.55). Focusing a Gaussian laser beam ideally results in a spot size of $D \approx \frac{2\lambda}{\pi \mathrm{NA}} \approx 930$ nm. Practically however, the focusing performance is limited by spherical aberrations introduced by the cryostat window. To circumvent this problem, we use a Nikon microscope objective (CF Plan 50X CR, EPI) that has a continuous cover-glass correction and thus allows for imaging performance close to the diffraction limit. A disadvantage of this element lies in an imperfect chromatic correction in the near infrared, such that it is not possible to obtain perfect focusing in the same plane for the luminescent QD light ($\lambda \sim 940$ nm) and the excitation laser ($\lambda \sim 800$ nm). This problem can be solved by introducing an intermediate focal plane in the PL excitation arm such that a tight focal spot on the sample is achieved. For RS measurements as discussed in Chap. 8, we use a different excitation arm aligned for collimation at $\lambda \sim 940$ nm which is combined with the PL arm on a 50:50 beamsplitter.

Control of the polarization of the collection light occurs after the fiber. Single-mode fibers induce unitary rotations of the polarization state that can easily be controlled using the elasto-optic effect: bending the fiber introduces birefringence that allows for the control of the polarization state of the light exiting the fiber. We accomplish this by using home-built fiber polarization paddles that allow for controlled twisting of a single-mode fiber. This technique is particularly important for the crossed-polarization scheme used for RS measurements described in Sec. 8.2.

In order to monitor the sample during experiments, a standard optical microscope with infinite conjugate ratios was implemented in the system. A flip mirror in the collection path (M2 in Fig. A.1) allowed for directing the signal from the sample to an integrating CCD camera. When illuminating the sample with a LED emitting in the near infrared, we obtain a high resolution image of the sample surface. Moreover, in this fashion it is possible to obtain an image of the spatial distribution of the QDs by obtaining PL micrographs: by defocussing the excitation laser we ensure wide-field excitation of the material over a large area ($\sim 50\ \mu$m). The PL emission is then imaged on the CCD, while the excitation laser is filtered by an interference filter.

3.2.3. Detection Apparatus and Time-Correlated Measurements

The spectrometer In PL spectroscopy, the spectral distribution of the luminescence signal is analyzed using a grating spectrometer, with the basic operation principle shown in Fig. 3.9a. The PL light is focused onto an entrance slit with a numerical aperture that is adapted to that of the spectrometer. Inside the device, the light is incident on a concave mirror that collimates the incoming signal and directs it to a diffraction grating. The first diffraction order of the grating is directed to another concave mirror that then directs the light onto a charge-coupled device (CCD) camera. The diffraction angle on the grating is proportional to the wavelength λ, thus creating a wavelength-resolved virtual image of the PL spectrum that is transfered to a real image in the CCD plane by the second concave mirror. The spectral resolution of the system is determined by the dispersion of the grating and the focal length of the imaging mirrors which determines the magnification factor between the virtual image of the spectrum formed after the grating and the real image in the CCD plane.

In this thesis we use an Acton Standard SP2750 spectrograph from Princeton Instruments that has a focal length of $f = 750$ mm and a numerical aperture of NA $= 0.052$. For high-resolution PL spectroscopy, a holographic diffraction grating with 1500 grooves per mm is available. The image of the PL spectrum is detected

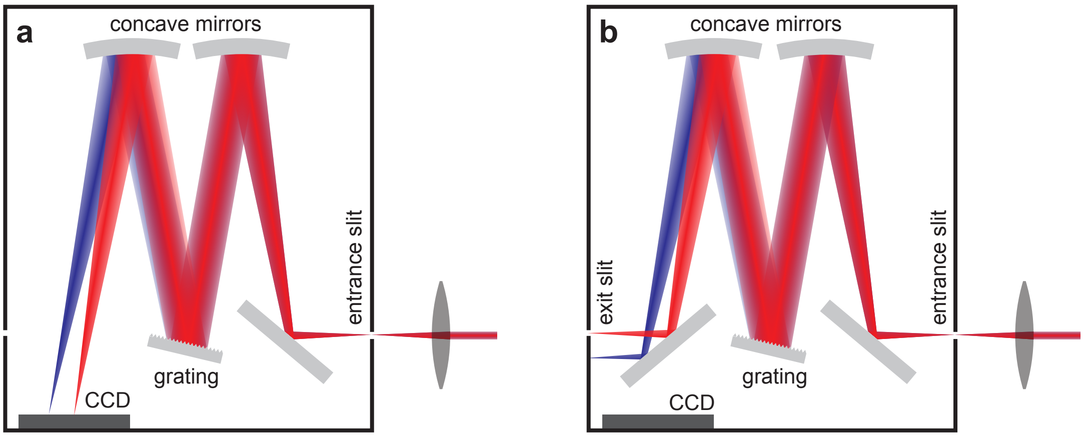

Figure 3.9.: The grating spectrometer. **a**, Spectroscopy mode: the incoming signal is collimated and directed to a diffraction grating that creates a $\boldsymbol{k}$-space image of the spectrum which is imaged onto a CCD chip. **b**, Monochromator mode: Here, the dispersed signal is sent to an exit plane in the side of the spectrometer by an additional flip mirror. A slit of variable size lets the relevant a small portion of the spectrum pass to the outside.

with a liquid N_2-cooled CCD camera that provides single-photon sensitivity at a working temperature of $T = -120\,°\mathrm{C}$. The CCD camera comprises a matrix of 1340×100 pixels each of dimension 20 μm × 20 μm.

In this system, we typically achieve a spectral resolution of ≈ 30 μeV. Efficient coupling to the low NA of the spectrometer is facilitated by the use of a single-mode fiber that guides the PL collected from the sample: by the use of an appropriate imaging optics the NA of the single-mode fiber can be matched to that of the spectrometer. Control of the grating position as well as readout of the CCD chip proceeds in a computerized manner.

System for time-correlated measurements Time-correlated detection schemes like those described in Sec. 3.1.3, Sec. 3.1.4, and Sec. 3.1.5, typically require spectral filtering of the photons of interest. For example, in order to measure TCSPC on the X^0 line of a QD, this line first has to be isolated from other parts of the PL spectrum. Here, we usually accomplish this by using the spectrometer as a monochromator: a flip mirror in front of the CCD camera directs the spectral image to a side exit of the spectrometer (see Fig. 3.9b). An adjustable slit in the side image plane allows for narrow spectral filtering of the emitted light that can then be directed to the single-photon counting modules (APDs).

For TCSPC measurements (Sec. 3.1.3), a filtered portion of the spectrum is directed to a single APD. For HBT measurements (Sec. 3.1.4), a pellicle beamsplitter with a splitting ratio of nominally 45 : 55 divides the filtered light from the spectrometer into two arms which are then directed to two APD modules. For cross-correlation measurements (Sec. 3.1.5), we separate the light of the two spectral windows of interest using the spectrometer, as illustrated in Fig. 3.10. The image of the PL spectrum is available in the exit-slit plane of the spectrometer. By opening the

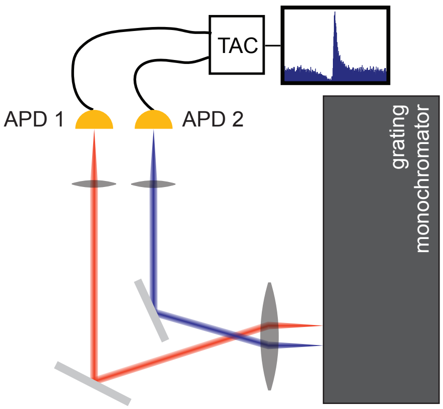

Figure 3.10.: Setup for photon cross-correlation measurements. The two spectral windows exiting the spectrometer at different locations are separately directed to two APDs.

spectrometer slit enough, the two windows can be extracted from the spectrometer. A focusing lens after the spectrometer then images the slit plane to infinity. The luminescence from the two different spectral windows propagates at different angles. Mirrors then direct the two signals separately onto two APDs. In this scheme, the chip of the APD provides the "pinhole" that together with the magnification of the imaging system determines the spectral bandwidth of light that is analyzed on the APD.

Single photons are detected with Si-based avalanche photodiodes (APDs). These devices consist of a p-i-n photodiode operated under extreme reverse bias close to breakdown. Absorption of a photon creates an electron-hole pair and both the electron and the hole experience strong acceleration in the applied electric field. Electron-electron scattering then results in the excitation of additional carriers across the bandgap which are in turn accelerated across the junction. As a result, a charge avalanche builds up which results in an amplification of the initial signal of several orders of magnitude. APDs operated in *Geiger mode* enable the detection of single photons. However, as the charge avalanche typically saturates the chip, no photon-number information can be extracted from the output pulse. APDs can only distinguish between zero and n photons, where n can be $n \gg 1$.

The electronic signal provided by the APDs is analyzed using a fast timing electronics from ORTEC®. Timing between single photon counting events is accomplished by a time-to-amplitude converter (TAC) that measures the time difference between a start and a stop pulse and converts it to a voltage signal of a proportional amplitude (we use the ORTEC 567). A multichannel analyzer card then accumulates a histogram of the voltage signals received from the TAC, giving histograms like the ones shown in Fig. 3.5, Fig. 3.7, and Fig. 3.8.

4. Implementation of a Single QD-Cavity System

The experiments presented in this thesis are based on a cavity QED system formed by a single QD strongly coupled to the fundamental mode of a PC defect cavity in the L3 configuration. The experimental realization of such a device faces two main challenges: First, in order to ensure a significant coherent coupling strength g between a QD exciton and the mode of the microcavity, $|\boldsymbol{\varphi}(\boldsymbol{r}_{\mathrm{QD}})|$ in Eq. 2.8 should be maximized by placing the QD at a location $\boldsymbol{r}_{\mathrm{QD}}$ close to the maximum of the cavity electric field. The central lobe of the fundamental L3 cavity mode has an extension on the order of ~ 100 nm (see also Fig. 2.11), such that relative positioning with an accuracy on that scale is desirable. Due to the random nucleation sites of self-assembled QDs this is a highly nontrivial task. The second challenge lies in the relative spectral alignment between the cavity mode resonance and the QD excitons in order to study resonant dynamics. In other words, a tuning mechanism is needed that allows for changing the cavity mode wavelength during the experiment. The following sections discuss the techniques we developed for ensuring both spatial (Sec. 4.1) and spectral (Sec. 4.2) overlap of the cavity mode with the QD.

4.1. Spatial Positioning

A flaw of self-assembled QDs is their inherently random nucleation site in the Stranski-Krastanow growth mode of elastic strain relaxation. While several attempts have been made towards the external control of the QD position, e.g. by lithographically creating nucleation centers [99], these techniques typically led to the growth of QDs of lower spectral quality, mainly due to the occurrence of strong non-radiative decay channels enabled by the peculiar material distribution of such structures. High-precision quantum optical experiments thus are still restricted to randomly positioned self-assembled QDs, for which coupling to functional nano-structures is naturally a non-trivial task. The route followed by most research groups working in the field is random positioning of a multitude of cavities on a substrate contain-

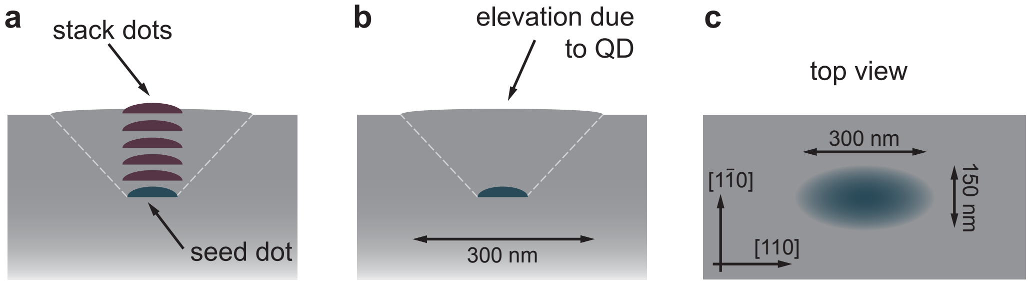

Figure 4.1.: Signature of a buried QD on the sample surface. **a**, The positioning scheme used in [26] employs a stack of QDs grown on top of the seed QD that can be imaged using SEM. **b**, AFM mapping of a single QD makes use of a shallow elevation on top of the QD that protrudes $\sim$1 nm from the sample surface. **c**, Top view of the hill formed on the surface, indicating its typical dimensions

ing QDs with a density of several 10 μm^{-2}. Subsequently, the devices that show significant coupling between the cavity mode and some QD transition are selected and used for further experiments [28–30, 75, 82, 100]. Typically, this approach does not lead to optimal spatial alignment between the cavity and the QD, and even for a system that shows significant coupling the distinction of the spectral features stemming from different QDs within the cavity mode volume can be difficult and frustrating.

In contrast, in this work, a deterministic coupling approach is followed that relies on active positioning of PC cavities around preselected QDs. To this end it is necessary to determine the coordinates of the target QDs with respect to some alignment markers prior to cavity fabrication. The need for cavity positioning on a < 100 nm scale makes localization of QDs by purely optical means difficult, such that imaging techniques of higher spatial resolution are required. A main challenge arises however from the low visibility of single QDs on the sample surface: grown in the center of the PC membrane, they are buried by a $\sim$63 nm capping layer of GaAs which makes them invisible for a scanning electron microscope (SEM). In the first demonstration of deterministic QD-cavity coupling, this problem was solved by creating a distinctive marker on the sample surface directly above the QD of interest in order to increase the image contrast in SEM [26, 101]. The marker consisted of a stack of strain-correlated QDs piled up on top of the seed dot [102, 103] as shown in Fig. 4.1a. Stacking of QDs can be accomplished in a fairly straightforward manner, since upon growth of an initial QD layer, the GaAs matrix on top of each QD is strained which creates a nucleation center for the next layer of QDs. Accordingly, it is possible to grow stacks of QDs that protrude from the surface of the sample and create a narrow pronounced hill that is visible by SEM. Making use of this technique, the relative coordinates between the QD stack and a pattern of predefined Ni/Au markers could be mapped out. Furthermore, the marker dots could easily be distinguished spectrally from the seed dot, since the latter was thermally annealed using the PCI technique described in Sec. 2.2.1 in order to shift its emission wavelength approximately 150 nm blue with respect to the dots of the stack. This technique allowed for the demonstration of significant Purcell enhancement in S1

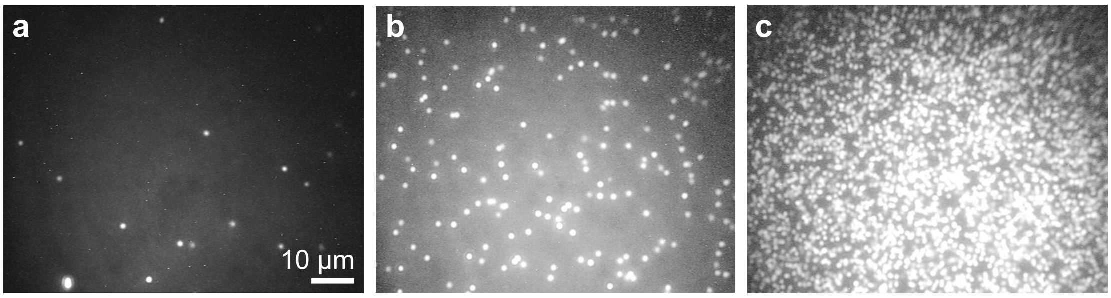

Figure 4.2.: PL micrographs in different density regions of a QD sample. The bright spots are QDs emitting PL light. The images were acquired in a 50× magnification microscopy setup with wide-field above-bandgap laser illumination. The excitation laser was suppressed by the use of a bandpass filter cutting light with a wavelength < 900 nm. **a-c** shows different density regions of the sample.

and L3 cavities [26].

Despite the great practicality of this technique, the presence of the marker stack potentially has a detrimental effect on the cavity Q factor, either by enhancing scattering losses due to the increased surface roughness, or due to absorption in the excited states of the marker QDs [65]. In order to avoid these potential limitations, a technique for the mapping of single layer QDs was developed in this work which comprises one of the central tools of this thesis. This mapping technique makes use of a shallow hill of material formed on the sample surface right on top of the QD. When the GaAs capping layer is grown on top of the InAs islands that form the QDs, the GaAs lattice structure is distorted due to the presence of the underlying InAs inclusion, which leads to a deformation of the material in a conical region on top of the QD. This situation is schematically depicted in Fig. 4.1b. Typically, the dimensions of this hill are much larger than those of the buried QD itself, owing to the conical shape of the material distortion on top of the QD. Moreover, this feature exhibits a peculiar elliptical shape that is typically elongated along the [110] crystalline direction of the GaAs substrate. As indicated in Fig. 4.1c, the hill typically has a size of ~ 150 nm × 300 nm and protrudes ~ 1.0-1.5 nm from the sample surface. While such a shallow feature cannot give rise to sufficiently large contrast in SEM, it is clearly observable using an atomic force microscope (AFM), since the latter provides much better resolution in the vertical direction than an SEM. Imaging then proceeds by acquiring AFM traces of the dot together with a marker feature, such that the relative coordinates between the two can be extracted.

Following this approach, we developed the following scheme for the fabrication of deterministically coupled single QD-cavity devices:

1. Selection of an appropriately sized chip from the ultra-low density region of an InAs/GaAs QD wafer (QD density $\sim 10^{-2}$–10^{-1} μm^{-2}). This is done by acquiring PL micrographs, as shown in Fig. 4.2. Following the discussion in Sec. 3.2.2, for this measurement the sample is illuminated with a laser above bandgap over a large area. The emission is then imaged onto an integrating CCD camera using an imaging system of 50× magnification while the excitation laser is suppressed by a bandpass filter. Figures 4.2a–c show different

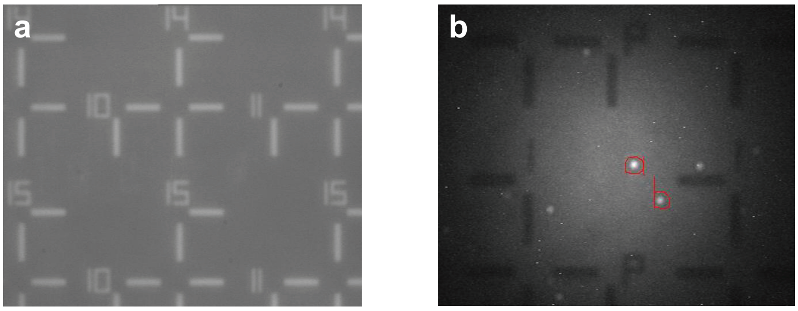

Figure 4.3.: Microscope image of gold markers. **a**, Microscope image of the gold marker layout under illumination with a near-infrared LED. In the figure one can see two square fields with their corresponding labels (the fields correspond to columns 10&11 in row 15). **b**, PL micrograph showing a single field containing two candidate QDs that are sufficiently isolated. The substrate here exhibits some emission below the bandgap, giving rise to the gray emission background. The gold markers are hence visible as shadow images.

density regions of the same sample. Only the QD density realized in Fig. 4.2a is useful for active positioning of PC cavities (typically $\sim$0.1–1 μm^{-2}).

2. Fabrication of Ni/Au markers in the chosen density region of the chip that allow for the identification and retrieval of single QDs. Technically, this is achieved by electron-beam lithography in combination with a lift-off process. Figure 4.3a shows an optical micrograph taken of the sample upon gold marker deposition under broadband illumination from a near-infrared LED. In the layout used here the sample is divided up into a square matrix of labeled fields (this figure shows columns ten and eleven in row 15). The seemingly redundant number of legs in this marker layout is necessary for the calibration of the sample position in the e-beam writer used for subsequent cavity fabrication.

3. Optical investigation of the chip using photoluminescence (PL) imaging (Sec. 3.1) and selection of well-isolated single QDs at distances from the gold markers sufficient for cavity fabrication. Figure 4.3b shows a PL micrograph as in Fig. 4.2 of a specific field containing gold markers. Obviously the sample exhibits some emission below bandgap, which gives rise to the gray emission background. For this reason, the gold markers can clearly be seen as shadow images. In the field shown in Fig. 4.3b, two well-isolated QDs have been identified (marked by the red letters).

4. Spectral investigation of the selected QDs using PL and further narrowing of the QD selection to those showing “clean” PL spectra with easily identifiable emission lines.

5. Obtaining high-resolution AFM images of the candidate QDs including a nearby alignment marker, and extraction of the relative coordinates of the QDs. Figure 4.4a shows a typical AFM height trace used for QD mapping. The QD appears as an elliptical elevation, as indicated by the white arrow.

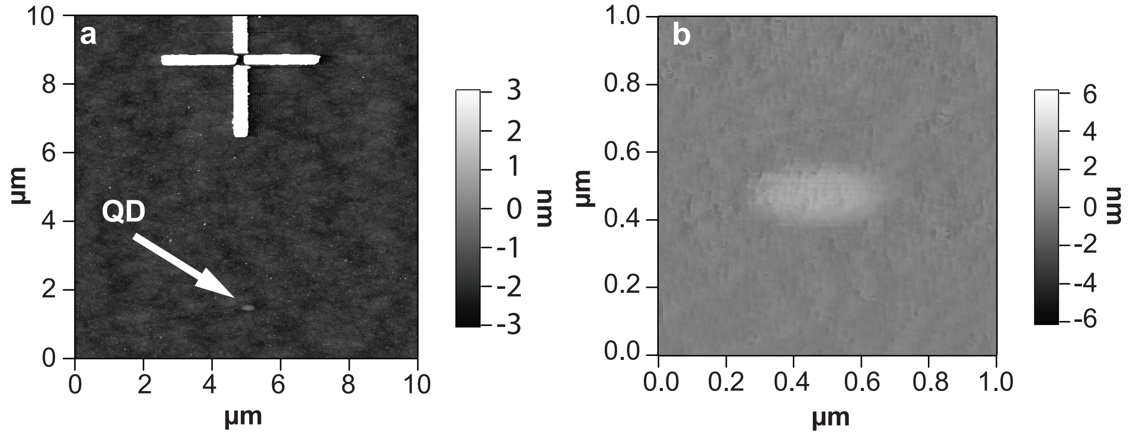

Figure 4.4.: **AFM height trace used for QD mapping.** **a**, A 10 × 10 μm^2 field containing a single QD (indicated by the white arrow) and a marker cross. **b**, Zoom-in of the hill formed on top of a single QD.

Usually, the QD can easily be distinguished from surface contaminants due to its characteristic elliptical shape. Moreover, Fig. 4.4a contains a marker cross, relative to which the QD coordinates are determined. Extraction of the QD coordinates is done by acquiring a zoomed-in scan of the QD as shown in Fig. 4.4b in order to obtain a high-resolution topography of the hill on the surface. The center of mass of this feature can then easily be determined, yielding the desired coordinates of the QD. In a similar fashion, the coordinates of the center of the marker cross are extracted.

A difficulty in determining the latter arises from the large height (~ 50 nm) of the gold marker on top of the sample. While the AFM traces a steep rising edge along the scan direction with high accuracy, a falling edge is typically washed out due to the inertia of the falling AFM tip after moving off the marker. When e.g. scanning from left to right in Fig. 4.4a, the left edge of the marker shows a pronounced slope, while the right edge is slightly smeared out. In order to overcome this problem, we typically obtained two scans in opposite scan directions, such that both the left and the right edges could be resolved by a steep rising edge.

6. Fabrication of PC defect cavities at the QD locations determined by AFM. The geometrical parameters of the PC structure are chosen such that the cavity-mode wavelength lies in close vicinity to the QD exciton transitions measured in step 4 (*lithographic tuning*).

For the successful positioning of PC defect cavities around single QDs with the required accuracy, a few technical key issues need to be addressed. One involves the correct interfacing between the atomic force microscope and the e-beam lithography machine used for cavity fabrication. As the internal length scales of the two devices are usually slightly different, one needs to gauge the conversion factor between them. To this end, a ruler scale of gold markers was written on the sample along with the alignment markers. An AFM image of such a ruler is shown in Fig. 4.5. Measurement

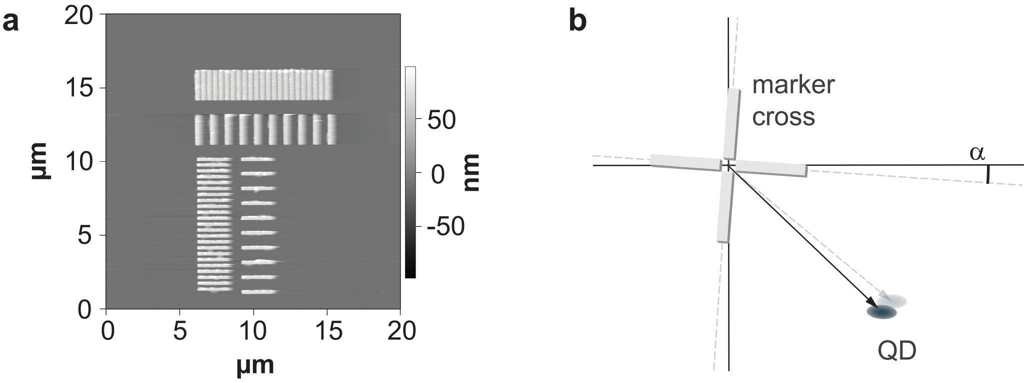

Figure 4.5.: Technical issues relevant for the AFM-mapping procedure. a, Marker ruler used for the conversion of the AFM length scales to those of the e-beam writer. From the given AFM micrograph the dimensions of the ruler in units of the AFM can be extracted. Comparison with the dimensions used in the e-beam writer yields the desired conversion factor. **b**, Problem of sample angular alignment within the AFM. Typically, the sample is slightly rotated with respect to the internal x and y axes of the AFM, which are used to determine the QD coordinates (indicated by the solid black lines). A precise measurement of the rotation angle α is hence required in order to determine the QD coordinates in the frame of the gold markers (dashed gray line).

of the dimensions of this ruler by AFM and comparing the results to the nominal design dimensions allows for proper conversion of the QD coordinates from “AFM units” to “e-beam units”. Obviously, this method requires that the same e-beam writer is used for fabrication of the gold markers *and* for writing the cavities.

The second issue involves the correct angular orientation of the sample within the AFM. A slight rotation of the sample chip with respect to the internal x and y axes of the AFM translates into a positioning error that scales linearly with the distance between QD and the alignment marker cross. Figure 4.5b shows this situation in detail: the solid black lines depict the x and y axes of the AFM, in which the coordinates of the QD are obtained. For lithography of the cavity structures, however, the QD coordinates in the frame of the gold markers are required (gray dashed lines). In order to obtain the correct conversion, an accurate measurement of the rotation angle α is required. In order to minimize the errors introduced by this procedure, it is of course desirable to start out with a close to optimum angular alignment of the sample. Since the AFM employed here does not provide control over the angular positioning of the sample, this had to be done manually, which lead to an alignment accuracy of $\sim 1^\circ$. The remaining error can then be compensated upon measurement of α. To this end we imaged gold marker features that were several millimeters long by recording two AFM images separated by a well-known distance of a few hundred μm. From these AFM traces α can be extracted and the QD coordinates in the frame of the alignment marker grid can be determined.

Eventually, cavity fabrication was done using a recipe developed by Kevin Hennessy at the University of California in Santa Barbara [65, 101]. Figure 4.6a shows an AFM height trace of a final device. In the center of the L3 defect, the slight

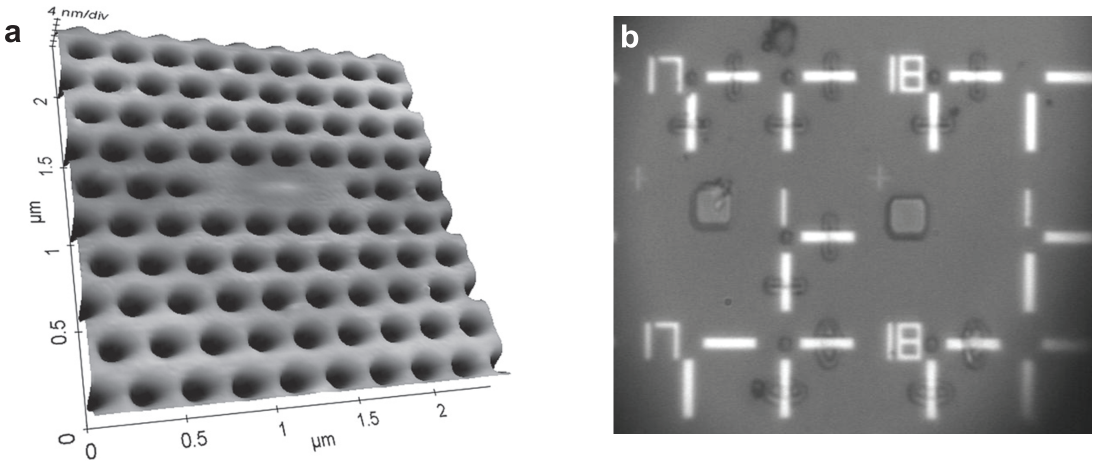

Figure 4.6.: Results of active cavity positioning. **a**, AFM topography of a final fabricated device. The elevation in the L3 defect center arising from the hill formed on top of the QD can clearly be seen. **b**, Optical micrograph showing a field (row 1, column 18) containing one PC cavity (square object) positioned to a QD. The marker cross used for QD mapping in Fig. 4.4a can clearly be seen in this image.

elevation heralding the presence of a single QD buried in the center of the cavity membrane can clearly be seen. The rounded edges of the PC holes are an artifact caused by the inertia of the AFM cantilever.

In our first fabrication run in 2006, we fabricated a total of ∼20 devices comprising L3 type PC defect cavities actively positioned around single QDs. Typical geometrical parameters of the cavities were $a = 260$ nm, $r = 60$ nm, and $d = 126$ nm. The devices were distributed over five chips, stemming from wafers grown by Antonio Badolato and Stefan Fält. From AFM images of the final devices like e.g. the one shown in Fig. 4.6a, the coordinates of the QDs within the L3 defect can be extracted. On average, we determined a positioning accuracy of 30 nm, allowing for a large number of devices having nearly optimal overlap with the cavity-mode electric-field maximum. Moreover, we measured cavity Q factors from 12 000 up to 30 000 in these devices, which are ∼ 20% larger than Q factors of cavities positioned using the stacking technique and the same cavity fabrication process. This observation suggests that the presence of a QD stack within the cavity mode volume indeed has a deteriorating effect on the cavity Q factor.

4.2. Spectral Tuning

Control of the mode wavelength of a nano-cavity is a challenging task in general. In a standard Fabry-Pérot resonator, one of the mirrors is typically mounted on a piezo actuator, thus allowing for external control of the cavity length and thereby of its resonance frequencies. In contrast, monolithically integrated cavities usually do not have mechanical degrees of freedom. A widely used strategy in solid-state cavity QED is the control of the QD-cavity detuning by changing the temperature of the host material, either locally [82] or by heating the entire chip [28, 29]. Since both the bandgap energy and the refractive index depend on temperature, this leads to a red shift both of the QD excitons *and* of the cavity mode. For GaAs-based PCs the temperature dependence of the former is stronger, such that changing the temperature mainly affects the QD lines, leading to a net red shift of the QD lines with respect to the cavity mode. In a solid-state environment, however, raising the temperature in general leads to increased phonon scattering and thereby to increased decoherence rates — a totally undesired effect. An alternative method is based on the electric control of the QD exciton energy via the quantum confined Stark effect [83, 104]. However, the technology of gating PC cavities was not available in the early days of this project.

Ideally, a tuning mechanism is desirable that tunes the resonant wavelength of the cavity mode, while the QD transitions remain unchanged. In fact, a major benefit of PC cavities is the relative ease at which these devices can be tuned even after fabrication. Since the resonant wavelength of a PC cavity mode depends only on the refractive index n of the material and on the geometrical parameters a, r, and t, a change of the structure geometry leads to a wavelength-shift of the cavity mode. Certainly, the geometry of the structure is initially designed such that the cavity mode is spectrally close to the QD excitons. Nevertheless, the finite accuracy of *lithographic tuning* demands an additional fine tuning mechanism. Such a mechanism can be implemented by post-fabrication modification of the cavity geometry, either by

- removal of material from the cavity structure by *wet digital etching*, leading to a *blue shift* of the cavity wavelength, or by
- deposition of extra dielectric material on the cavity membrane surface, leading to a *red shift* of the cavity wavelength,

while leaving the QD emission wavelength unchanged.

4.2.1. Digital Etching

The former technique - known as *wet chemical digital etching* - takes advantage of the native oxide layer of GaAs that forms when the sample is exposed to ambient air [26, 32] as shown in Fig. 4.7a. This ~ 1.5 nm thick oxide layer can easily be removed by immersing the sample into citric acid ($C_6H_8O_7$) for 15–60 s, which leads to a reduction of the membrane thickness t and an increase of the hole radii r and hence to a blue-shift of the cavity mode wavelength. As the H_2O hardly oxidizes the GaAs, etching stops once the oxide is fully removed. The process can be repeated upon re-oxidation of the GaAs surface by exposing the sample again to air. This allows for a *digital* etching procedure for fine-tuning of the cavity mode at a rate of $\sim$2.1 nm/cycle (numbers taken from [32]).

Digital etching proceeds in a well controlled and smooth manner, such that this method allows for tuning over tens of nanometers without a significant reduction of Q. Figure 4.7b shows a calibration curve of digital etching, reproduced from [32].

However, a disadvantage of the digital etching technique arises from the fact that the etching procedure has to be performed outside the cryostat. Each cavity tuning step therefore requires an interruption of the experiment. Moreover, although the

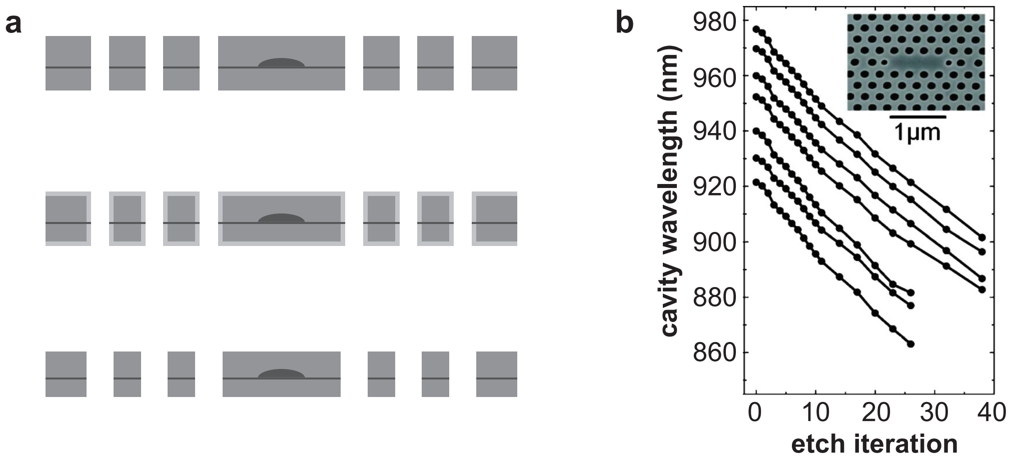

Figure 4.7.: Digital etching of a PC cavity. **a**, Wet chemical digital etching procedure: the final fabricated sample (top) undergoes oxidation of the first few monolayers on the sample surface when exposed to air (center). Immersion into citric acid removes the oxide layer, resulting in a change of the cavity geometry. The process can iteratively be repeated, providing tuning in digital steps. **b**, Calibration curve of digital etching for several L3 cavities as reproduced from [32]. Clearly, digital etching allows for tuning the cavity mode over several tens of nanometers.

digital nature of this tuning mechanism provides an advantage in terms of applicability, for more refined cavity QED experiments a fine tuning mechanism is required that allows for continuous tuning of the a cavity mode across an excitonic transition of the QD. Such a procedure is given by the gas adsorption mechanism presented in the next section.

4.2.2. Tuning by Gas Adsorption

As mentioned above, the cavity mode can be tuned to longer wavelengths by growing additional dielectric material on the sample surface. This can be achieved by the cryogenic adsorption of gas on the cavity membrane [34, 35, 105]. Since the sample is kept at $T = 4$ K during the experiments, it acts as an efficient getter pump for essentially all residual gas traces inside the cryostat vacuum chamber except for He and H_2. Gas molecules directed at the sample therefore adhere to the surface, forming a thin layer of dielectric material, as outlined in Fig. 4.8a. As a result the membrane thickness t is increased, while the hole radii r are reduced, thus leading to the desired red shift.

In fact, in many cryogenic setups this effect is automatically present due to the inferior quality of the cryostat isolation vacuum. In particular, outgassing from window glue and "dirty" surfaces within the direct line of sight of the sample can give rise to a background drift of the cavity mode [34] — in the context of this thesis this effect is referred to as *mode walking*. Figure 4.8b shows the time dependent drift of the cavity mode for various experimental situations. The Microstat®He flow cryostat by Oxford Instruments for example gave rise to significant mode walking as can be seen from the red bullets: within approximately three hours, the cavity mode

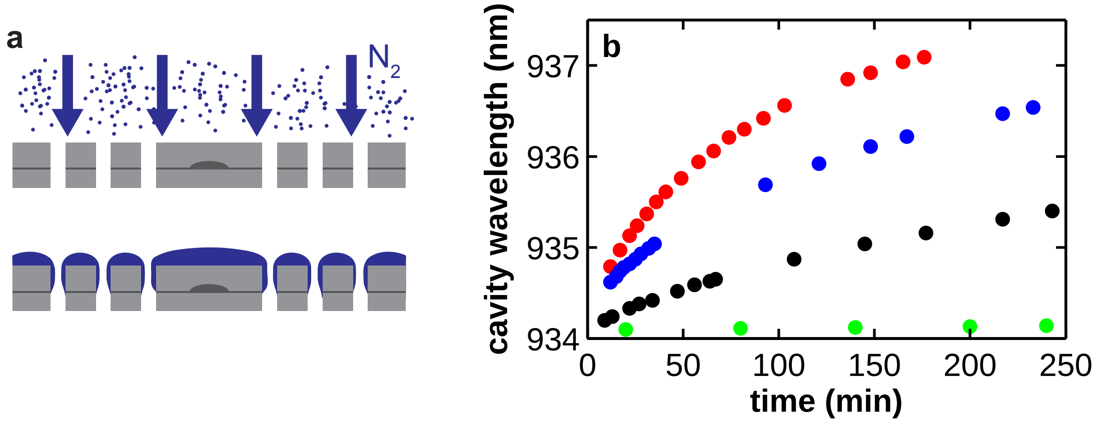

Figure 4.8.: Cavity tuning by gas adsorption. **a**, Schematic of gas adsorption tuning: gas molecules are gettered on the sample surface due to cryo-pumping. The ice layer accumulated in this fashion leads to a geometry change that results in a red shift of the cavity mode. **b**, Mode walking as a function of time for different experimental conditions: using the Oxford Microstat®He (red bullets), the same system after baking the chamber for six days (blue bullets), the same system with the sample mounted closer to the cryostat window (black bullet), and data obtained with the CryoVac system, in which the distance from the sample to the window can be reduced even further.

drifted as much as 3 nm. The cavity mode wavelength as a function of time follows a characteristic saturation behavior. A similar behavior is observed in [106], where the cavity mode wavelength is determined as a function of the ice-layer thickness. The saturation of the curves in Fig. 4.8b is most probably related to the saturation of the mode-walking effect with increasing layer thickness rather than to a saturation of the ice layer growth rate as a function of time.

On the one hand, mode walking provides a useful *automatic* tuning mechanism that in fact enabled multiple experiments presented in this thesis[1], on the other hand the inherent lack of control sets significant limits to experiments that require long integration times at a fixed detuning. It is therefore desirable to reduce mode walking as much as possible and introduce the gas for cavity tuning in a well-controlled way.

The main design principle towards the reduction of background gas adsorption is the improvement of vacuum conditions in the cryostat chamber. We found that the glue used for fixing the cryostat window acts as a major source for background gas traces in the cryostat vacuum chamber. In the second, more advanced setup used in this work, we therefore used EPO-TEK 353ND high-vacuum glue for fixing the window. The mode walking performance of the Microstat®He cryostat could be improved by baking out the cryostat front plate at ∼ 100 °C for approximately six days, which led to a slight reduction of mode walking, as can be seen from the blue bullets in Fig. 4.8b. Nonetheless, as long as no ultra-high vacuum conditions are met within the cryostat chamber, the mode walking is still considerable, owing to outgassing from the front plate. We found that the mode-walking rate could be further diminished by reducing the amount of material in the line-of-sight of the sample surface, from which the latter can getter background gas traces[2]. This can be achieved by moving the sample closer to the cryostat window. Moving the sample from a distance of ∼5 mm to ∼1 mm from the cyrostat window led to a significant reduction of mode walking, as can be seen from the black bullets in Fig. 4.8b.

---

[1] The data e.g. presented in [81, 107] were taken using mode walking

Finally, the Konti-Cryostat-Mikro from CryoVac Low Temperature Technologies Inc. gave rise to even less mode walking (green bullets in Fig. 4.8b). The significant advantage of this cryostat is the chamber design which allows for bringing the sample chip even closer to the front window as compared to the Microstat®He system from Oxford Instruments. Accordingly, mode-walking could be reduced even further. For a sample distance of ≈5 mm from the window, we measured a mode walking drift of 0.01 nm/h, which was reduced to a nearly undetectable value when bringing the sample even closer and baking the cryostat front plate for ∼20 hours. Reducing the distance to the window did not result in any instability of the sample temperature[3].

In the complete absence of mode walking, tuning is accomplished by introducing gas into the cryostat for the controlled growth of an ice layer. Experimentally, this is implemented by a gas feedthrough that allows for the controlled injection of ultra-clean molecular N_2 gas. In a pre-chamber connected to a Bayard-Alpert high-vacuum pressure gauge, a certain pressure of N_2 is prepared before releasing it onto the sample via a micrometer-screw driven metering valve. The system is stainless-steel based and all-metal sealed, thus allowing for maintaining high-vacuum conditions even for small tube diameters. A key criterion in designing the system is the need for a direct line-of-sight between the gas inlet and the sample surface, since cryogenic obstacles impeding the ballistic motion of the N_2 molecules reduce the efficiency of N_2 transfer onto the sample surface, which leads to a reduced tuning range. Consequently, the distance of the sample from the cryostat front window is subject to a trade-off: too large distances result in undesired mode walking, while too small distances reduce the efficiency of N_2 tuning.

Both the tuning range and the tuning speed achievable using *N_2 tuning* depend heavily on the pre-chamber pressure and the temperature of the sample. Higher pressures result in a larger flow of N_2, giving rise to faster tuning, and an increased sample temperature results in a larger shift per injected amount of gas. This is potentially due to an increased surface-mobility of N_2 molecules, allowing for a smoother film growth. While at $T = 4$ K we found the total tuning range to be limited to ∼3 nm, at $T = 25$ K we could tune the cavity wavelength up to 9 nm. This observation leads us to a practical procedure for tuning the cavity mode over wide ranges: first, we increase the sample temperature to about 25 K, tune close to the desired wavelength and then *freeze* the N_2 ice layer by cooling the sample back down to $T = 4$ K.

For small detuning ranges and in particular for fine tuning around a certain resonance, the metering valve used for the injection of N_2 allows for highly precise tuning of the cavity mode with an accuracy as good as or even better than the spectrometer resolution.

---

[2] Note that for typical cryostat dimensions at high vacuum conditions the regime of molecular gas flow is realized. Accordingly, the mean free path of gas traces in the chamber is much larger than the separation between surfaces of the cryostat and the sample.

[3] A significant change in the sample temperature can be observed via a shift of the QD PL lines.

5. Observation of Strong Coupling

The findings presented in this chapter were published in Nature [81].

As discussed in Sec. 4.1, the deterministic positioning scheme developed in the framework of this thesis allowed for the fabrication of several coupled cavity QED systems in which a *single* quantum dot was located in the center of a PC defect cavity in the L3 configuration. The latter design was selected due to its promising properties for reaching the strong coupling regime of cavity QED: the fundamental mode of the L3 cavity supports both an ultra-small mode volume of $V_{\mathrm{eff}} = 0.7 \cdot \left(\frac{\lambda}{n}\right)^3$ and a large theoretical Q factor of $Q \sim 3 \cdot 10^5$ [86].

In this chapter we investigate a single QD-cavity device and study its PL spectra, demonstrating strong coupling between the QD and the cavity mode. Figure 5.1a shows an AFM height trace obtained from this particular device after cavity fabrication. Like in Fig. 4.6 one can clearly identify a slight "hill" in the center of the

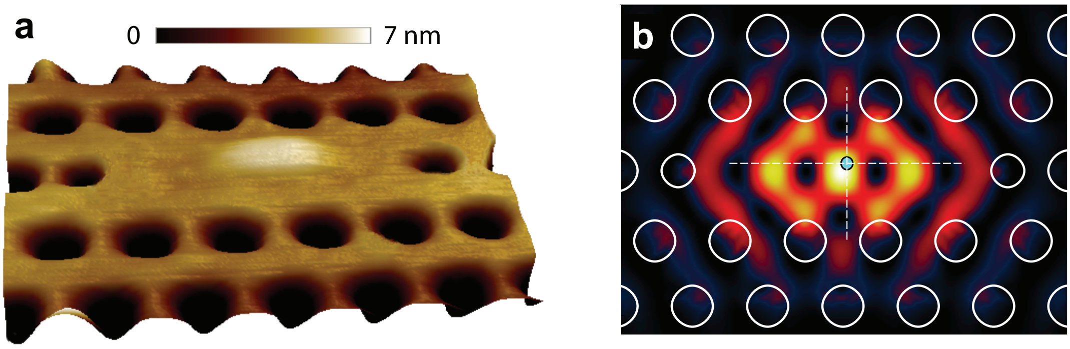

Figure 5.1.: A QD-cavity device. a, AFM height trace showing the surface structure of the device. **b**, FDTD simulations of the L3 cavity electric field distribution. The cross indicates the location of the QD derived from **a**. The QD is slightly off center with $|\boldsymbol{\varphi}(\boldsymbol{r}_{\mathrm{QD}})| \sim 70\%$.

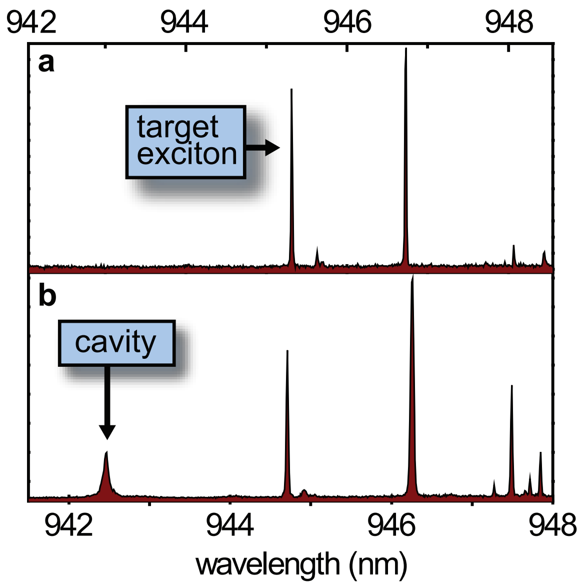

Figure 5.2.: PL spectra of the QD-cavity device. **a**, PL spectrum of the QD prior to and **b**, after cavity fabrication. The presence of the cavity is indicated by the additional PL peak. The system was excited at $\lambda_{\mathrm{ex}} = 780$ nm with a pump power below the saturation power of the QD.

L3 defect that protrudes ~1 nm from the sample surface and indicates the presence of a buried QD about 63 nm below the sample surface. From the AFM picture we learn that the QD is located slightly off-center. The extracted relative coordinates of the QD within the L3 defect and an FDTD simulation of the cavity field (Fig. 5.1b) indicate that the electric field experienced by the QD amounts to $|\boldsymbol{\varphi}(\boldsymbol{r}_{\mathrm{QD}})| \sim 70\%$ of the maximum value in the center of the defect. Hence we expect a vacuum Rabi splitting of approximately 70% of the maximum possible value. Morevoer, the cavity mode is initially ~5 nm blue detuned from the bluest QD line, such that the cavity mode can easily be tuned into resonance with the QD excitons using gas adsorption.

5.1. Vacuum Rabi Splitting

In order to investigate the optical properties of the device presented above, PL measurements as described in Sec. 3.1 were carried out. Figure 5.2 shows PL spectra of the device under investigation before (a) and after (b) cavity fabrication. In order to obtain these measurements, the GaAs host material was excited above bandgap ($\lambda_{\mathrm{ex}} = 780$ nm) with a pump power below the saturation power of the QD. Clearly, the excitonic emission lines of the QD do not undergo considerable qualitative changes when fabricating the cavity. The only observable difference in the QD spectrum is a slight blue shift of the QD excitons after cavity fabrication. This observation can most likely be explained by slightly different sample temperatures in the two experiments. However, the PL spectrum of the final device (Fig. 5.2b) exhibits an additional emission line that is related to PL emission from the uncoupled cavity mode. A Lorentzian fit yields a Q factor of $Q \approx 13\,000$, as roughly expected according to measurements performed on calibration samples[1]. Furthermore, the intensity of the peak increases far above the saturated intensities of the QD s-shell lines when increasing the pump power. Moreover, as expected the cavity peak undergoes a redshift as a function of time due to gas adsorption on the cavity membrane (*mode walking*).

The occurrence of this extra peak is by itself a rather surprising observation. In the case of an incoherently pumped two-level atom, one expects excitation of the cavity mode to occur only if a resonance condition between the optical transition of the atom and the cavity mode is met[2]. In the present case, however, it is clear from a comparison of Figs. 5.2a and 5.2b that the QD does not support a discrete optical transition at the spectral location of the cavity mode. Nonetheless, efficient emission of the off-resonant cavity mode can be observed with a weak dependence on the detuning from the QD excitons as the cavity mode undergoes mode walking. In fact, the same observation was made on all other fabricated devices in which a large range of QD-cavity detunings was realized.

Off-resonance PL emission of a cavity mode was reported in essentially all previous studies of cavity QED systems involving QDs in microcavities [28–30, 100, 108]. In contrast to the experiments presented here, however, in all these reports the cavity typically contained a large number of QDs. Obviously, in such a situation there is a significant likelihood of establishing a near-resonance condition with some transition of at least one QD. Therefore, this effect seemed to be explainable by the large number of QDs involved and did not receive much further attention. Nonetheless, also the single-QD devices fabricated by the stacking technique described in Sec. 4.1 showed off-resonance cavity-mode emission [26, 65]. In this situation, the observation of the latter was related to the presence of a quasi-continuum of excited states of the stacked QDs. As a matter of fact, these arguments even provided a motivation in favor of the stacking technique: the stack was assumed to be not only beneficial for positioning, but also for enabling the spectroscopic investigation of the off-resonant cavity mode by simple PL.

In stark contrast, in the present situation only a single QD is located within the cavity mode volume. Hence, off-resonant cavity emission cannot be explained by the presence of multiple QDs. From more refined experimental investigations it is indeed possible to unequivocally relate the off-resonance cavity mode emission — in this context typically referred to as *cavity feeding* — to the presence of a single QD. Given the artificial atom nature of the QDs, this conclusion seems rather contradictory at first sight and hence gave rise to a vivid discussion in the community. A detailed discussion of the experimentally observed features together with a microscopic model of *cavity feeding* is given in Chap. 7. Here, we focus on the resonant behavior of the strongly coupled QD-cavity system, in which cavity feeding merely provides a means to observe the cavity mode in PL even when being off-resonant from the QD excitons.

---

[1] Again, it has to be remarked that the experimentally observed Q factor is approximately one order of magnitude smaller than the theoretical value.

[2] As an example consider the simulated PL spectra of a two-level atom strongly coupled to a cavity mode, shown in Fig. 2.3a. Incoherent excitation of the atom only leads to emission from the cavity mode, when the cavity mode is moved on resonance with the atom.

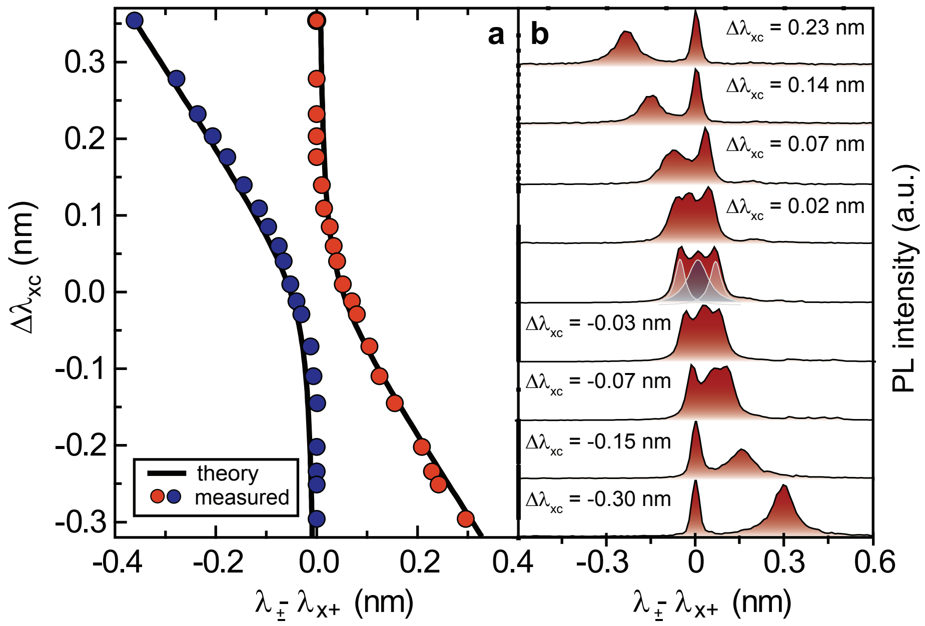

Figure 5.3.: Observation of vacuum Rabi splitting. **a**, The filled circles show the peak positions of the PL peaks shown in **b** for various detunings $\Delta\lambda_{\mathrm{xc}}$ of the cavity mode from the X^{1+}. The anticrossing related to vacuum Rabi splitting can clearly be seen. The solid black lines show a fit using Eq. (5.2), where g is the only fit parameter. **b**, Spectra of the two anticrossing polariton states near zero detuning. An additional peak is identified as the pure photonic state of the cavity mode. The $\Delta\lambda_{\mathrm{xc}}$ values are indicated for each spectrum.

In order to tune the cavity mode on resonance with the nearest exciton line of the QD we employ the *mode-walking* technique described in Sec. 4.2.2. Subsequent detailed studies of QD emission lines in the coupled QD-cavity device allow us to assign this QD line to the positively charged trion X^{1+} (Chap. 6). Figure 5.3b shows PL spectra recorded for different exciton-cavity detunings $\Delta\lambda_{\mathrm{xc}} = \lambda_{X^{1+}} - \lambda_{\mathrm{cav}}$. For $\Delta\lambda_{\mathrm{xc}} > 0.05$ nm, the short-wavelength spectral feature remains cavity-like with a linewidth of $w_- \approx w_{\mathrm{cav}} = 0.071$ nm, corresponding to $\hbar\kappa = 100$ μeV ($Q \approx 13\,300$) and the long-wavelength peak retains its excitonic nature with $w_+ \approx w_x = 0.025$ nm ($\hbar\gamma = 35$ μeV). Here, w_{cav} (w_x) denotes the bare cavity-mode (exciton) linewidth[3]. As the cavity mode approaches the exciton, the short-wavelength feature broadens and then separates into two distinct peaks. As tuning proceeds, the middle peak preserves exactly the wavelength, linewidth, and polarization of the cavity mode when moving across resonance, while the long- and short-wavelength peaks repel each other and assume equal linewidths of $w_\pm = 0.042$ nm $\approx (w_{\mathrm{cav}} + w_x)/2$ on resonance. The two outer peaks anticross at $\Delta\lambda_{xc} = 0$ and can therefore be identified as the polariton states

$$|p_\pm\rangle = \frac{1}{\sqrt{2}}\left(|X^{1+}, 0_c\rangle \pm |g, 1_c\rangle\right) \tag{5.1}$$

---

[3] The value of w_x is close to the spectral resolution of ≈ 21 pm of our spectral apparatus.

of the strongly coupled exciton-photon system, the resonant frequencies $\Omega_\pm$ and linewidths $\Gamma_\pm$ of which are given by

$$\Omega_\pm + i\frac{\Gamma}{2} = \frac{\omega_{\mathrm{cav}} + \omega_{X^{1+}}}{2} - i\frac{\gamma+\kappa}{4} \pm \sqrt{g^2 + \frac{1}{4}\left((\omega_{\mathrm{cav}} - \omega_{X^{1+}}) - i\frac{\gamma-\kappa}{2}\right)^2}. \quad (5.2)$$

In Fig. 5.3a we plot the peak positions of the polariton peaks obtained from the PL spectra as solid circles and fit the data with Eq. (5.2) by using κ and γ given above and using g as the only fit parameter. The fit is shown as the solid black lines in Fig. 5.3a and yields $g = 76$ μeV. Obviously, the agreement with the measured peak positions is excellent. Owing to the slight spatial mismatch between the QD and the cavity electric-field maximum, g is reduced to $\sim 70\%$ of its maximum possible value. Furthermore, a similar anticrossing was observed on another exciton peak of the same device that is red detuned by ~ 1.5 nm from the X^{1+}. The vacuum Rabi splitting observed on this transition amounted to $g = 120$ μeV. Given the larger vacuum Rabi splitting observed on this line and its detuning with respect to the X^{1+}, we assign it to the X^0 transition.

From the observation of the characteristic polariton anticrossing related to vacuum Rabi splitting and the fact that $g > |\gamma - \kappa|/4$, we conclude that the device at hand is indeed in the strong coupling regime of cavity QED. However, the predicted strong-coupling emission spectrum only accounts for two of the three peaks observed experimentally. We attribute the third peak to the pure photonic state of the cavity, since it exhibits both the linewidth and the polarization properties of the cavity mode, and since it dominates over the QD spectral lines when increasing the pump power. We argue that the occurrence of the third peak in the strong coupling spectrum is a natural consequence of the effect of off-resonant cavity-feeding introduced above. The presence of multiple exciton peaks in the QD PL spectrum indicates that the QD charges from time to time and hence its optical transition frequency fluctuates randomly. The cavity is resonant with the X^{1+} transition and leads to vacuum Rabi splitting only when the QD contains an extra hole. However, at times when the QD is uncharged or occupies a different charging state, the cavity mode reverts to its uncoupled spectral location and linewidth, thus contributing to the central, pure photonic peak in the strong-coupling spectrum via the off-resonant cavity-feeding effect. In our experiments, integration of the PL signal occurs over ~ 1 s, such that the observed spectra constitute a time-average of the two regimes, resulting in the observed spectral triplet.

A similar three-peak feature has been observed in experiments dealing with an ensemble of Ba atoms strongly coupled to a high-finesse cavity [109]. There the third peak is due to fluctuations in the number of emitters coupled to the cavity mode. Our experiment constitutes a solid-state analogue of this scenario, in which fluctuations of the emitter frequency, rather than emitter number, occur over time.

5.2. Modification of Lifetime

Besides inducing the vacuum Rabi splitting, strong coupling also leads to an enhancement of the spontaneous QD relaxation rate when the cavity moves on resonance with the QD. This behavior is reflected in the detuning dependence of the

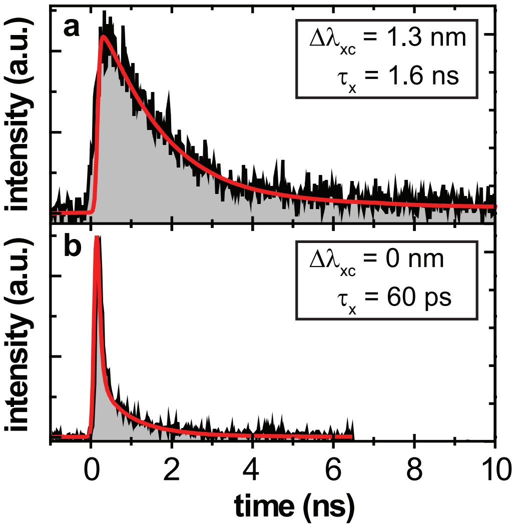

Figure 5.4.: Observation of lifetime reduction. X^{1+} PL decay curves when the cavity is **a**, blue detuned by $\Delta\lambda_{\text{xc}} = 1.3$ nm and **b**, resonant with the X^{1+}.

imaginary part $\Gamma_{\pm}$ of the polariton eigenfrequency given in Eq. (5.2). Moreover, it is particularly pronounced in a photonic crystal environment, where the presence of a photonic bandgap results in the depletion of the optical density of states, thus leading to an enhanced lifetime of a QD exciton when off-resonant from the cavity mode. This is confirmed by a measurement of the X^{1+} PL decay time at large detuning ($\Delta\lambda_{\text{xc}} = 4.1$ nm) using the TCSPC technique presented in Sec. 3.1.3. At this detuning, the QD X^{1+} population undergoes exponential decay $P_{X^{1+}}(t) \sim \exp(-t/\tau_{X^{1+}})$ with a time constant of $\tau_{X^{1+}} = 8.7$ ns, significantly longer than the typical QD lifetime in bulk material of $\tau_0^{(bulk)} \approx 1$ ns.

When the cavity is tuned towards resonance with the X^{1+}, $\tau_{X^{1+}}$ decreases following the dependence given in Eq. (5.2). For a detuning of $\Delta\lambda_{\text{xc}} = 1.26$ nm, we measure $\tau_{X^{1+}} = 1.6$ ns which further decreases down to a resolution limited $\tau_{X^{1+}} = 60$ ps on resonance (see Fig. 5.4). This strong lifetime reduction by a factor of 145 confirms the spectral evidence that the exciton-photon coupling g is sufficiently large for the system to be in the strong-coupling regime.

In order to obtain an independent estimate of g from lifetime measurements, $\tau_{X^{1+}}$ was determined for several detunings $\Delta\omega_{\text{xc}}$ and the experimental data was fit by

$$\frac{\hbar}{\tau_{X^{1+}}} = \gamma_0 + \frac{4g^2}{\kappa}\frac{\kappa^2}{4\Delta\omega_{\text{xc}}^2 + \kappa^2}, \tag{5.3}$$

where γ_0 refers to the background spontaneous emission rate into modes other than the cavity mode. Eq. (5.3) corresponds to an expansion of Eq. (5.2) for large detuning $\Delta\omega_{\text{xc}} \gg g, \kappa, \gamma$ and reflects the detuning-dependent Purcell effect [43]. The best fit is obtained for $\gamma_0 = 0.05$ μeV, corresponding to $\tau_0 = 13.2$ ns, and $\hbar g = 90$ μeV. The latter value agrees well with the value $\hbar g = 76$ μeV measured from the vacuum Rabi splitting shown in Fig. 5.3.

5.3. Quantum Nature

The measurements presented above prove unequivocally that the QD-cavity system under investigation operates in the strong coupling regime. However, the calculated two-peak lineshape given in Eq. (5.2) also describes two coupled classical harmonic oscillators [110]. Therefore, vacuum Rabi splitting alone is not sufficient to discriminate between a quantum regime arising from the interaction of single exciton and photon quanta, and a classical regime describing the coupling behavior of two classical harmonic oscillators. The striking difference between the two regimes is manifested in the level spectrum for cavity occupation numbers above one: while the quantum non-linear regime is characterized by the distinct $\sqrt{n}$ anharmonicity of the Jaynes-Cummings ladder spectrum (see Sec. 2.1.1), a system composed of two coupled classical oscillators retains a harmonic level spectrum also for large cavity photon numbers. A generic example for the latter regime is given by a quantum well strongly coupled to a microcavity. In the low excitation regime, the excitonic system exhibits bosonic statistics allowing for the excitation of multiple polaritons at the same energy.

A striking feature of the quantum nonlinear regime is the occurrence of *photon blockade* [111]: due to the anharmonicity of the Jaynes-Cummings ladder spectrum, each of the lowest lying polariton transitions comprises a quasi-isolated two-level system, the relaxation of which results in the emission of single photons. Optical transitions to higher manifolds on the other hand occur at different frequencies due to the anharmonic $\sqrt{n}$ dependence of the higher excited polariton states. As a result, the photon stream emitted from a cavity QED system in the quantum nonlinear regime therefore exhibits *antibunching*. In contrast, the emission from a system exhibiting a harmonic level scheme — like a system comprised of two coupled classical oscillators — should show *super-Poissonian* statistics due to the potential occurrence of multi-photon emission events at the same transition frequency. A distinction between the two regimes can thus be obtained from a measurement of the second order auto-correlation function $g^{(2)}_{\mathrm{cav}}(\tau)$ of the cavity photon stream.

In order to prove the quantum nature of the QD-cavity system at hand, we hence tune the cavity mode on resonance with the X^{1+} transition and carry out a photon auto-correlation measurement of the entire resonant three-peak structure following the methods outlined in Sec. 3.1.4. For this measurement, the system was excited slightly below saturation of the QD using pulsed excitation, in order not to be limited by the time jitter of the APDs. As can be seen in Fig. 5.5, the photon stream emitted from the cavity mode exhibits sub-Poissonian statistics with a central peak area at $\tau = 0$ that is only 54% of the average peak area for other time delays, such that $g^{(2)}_{\mathrm{cav}}(0) \approx 0.54$. The presence of sub-Poissonian statistics provides evidence for the system being in the quantum anharmonic regime.

However, the emission from the strongly coupled device does not show the behavior of a single photon source, for which one would expect $g^{(2)}_{\mathrm{cav}}(0) = 0$. We argue that the experimentally observed $g^{(2)}_{\mathrm{cav}}(0) > 0$ is caused by two mechanisms. First, the spectral window analyzed by the HBT apparatus in order to estimate $g^{(2)}_{\mathrm{cav}}(\tau)$ has two contributions: the strongly coupled polariton peaks and the central peak arising from the uncoupled cavity mode. In fact, a three Lorentzian fit to the data (as indicated in the $\Delta\lambda_{\mathrm{xc}} = 0$ curve in Fig. 5.3b) reveals that the latter contributes $\sim$45% of

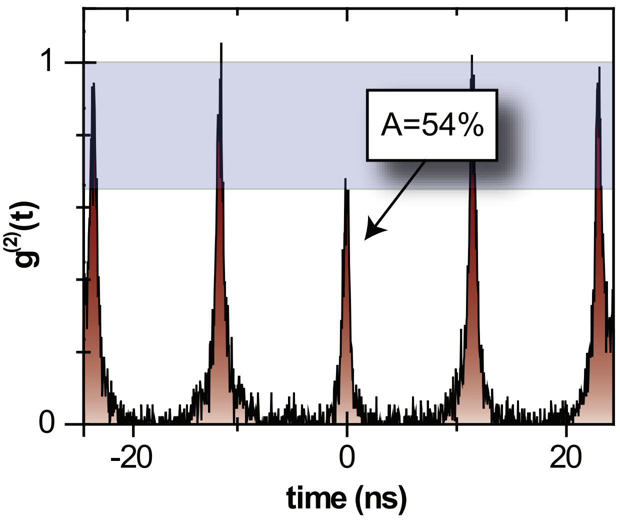

Figure 5.5.: Measured auto-correlation of the strongly coupled system. Auto-correlation $g^{(2)}_{\text{cav}}$ of the entire three-peak structure on resonance. We observe antibunching with $g^{(2)}_{\text{cav}} = 54\%$, indicative of the system being in the quantum non-linear regime.

the total collected PL. A possible explanation for the finite $g^{(2)}_{\text{cav}}(0)$ could therefore arise from the contribution of the uncoupled cavity mode, which was not further understood at this point. Second, in strong coupling the carrier-capture process occurs on timescales similar to the polariton decay time ($\tau_{\pm} \approx 2\hbar/\kappa \approx 13.3$ ps), such that it is possible for the system to undergo multiple capture/emission events per excitation pulse on timescales shorter than the timing resolution of the correlation setup.

The first hypothesis was confirmed by studying $g^{(2)}_{p+}(\tau)$ of the upper polariton branch $|p_+\rangle$ alone. To this end a different device was used that exhibits larger vacuum Rabi splitting with a nearby exciton transition ($\hbar g = 110$ μeV) the nature of which remained unknown. For the measurement, we slightly red detuned the cavity from perfect resonance with the exciton in order to facilitate spectral filtering of the upper polariton branch (the one of the vacuum Rabi-split polariton peaks with higher energy) and use a diffraction grating with higher spectral resolution. Figure 5.6a shows a PL spectrum of the resonant strong-coupling feature of the studied device. The green bar indicates the spectral window of the photons collected for the measurement of $g^{(2)}_{p+}(\tau)$. Although the pure photonic state of the cavity is slightly off-resonant and thus has a reduced contribution to the collected signal ($\sim 15\%$), the excitonic and photonic contributions of the upper polariton state are still well-balanced: the state can be written as $|\Phi_1^+\rangle = \alpha|X,0\rangle + \beta|g,1\rangle$, where $|\alpha|^2 = 56\%$ and $|\beta|^2 = 44\%$ are the probability amplitudes of the excitonic and the photonic parts, respectively. These numbers were in turn extracted from the three-Lorentzian fit shown in Fig. 5.6b.

Figure 5.6c shows the result of an auto-correlation measurement $g^{(2)}_{p+}(\tau)$ of the upper polariton emission. Clearly, the central peak is now significantly reduced to $g^{(2)}_{+}(0) = 19\%$ as compared to the measurements, in which the full contribution of

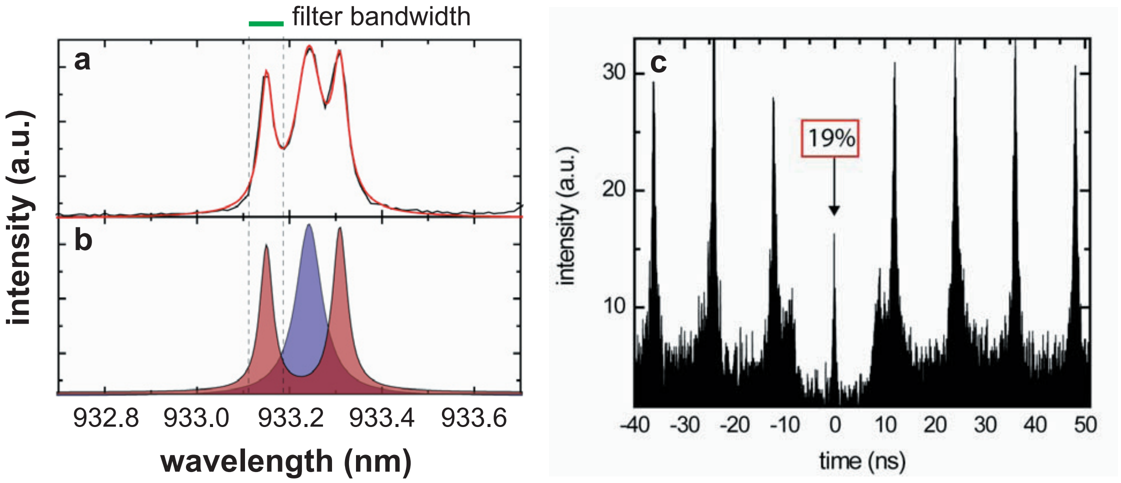

Figure 5.6.: Spectral filtering of a single polariton. PL spectrum of the device used for the measurement of $g^{(2)}_{p+}(\tau)$ of the upper polariton branch. **a**, Measured PL spectrum (black line) together with a three-Lorentzian fit (red line). The contributions of the individual peaks are shown in **b**. From the peak locations, we extract the contributions of the excitonic and the photonic channel to the polaritons. **c**, Auto-correlation $g^{(2)}_{p+}(\tau)$ of the upper polariton emission using narrow spectral filtering. Here, we measure $g^{(2)}_{p+}(0) = 19\%$, demonstrating that the finite correlations at $\tau = 0$ mainly arise from the pure photonic state of the cavity.

the pure photonic state of the cavity was included. The two shoulders at ±10 ns we attribute to secondary emission and cross-talk of the avalanche photodiodes.

These observations clearly show that the finite $g^{(2)}_{\mathrm{cav}}(0)$ presented above arises mainly from the contribution of the uncoupled cavity peak, thus proving that the cavity field attains an anharmonic character when brought into strong coupling with an excitonic transition, and thus proving the quantum nature of the strongly coupled QD-cavity device.

In conclusion, the results presented in this chapter prove that the devices fabricated using the active positioning scheme introduced in Chap. 4 operate in the strong coupling regime and exhibit genuine quantum dynamics.

6. Cavity QED as a Tool for Quantum Dot Spectroscopy

The main findings presented in this chapter were published in Physical Review Letters [107].

At the time of the first demonstration of strong coupling in our QD-cavity systems (Chap. 5), the charge configurations of the excitons the cavity mode was resonantly coupled to was not well understood. The same statement holds for essentially all previously reported experiments by our or other groups dealing with QDs coupled to nanocavities. This shortcoming is mainly due to the fact that the inherently random carrier excitation process used in PL spectroscopy creates a multitude of different QD charge configurations, such that the emission spectra are generally difficult to interpret. This is particularly true when multiple QDs are present within the cavity, as it is the case in experiments relying upon random positioning of cavities on medium to high QD-density samples [28, 30, 43, 67, 75, 82, 100, 108]. However, this ambiguity has not hindered progress in the field, since the emphasis in these experiments was on using the QD as a simple two-level emitter coupling to a cavity mode. The nature of the particular QD transitions used was irrelevant for the study of cavity QED physics.

In contrast, we show here that a nanocavity strongly coupled to QD transitions allows for studying fundamental properties of the QD itself. Enabled by the advantage of having only a single QD present in the cavity, the "clean" PL spectra observed in this case allow us to study the strong-coupling dynamics of different QD excitonic transitions in more detail. Spectral anticrossings observed when tuning the cavity mode across certain resonances allow us to unambiguously identify the most prominent QD exciton transitions, as presented in Chap. 2.2.3: the single positively charged trion (X^{1+}), the neutral exciton (X^0), and the neutral biexciton (XX^0). Moreover, cavity QED allows us to study the fine structure of these QD transitions in detail. As a result, we discover a novel strong-coupling induced mixing of bright and dark excitons of the neutral QD. In this setting, cavity QED provides a powerful spectroscopic tool for the study of QD physics.

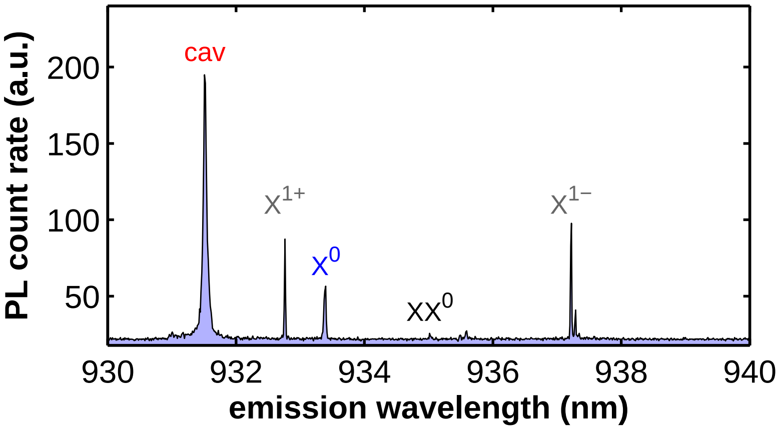

Figure 6.1.: Typical PL spectrum of the device studied here. Along with the off-resonant cavity-mode emission, a few QD transitions are visible to which the cavity mode can couple. Tuning of the cavity mode can be accomplished by gas adsorption.

6.1. Strong-Coupling PL for Different Excitons

In this chapter, we perform cavity-QED experiments with a strongly coupled device that exhibits close to perfect positioning within the cavity mode. From AFM topographies we find that the QD is located precisely in the center of the L3 defect such that $|\varphi(\boldsymbol{r}_{QD})| \approx 1$. Fig. 6.1 shows a PL spectrum of the device, obtained by exciting the GaAs host material with the MIRA-900 tunable titanium-sapphire laser at a wavelength of $\lambda_{\text{ex}} = 818$ nm, slightly above the GaAs bandgap. The laser beam is focused to a diffraction-limited spot and delivers a power of $P_{\text{ex}} = 5$ nW to the sample surface. One can clearly see the off-resonance cavity-mode emission at $\lambda_{\text{cav}} = 931.5$ nm together with a few exciton lines stemming from the QD. The cavity luminescence peak exhibits a Lorentzian lineshape with a Q factor of $Q = 16\,000$ ($\kappa = 83$ μeV) and is predominantly polarized along the y direction (degree of polarization $= 96\%$), i.e. perpendicular to the L3 defect line. Since the cavity mode is initially blue-detuned from the excitons, we can in principle tune the cavity mode in resonance by the gas-adsorption technique discussed in Sec. 4.2.2. Here, we rely on the intrinsic *mode-walking* effect, i.e. on the automatic redshift of the cavity mode over time, allowing us to continuously move the cavity mode across the QD excitons while repeatedly taking spectra.

Figure 6.2 shows the result of a corresponding measurement in a false-color plot. In each spectrum, the central wavelength of the (uncoupled) cavity mode was extracted and used to linearize the vertical axis. Furthermore, since the total intensity of the spectrum fluctuates in time as a result of sample drift, each spectrum was normalized to its integral. The data were taken with a polarizer in the PL collection arm oriented along the y direction in order to maximize the signal from the cavity mode.

The diagonal line corresponds to the uncoupled cavity mode (c.f. Sec. 7.1.1). The two vertical lines at $\lambda = 932.8$ nm and $\lambda = 933.4$ nm exhibit a large anticrossing

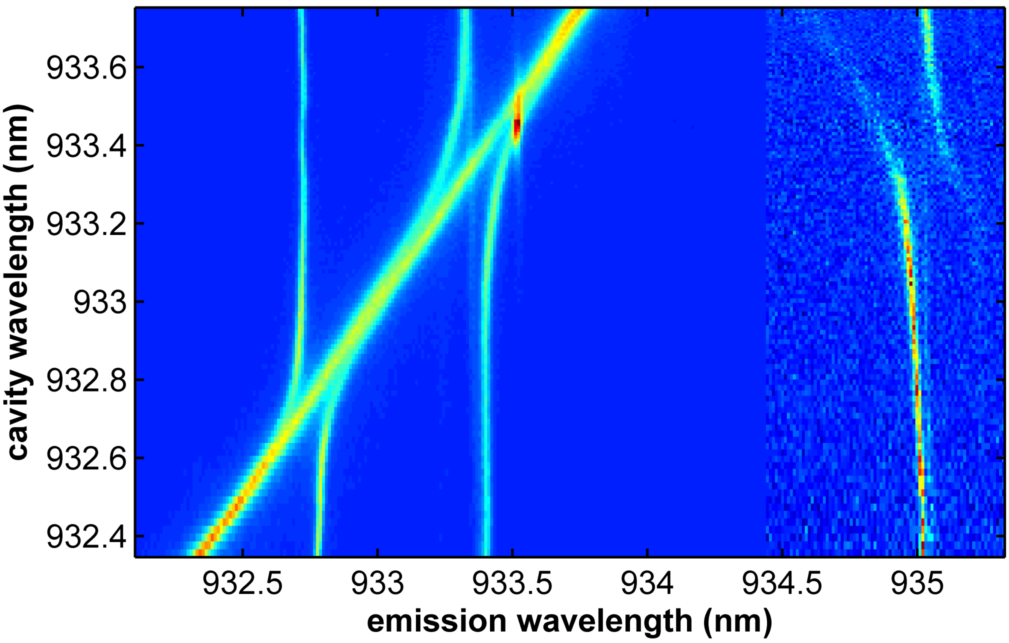

Figure 6.2.: Strong-coupling anticrossing curves for different QD lines. PL color plot when the cavity mode is tuned across the X^{1+} and the X^0 transitions. For both lines a clear anticrossing can be identified. For wavelengths to the red of 934.5 nm the color scale has been offset by a factor of 26 in order to highlight the biexciton emission.

when the cavity moves into resonance, indicative of of the system undergoing vacuum Rabi splitting. The blue line shows a splitting of $2g = 205$ μeV while that of the red line is $\sim$1.5 times larger and amounts to $2g = 316$ μeV, which is, to the best of our knowledge, the largest vacuum Rabi splitting reported so far in any cavity-QED system with a single emitter. We also note here, that the uncoupled cavity emission again gives rise to a third central peak on resonance, as previously observed in Fig. 5.3. Furthermore, it can clearly be seen that the anticrossing at $\lambda = 933.4$ nm exhibits additional features as compared to the anticrossing at 932.8 nm. Finally, there is a faint additional line at $\lambda = 935$ nm that undergoes a splitting when the cavity is on resonance with the X^0. Due to the smaller intensity of this line, the color scale of Fig. 5.3 was re-normalized for wavelengths longer than 934.5 nm. These observations allow for conclusions both on the nature and the fine structure of the three QD transitions.

The complex anticrossing feature at $\lambda = 933.4$ nm is consistent with the fine structure expected form the neutral exciton X^0. As has been discussed in Sec. 2.2.3, the X^0 emission consists of a doublet of orthogonally polarized lines, split by the x-y splitting δ. The two emission features stem from two orthogonally oriented dipoles in the QD-plane that correspond to the neutral exciton states

$$|X^0_{x,y}, 0_c\rangle = \frac{1}{\sqrt{2}} \left(|+1\rangle \pm |-1\rangle \right) \otimes |0_c\rangle, \tag{6.1}$$

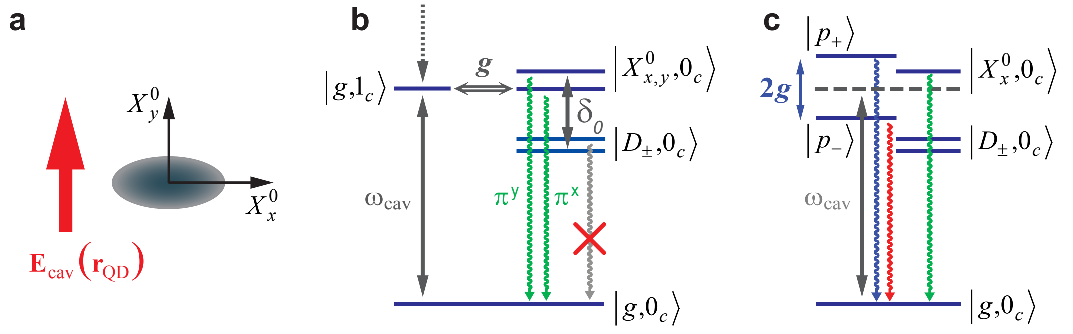

Figure 6.3.: The cavity mode interacting with the X^0. **a**, Alignment of the exciton axes with respect to the cavity-mode electric field. The y polarized component of the X^0 is parallel to the electric field vector. **b**, Eigenstates of the QD and the cavity mode. **c**, Since the cavity electric-field vector is parallel to the y direction at the QD, coherent coupling g occurs with $|X^0_y, 0_c\rangle$, giving rise to the polariton states $|p_\pm\rangle$ while $|X^0_x, 0_c\rangle$ is not influenced by the cavity mode.

where $|0_c\rangle$ denotes the empty cavity mode. The cavity electric field at the location of the QD is linearly polarized and is oriented perpendicular to the defect line (y direction) in the exact center of the L3 cavity, as indicated in Fig. 6.3a. When the cavity mode is tuned into resonance with the X^0, strong coupling with the cavity-mode single-photon state $|1_c\rangle$ can only occur with the excitonic dipole that is oriented parallel to the electric field of the cavity mode, i.e. with $|X^0_y, 0_c\rangle$ in this case. This is schematically indicated in Fig. 6.3b. As a result, the y oriented exciton undergoes strong coupling and creates a vacuum Rabi split doublet of polariton states

$$|p_\pm\rangle = \frac{1}{\sqrt{2}}\left(|X^0_y, 0_c\rangle \pm |g, 1_c\rangle\right), \tag{6.2}$$

while leaving the uncoupled state $|X^0_x\rangle$ unchanged, as indicted in Fig. 6.3c. As a result, this state does not undergo any frequency shift as the cavity-mode detuning changes.

This fine structure is exactly what we observe for the central QD line at $\lambda_{X^0} = 933.4$ nm: in addition to the emission originating from the vacuum Rabi split doublet $|p_\pm\rangle$, we observe a faint vertical emission line that does not shift as the cavity is tuned across resonance and that we hence attribute to the uncoupled exciton state $|X^0_x, 0_c\rangle$. Further evidence comes from the polarization behavior of the emission: as the polarizer in the PL detection path is rotated, the emission from this central line increases and dominates the spectrum when oriented orthogonal to the polarization direction of the cavity mode emission. Figure 6.4 shows a zoom-in of the X^0-cavity anticrossing for two different polarizations. In Fig. 6.4a the polarizer is oriented parallel to the cavity polarization (as in Fig. 6.2), whereas in Fig. 6.4b it is rotated by 55°, in order to make the emission from both the uncoupled exciton and the polariton features visible in the same spectrum. This polarization behavior is in perfect agreement with the X^0 fine structure described in Sec. 2.2.3.

The anticrossing of the line at $\lambda = 935$ nm is mirrored with respect to the X^0-cavity anticrossing. This is consistent with the expected behavior of the neutral

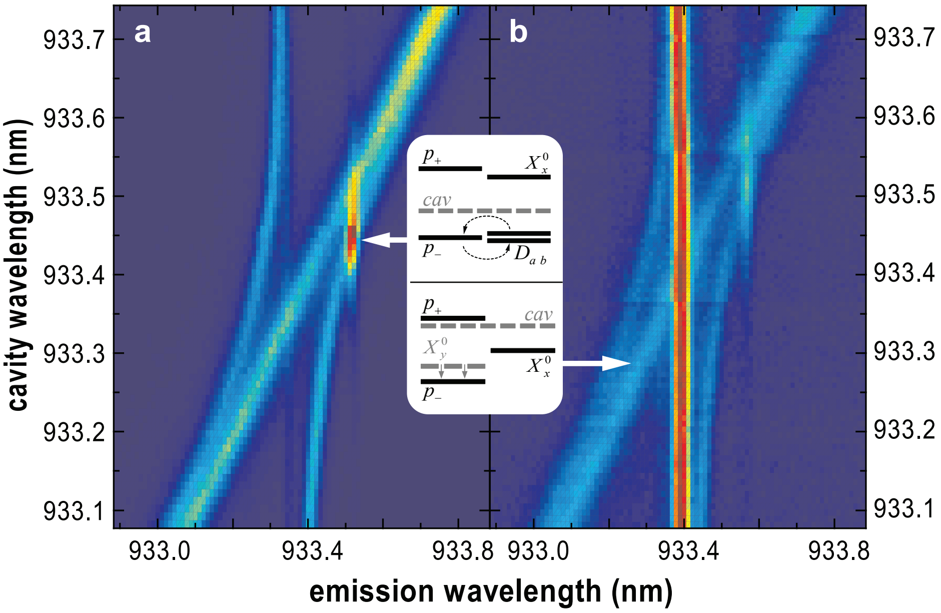

Figure 6.4.: Comparison of X^0 dynamics for different emission polarization. a Zoomed-in version of Fig. 6.2 for the polarizer set in order to maximize the cavity emission. The inset shows level schemes for two different positions of the cavity mode. In the lower inset the cavity is red detuned from the X^0. As the cavity photon energy is reduced, $|p_-\rangle$ moves in resonance with the dark states $|D_{a,b}\rangle$ as indicated in the upper inset. **b** Here the polarizer is set to 55° with respect to the cavity polarization and the signal is plotted in a logarithmic color scale.

biexciton XX^0: since the XX^0 emission arises from biexciton decay to the neutral exciton states $|X^0_{x,y}\rangle$, the vacuum Rabi splitting of the coupled exciton $|X^0_y\rangle$ leads to a splitting of the XX^0 line. Thereby, the upper (lower) polariton state shifts the biexciton decay to lower (higher) emission energy, such that the anticrossing feature of the XX^0 appears horizontally mirrored with respect to that of the X^0. The splitting of the XX^0 amounts to 0.22 nm, identical to the vacuum Rabi splitting of the X^0 itself. Moreover, the intensity of the cavitylike branches decays when moving away from resonance. This is exactly the behavior expected from the XX^0 decaying to the QD-like component of the intermediate $|p_\pm\rangle$. Furthermore, we note that there is no signature of an uncoupled cavity peak as it is present in the anticrossings observed on the X^{1+} and X^0 lines. This supports the hypothesis that the third peak is not an intrinsic feature of the resonantly coupled QD-cavity system itself, but rather a manifestation of off-resonant cavity feeding at times when the QD occupies a state other than the one the cavity is resonantly coupled to.

Since the other pathway of biexciton decay leads through the intermediate uncoupled exciton state $|X^0_x\rangle$, we also expect an x polarized uncoupled biexciton line that does not shift as the cavity mode is tuned. Since the PL shown in Fig. 6.2 is polarized along the y direction, this additional line is hardly visible here. The presence of the uncoupled exciton and biexciton lines for x polarized PL, along with the correlated anticrossings of the y polarized X^0 and XX^0 emission lines make the identification of these transitions unambiguous.

In contrast to these observations, the line at $\lambda = 932.8$ nm exhibits significantly different behavior. In particular, there is no uncoupled exciton for the latter, which is in fact exactly the behavior expected for a charged excitonic state. Given the blueshift of 0.6 nm with respect to the X^0, one can assign this transition to the decay of the positively charged trion state X^{1+}, in which the QD is occupied by a pair of heavy holes together with a single electron. Due to the zero total hole-spin projection in the initial state of the X^{1+} decay, no exchange splitting occurs. The two possible initial electron spin configurations then lead to two degenerate circularly polarized transitions, either of which couple with equal strength to the cavity field. As their decay on resonance mainly occurs via the cavity mode, the emission is copolarized with the cavity mode for both initial states. This is exactly what we experimentally observe for this line.

The fact that the X^0 exhibits a coherent coupling strength g approximately 1.5 times larger than that of the X^{1+} can also be explained by the fine structure of the transitions. Since the transition dipole matrix element of the X^{1+} is circularly polarized, it is reduced by a factor of $\frac{1}{\sqrt{2}}$ with respect to that of a linearly polarized dipole of equal magnitude. Moreover, the difference between the oscillator strengths of the X^0 and the X^{1+} are subject to strong variations from dot to dot. Generally, one expects a slightly smaller oscillator strength for the X^{1+} due to a screening of the electron-hole wavefunction overlap induced by the extra spectator hole. However, the shape of the hole wavefunctions in QDs are usually subject to strong variations, such that the difference in the X^0 and the X^{1+} transition dipole varies strongly from dot to dot.

In conclusion, the observation of the characteristic anticrossings due to the coupling of the cavity mode to the different QD transitions enable the spectroscopic identification of the different lines and their substructures.

6.2. Dark Exciton coupling

In addition to the occurrence of an uncoupled exciton branch, the X^0 shows even richer spectral features, than the charged excitons. When the cavity mode is tuned to the red side of the X^0 line, an additional peak appears in PL. At $\lambda_0 = 933.52$ nm an additional line is activated as the lower polariton branch $|p_-\rangle$ moves in resonance. We can rule out the possibility that this line arises from a different charge configuration of the QD, since it shows a pronounced maximum for a resonance condition with the lower polariton state rather than with the uncoupled cavity mode. This suggests that the mechanism responsible for inducing this luminescence stems from the excitonic rather than from the photonic component of the polariton state $|p_-\rangle$.

The additional PL peak can be related to neutral dark excitons that are activated by a combination of a strong-coupling induced resonance with the $|p_-\rangle$ state and an efficient elastic spin-flip process. As the lower polariton state $|p_-\rangle$ is redshifted due to level repulsion when tuning the cavity mode, it approaches the doublet of dark excitons $|D_\pm\rangle$; the large cavity-exciton coupling ensures that the $|p_-\rangle$ state has a substantial excitonic component when it reaches exact resonance with the dark exciton transition, which occurs for a cavity wavelength of $\lambda_{\text{cav}} = 933.45$ nm[1]. A sketch of this situation is given in the insets of Fig. 6.4. The splitting between bright and dark exciton lines is found to be $\delta_0 = 256$ μeV, in good agreement with values reported elsewhere [58]. Furthermore, we have independently determined δ_0 from the splitting of the double negatively charged exciton X^{2-} and the single negatively charged biexciton $2X^{-1}$ as proposed in [62]. We identify these lines from their spectral location and their power dependences and determine a splitting of 0.17 nm, in close agreement to the measurement presented here.

---

[1] The PL enhancement is not symmetric around the dark exciton resonance. This asymmetry is

In the off-resonant excitation scheme employed in our PL measurement, bright and dark excitons are populated with comparable probabilities, as carriers of random spin are injected into the QD. Optical decay of the population stored in the dark excitons, however, requires a spin-flip to take place prior to the optical recombination event. The strong dependence of the dark-exciton PL on the detuning from the lower polariton branch observed here suggests that an elastic spin-flip process is involved in the optical activation of dark exciton decay. A strong candidate mechanism is the hyperfine interaction between the electron in the QD and the spins of the lattice nuclei. In this process angular momentum can be exchanged with negligible energy transfer [112]. For QDs outside a cavity this process is very inefficient, since the exchange energy δ_0 has to be overcome in order to flip the electron spin. However, as δ_0 is compensated by the strong-coupling induced shift of $|p_-\rangle$, we expect a significant increase of the hyperfine induced electron spin-flip rate.

Typical hyperfine interaction strengths are on the order of $\Omega_\mathrm{N} \sim 0.5$ μeV for QDs with $\simeq 10^5$ atoms [112]. The effective optical recombination time of dark excitons via the resonant intermediate lower polariton state $|p_-\rangle$ is then given by $\gamma_p/\Omega_\mathrm{N}^2 \sim 110$ ns, where γ_p is the linewidth of the lower polariton. This timescale is relatively long compared to the < 100 ps timescale of polariton recombination and the ~ 10 ns timescale of the uncoupled exciton within the photonic bandgap. However, both bright and dark excitons are created with equal probability in the QD, such that the populations of the two are comparable for pump powers well below saturation. Even for different decay times this leads to comparable PL intensities of the cavity induced dark-exciton luminescence and the PL from the polariton states, which is confirmed by multi-Lorentzian fits to our data. If the pump power is increased, the dark excitons can make transitions to other charge configurations like trions or a biexciton by the capture of additional carriers, which results in a depletion of the dark exciton population. This effect can be investigated by studying the X^0 anticrossing feature for different pump powers. Indeed, the dark exciton related PL peak saturates long before the other peaks in the spectrum.

In conclusion, the strong-coupling limit of cavity QED can be used as a powerful spectroscopic tool, providing an unambiguous identification of QD spectral features. The findings presented here could prove useful in more complicated systems such as coupled QDs where the multitude of emission lines render precise identification of PL lines more difficult.

---

probably due to the increasing linewidth of the lower polariton as it crosses the resonance - the decay rate of the $|p_-\rangle$ changes from $(\gamma + \kappa)/2$ on exact resonance to κ far off resonance.

6.3. Influence of Angular Misalignment

Our discussion of the influence of the X^0 and XX^0 fine structure on the strong-coupling PL spectra is based on the assumption that the cavity electric field at the location of the QD is parallel to the one of the excitonic dipoles. In the QD-cavity device used to obtain the data of Fig. 6.1 and Fig. 6.4 this is apparently the case to a good approximation. It has to be mentioned though that reasonable angular alignment between the cavity and the QD polarizations is rather a matter of coincidence. First of all, the L3 fundamental cavity mode exhibits a highly non-trivial electric-field distribution with polarization along the y direction only exactly in the center of the defect. A slight misplacement of the QD therefore results in an off-axis electric field experienced by the QD. Moreover, the angular orientation of the X^0 excitonic dipoles is not necessarily correlated with the lattice vectors of the GaAs host matrix. Their orientation is given by the breaking of the in-plane rotational symmetry of the QD, which is on the one hand given by the asymmetry of the QD confinement potential[2] and on the other hand by an anisotropy of the material piezoeletric field. The interplay between these two effects typically yields a rather random orientation of the X^0 dipoles [113]. Although the L3 cavities were fabricated with the defect line oriented along the [110] crystal direction, this can nevertheless result in an angular misalignment even for a QD located exactly in the defect center.

The following discussion gives an example of such a situation by presenting PL measurements that were obtained using a different QD-cavity device. From an AFM topography of this device we find that here the QD is positioned slightly off the PC defect, such that the electric field experienced by the QD amounts to $\approx 66\%$ of the field maximum in the center of the L3 defect. At this location, the electric field of the cavity mode is not parallel to the y direction, such that an angular misalignment of the exciton axes and the cavity mode polarization is likely. The result of a cavity-polarized PL scan while tuning the cavity mode across resonance with the X^{1+} and the X^0 emission lines can be seen in Fig. 6.5. Obviously, the features observed here are qualitatively comparable to those presented in Fig. 6.2: the anticrossing features of the X^{1+} and X^0 are clearly visible and the XX^0 shows the horizontally flipped anticrossing feature reported above and even undergoes an anticrossing when the cavity mode moves into resonance. The vacuum Rabi splitting observed on these two lines amounts to $2g = 282\ \mu\text{eV}$ for the X^0 and $2g = 198\ \mu\text{eV}$ for the X^{1+}, respectively[3]. We attribute the slight red shift of the QD lines in the top part of the figure to increased temperature fluctuations of the sample chip as the amount of N_2 injected into the system becomes significant.

The difference to the measurements presented before, however, is the presence of an uncoupled exciton branch in the polarization channel of the cavity mode. In contrast to the situation in Sec. 6.1, this uncoupled exciton peak cannot be suppressed by rotating the polarizer. This observation can be related to an angular misalignment between the excitonic dipole and the cavity mode electric field. In

---

[2] The QDs are typically elongated along the [110] direction.

[3] Again, the ratio between the coherent coupling strengths of X^0 and X^{1+} is close to 1.5.

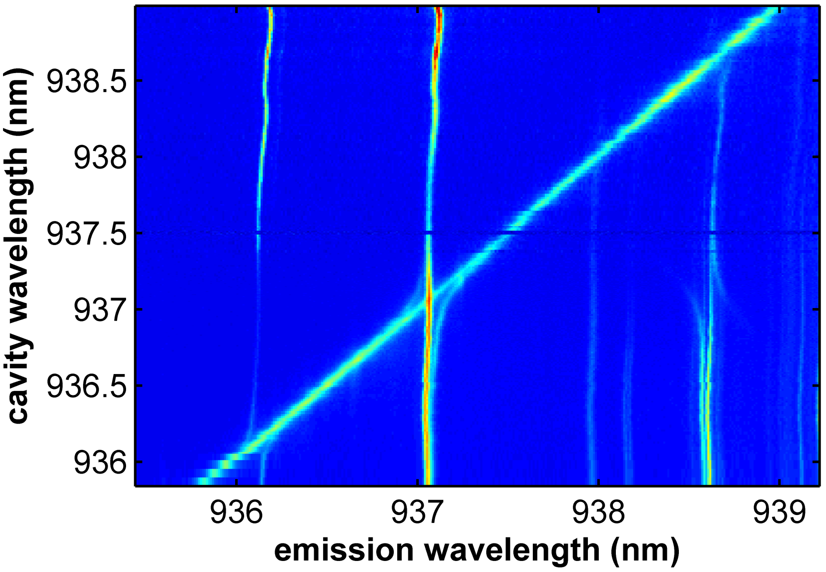

Figure 6.5.: Anticrossings for a device with cavity-X^0 angular misalignment. One can clearly see the presence of an uncoupled exciton branch when the cavity is on resonance with the X^0. Here, this feature cannot be suppressed by changing the polarizer setting in the detection path.

such a situation the QD-cavity coupling is described by the Hamiltonian

$$\begin{aligned} H &= \hbar\omega_c\hat{a}^\dagger\hat{a} + \hbar\omega_{X^0}\left(\hat{\sigma}_{xx}+\hat{\sigma}_{yy}\right) + \frac{\hbar\delta}{2}\left(\hat{\sigma}_{xx}-\hat{\sigma}_{yy}\right) \\ &\quad +\hbar g\sin\theta\left(\hat{\sigma}_{xg}\hat{a}+\hat{\sigma}_{gx}\hat{a}^\dagger\right)+\hbar g\cos\theta\left(\hat{\sigma}_{yg}\hat{a}+\hat{\sigma}_{gy}\hat{a}^\dagger\right), \end{aligned} \tag{6.3}$$

where $\hat{\sigma}_{gx} = |g\rangle\langle X_x^0|$ and $\hat{\sigma}_{gy} = |g\rangle\langle X_y^0|$ are the lowering operators of the x and y polarized exciton branches, respectively, and $|g\rangle$ denotes the ground state of the QD. The angular misalignment is quantified by the angle θ that describes the rotation of the cavity polarization with respect to the y axis.

In the absence of exchange splitting ($\delta = 0$), the eigenstates of this Hamiltonian are

$$|X_\theta^0\rangle = \sin\theta|X_x^0\rangle + \cos\theta|X_y^0\rangle \tag{6.4}$$

$$|X_\perp^0\rangle = \cos\theta|X_x^0\rangle - \sin\theta|X_y^0\rangle \tag{6.5}$$

where $|X_\theta^0\rangle$ corresponds to an excitonic dipole tilted at an angle θ with respect to the y direction and hence coupling to the cavity mode with strength g, whereas the orthogonal exciton $|X_\perp^0\rangle$ does not couple to the cavity at all. For $\delta \neq 0$, however, the two excitons undergo a finite mixing: in the basis $\{|X_\theta^0\rangle, |X_\perp^0\rangle\}$ the Hamiltonian H reads

$$\begin{aligned} H = \hbar\omega_c\hat{a}^\dagger\hat{a} &+ \hbar\omega_{X^0}\Big(|X_\theta^0\rangle\langle X_\theta^0| + |X_\perp^0\rangle\langle X_\perp^0|\Big) \\ &+ \hbar\delta\sin\theta\cos\theta\Big(|X_\theta^0\rangle\langle X_\perp^0| + |X_\perp^0\rangle\langle X_\theta^0|\Big) \\ &+ \hbar g\Big(|X_\theta^0\rangle\langle g|\hat{a} + |g\rangle\langle X_\theta^0|\hat{a}^\dagger\Big), \end{aligned} \tag{6.6}$$

i.e. the cavity-coupled and the orthogonal exciton are mixed by the exchange splitting δ. As a result, both excitons couple to the cavity mode and hence give rise to emission polarized parallel to the cavity mode. Treating the term proportional to δ in Eq. (6.6) in first order perturbation theory, the orthogonal exciton state $|X^0_\perp\rangle$ acquires a contribution from the cavity single-photon state $|g\rangle \otimes |1_c\rangle$:

$$|\widetilde{X^0_\perp, 0_c}\rangle \propto |X^0_\perp, 0_c\rangle + \frac{2\delta}{g} \sin\theta \cos\theta |g, 1_c\rangle. \tag{6.7}$$

The decay of this state via the cavity mode is then given by

$$\gamma_\perp \propto \frac{4\kappa\delta^2}{g^2} \sin^2\theta \cos^2\theta, \tag{6.8}$$

i.e. the fine-structure splitting of the X^0 induces a decay of the orthogonal exciton state that scales with δ^2. The occurrence of the latter in the measurements presented in Fig. 6.5 could therefore also be related to the significant x-y splitting of $\delta \sim 31\ \mu$eV we observe for this device.

7. Cavity Feeding - The Effect of Off-Resonance Cavity Mode Emission

The findings presented in this chapter mainly reproduce those contained in the manuscript [114] submitted to Physical Review Letters.

Besides the demonstration of strong coupling in the QD-PC cavity system studied in this thesis, Sec. 5.1 introduced the entirely unexpected feature of *cavity feeding*. As was obvious from the comparison of PL spectra before and after cavity fabrication (Fig. 5.2), the off-resonant excitation of the QD system in PL leads to significant luminescence from the cavity mode, even when its resonance frequency is far detuned from that of the QD excitons. While this effect had been observed previously in other works based on ensembles of QDs embedded in a microcavity, its occurrence in a system that contains only a single QD was rather surprising and triggered a vivid discussion in the community.

This chapter studies cavity feeding in more detail. Section 7.1 provides the basic phenomenology the main findings of which were originally published in [81]. Section 7.2 then discusses a full theoretical model that accounts for the surprising and partly counter-intuitive features of cavity feeding. Finally, Sec. 7.3 demonstrates an additional mechanism based on phonon scattering that leads to off-resonant coupling of QD excitons to a cavity mode.

7.1. Phenomenology of Cavity Feeding

7.1.1. Off-Resonant PL Spectra

The PL spectrum shown in Fig. 5.2b revealed significant emission from a cavity mode that was blue detuned by $\Delta\lambda_{\mathrm{cx}} = \lambda_{\mathrm{cav}} - \lambda_X = -2.2$ nm from the nearest exciton line (the X^{1+} in this case), a detuning corresponding to ~ 31 cavity linewidths. The same observation was made for all other devices fabricated in the framework of this thesis. Figure 7.1a shows the example of a far red detuned cavity mode with a

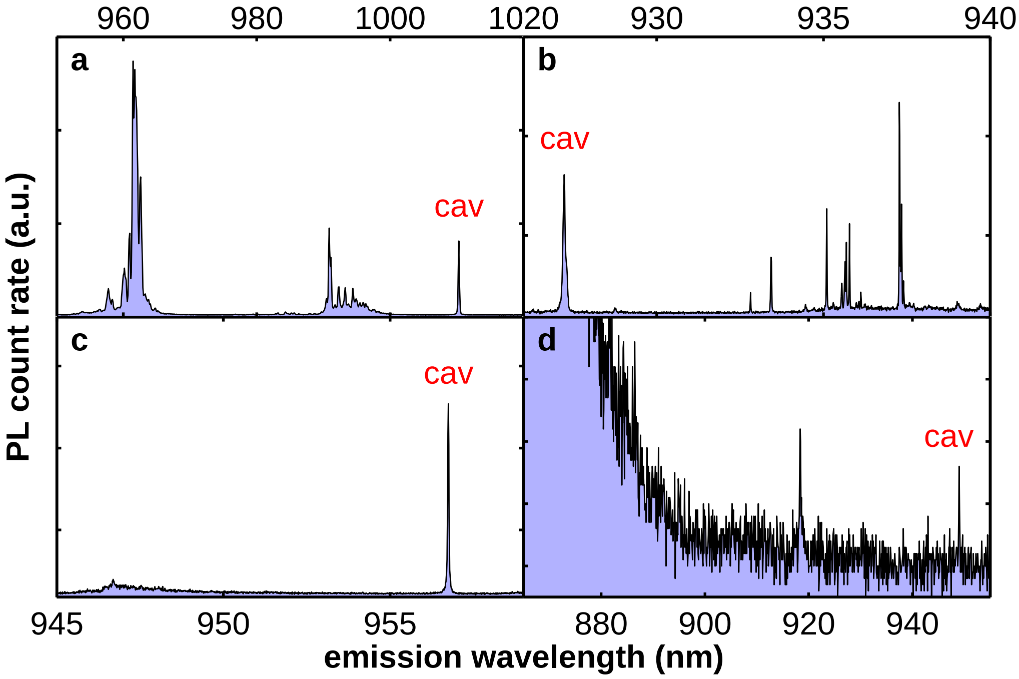

Figure 7.1.: PL spectra showing cavity feeding. **a**, Here, the cavity mode is red detuned by 19 nm from the X^0 of the QD. **b,** Example of cavity feeding for a device with a blue detuning of -6.2 nm from the X^0. **c**, Example for *cavity draining*. For $P_{\mathrm{ex}} = 10$ nW at $\lambda_{\mathrm{ex}} = 780$ nm, the cavity mode shows extremely strong luminescence, while the QD lines are almost fully suppressed. **d**, Emission from a cavity containing no dot, but a wetting layer. This structure was pumped with $P_{\mathrm{ex}} = 10$ μW, but showed only negligible emission from the cavity modes. The peak at $\lambda \approx 918$ nm arises from the second excited cavity mode. The strong emission on the blue side of the spectral window arises from wetting layer emission.

cavity-X^0 detuning of 19 nm. Obviously, significant emission from the cavity mode can be observed at ≈ 1010 nm. The strong emission band around ~ 960 nm stems from the QD p-shell transitions. This observation is particularly surprising, since for this detuning the energy of a single photon in the cavity mode is much smaller than all relevant optical transitions of the QD. Nonetheless, significant emission from the cavity mode can be observed. Similarly, the same behavior was observed for a blue detuned cavity mode, as shown in Fig. 7.1b, where the cavity mode had a detuning of -6.2 nm from the X^0. From experiments conducted on all the other fabricated devices, we found strong cavity mode emission for blue detunings up to ~ 8 nm and red detunings as large as ~ 30 nm.

Even more dramatically, for certain devices even weak off-resonant excitation above the bandgap (e.g. around $\lambda_{\mathrm{ex}} = 780$ nm) led to a complete suppression of the QD lines, while the cavity-mode luminescence became exceedingly strong, as can be seen in Fig. 7.1c. In order to obtain this spectrum, the system was excited at $\lambda_{\mathrm{ex}} = 780$ nm with a power of $P_{\mathrm{ex}} = 10$ nW on the sample surface. A very weak feature arising from QD luminescence around ~ 947 nm is all that is left from the QD spectrum. This *cavity draining* effect is likely to be related to the presence of free carriers, as experiments involving two excitation lasers revealed: a weak above-bandgap laser resulted in strong suppression of the QD lines while driving the system below bandgap, even if the power of the above-bandgap laser was a factor of 100 smaller than that of the excitation laser.

A generic explanation of cavity feeding could be that excitation of the cavity mode does not proceed via the QD, but from a background continuum related to the bulk material or the InAs wetting layer. In order to check this hypothesis, we fabricated a few empty control cavities on parts of the wafer where we checked both by PL and AFM that there were no QDs present. However, these control devices still contain a wetting layer. Surprisingly, in these devices luminescence from the cavity mode could only be detected when pumping the system so strongly that the bandgap-renormalized tail of the wetting layer had an overlap with the cavity mode. This situation can be seen in Fig. 7.1d. For this spectrum, the system was excited at $\lambda_{\mathrm{ex}} = 780$ nm with an excitation power of $P_{\mathrm{ex}} = 10\ \mu$eV, i.e. three orders of magnitude stronger than for the spectrum shown in Fig. 7.1c. However, only weak luminescence could be observed from two peaks at 949 nm and at 918 nm. These two peaks correspond to the first two modes of the L3 cavity. The strong luminescence that can be seen on the short wavelength side of Fig. 7.1d corresponds to emission from the wetting layer.

A similar observation was made on a device where our positioning procedure failed such that the QD was located roughly at an antinode of the cavity field. As in the case of the empty cavity, we found that here the excitation of the QD did not result in significant emission from the fundamental cavity mode.

In summary, these observations suggest that the off-resonance cavity mode emission is not an artifact of the semiconductor environment of the QD, but is indeed related to the presence of the single QD.

7.1.2. Photon Correlation Measurements

To further confirm the interpretation that cavity feeding is mediated only by a single QD, we study the time dynamics of the luminescence by performing intensity cross-correlation measurements between the cavity mode and the X^0 line of the QD using the method presented in Sec. 3.1.5. This measurement was done on a device in which the cavity mode was $\Delta\lambda_{\mathrm{cx}} = 7.48$ nm ($\hbar\Delta\omega_{\mathrm{xc}} = 10.3$ meV) red detuned from the X^0 transition. A PL spectrum of this device can be seen in the inset of Fig. 7.2a. In this situation a photon in the cavity mode carries an energy much smaller than all observed excitonic transitions, such that any direct influence from an excitonic transition on the cavity mode can be neglected. The system was excited with a laser below the bandgap energy at $\lambda_{\mathrm{ex}} = 838$ nm with a power of $P_{\mathrm{ex}} = 0.4\,P_{\mathrm{sat}}$ focused to a diffraction limited spot size[1]. Following the techniques described in Sec. 3.2.3, the two emission lines corresponding to X^0 decay and the uncoupled cavity mode emission were separated by the spectrometer grating and then directed onto two separate APD detectors, as schematically indicated in Fig. 7.2a. Figure 7.2b shows

---

[1] The saturation power P_{sat} here is defined as pump power at which the X^0 emission intensity assumes its maximum value. In this device and for this detuning this is the case for $P_{\mathrm{sat}} \approx$ 700 nW.

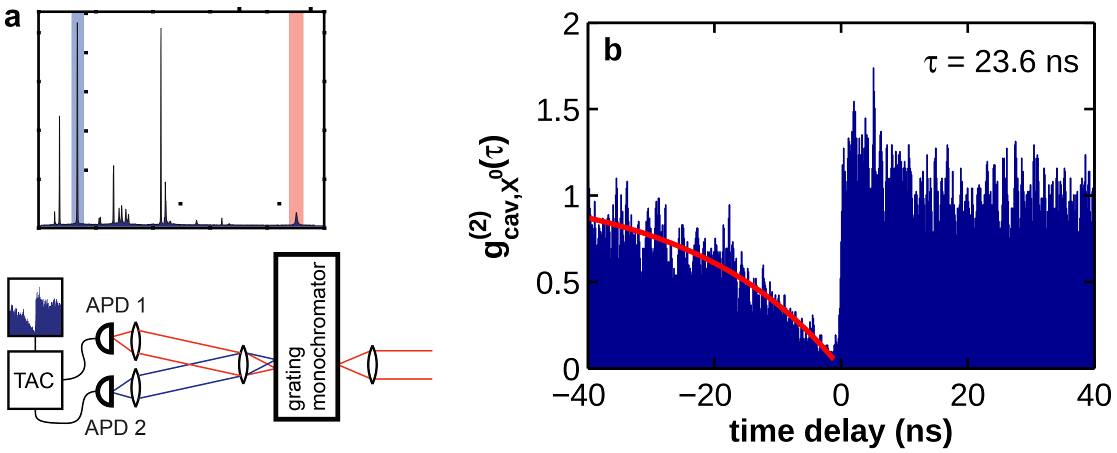

Figure 7.2.: QD-cavity cross-correlation measurement. **a**, Schematic of the setup: the spectrometer grating separates the cavity mode (blue window in the inset) from the X^0 (red window) emission. The subsequent imaging system directs the two spectral windows onto two separate APDs. **b**, Cross-correlation histogram between cavity and X^0 emission. Positive time delay corresponds to X^0 detection upon observation of a cavity photon.

the measured cross-correlation function

$$g^{(2)}_{\mathrm{cav},X^0}(\tau) = \frac{\left\langle : \hat{I}_{\mathrm{cav}}(t)\hat{I}_{X^0}(t+\tau) : \right\rangle}{\left\langle \hat{I}_{\mathrm{cav}} \right\rangle \left\langle \hat{I}_{X^0} \right\rangle} \tag{7.1}$$

between the cavity and the X^0 luminescence, i.e. a histogram of coincidence photon counts as a function of their time separation. Experimentally, the TAC timer here is started upon detection of a cavity photon and stopped upon detection of a photon arising from X^0 emission, such that $\tau > 0$ refers to X^0 detection after detection of a cavity photon. For $\tau = 0$ there is a strong suppression of coincidence counts, which means that emission from the cavity mode and from the X^0 never occur simultaneously: the excitation provided by the off-resonant PL laser is either channeled into the cavity mode or into the QD.

In combination with the absence of cavity-mode emission in devices that do not contain QDs, the observation of close to perfect anti-correlation between photons emitted from the cavity mode and the X^0 transition proves unequivocally that off-resonance cavity mode emission is mediated already by a single QD. It is therefore natural to assume that cavity feeding relates to a fundamental feature of QDs that goes beyond the usual picture, in which QDs are modeled as N-level atoms with a series of independent sharp excitonic transitions manifested as discrete lines in the PL spectra. Moreover, it has to be mentioned that analogous results were reported in [100], where the off-resonant emission of photonic crystal cavities was investigated in the presence of an ensemble of QDs.

Another pronounced feature of the histogram shown in Fig. 7.2 is the distinctive asymmetry of the timescales on either side of $\tau = 0$. For $\tau < 0$ we find an exponential recovery of the cavity PL upon X^0 detection with a time constant of $\tau_- = 23.6$ ns, which is on the same order of magnitude as the lifetime of the X^0 for this detuning value. From an exponential fit to a luminescence decay curve of the X^0 for this detuning, we find $\tau_{X^0} = 14.6 \pm 6.6$ ns. The large error bar can be explained by the fact that this long decay time is larger than the accessible time window of the correlation setup[2], such that finding the correct offset for $\tau \to \infty$ is difficult difficult. Nonetheless, a decay time in the range of ~ 20 ns is consistent with the depleted radiation field density of states due to the presence of the photonic bandgap.

For $\tau > 0$, the cross-correlation curve exhibits a sharp rising edge that with the maximum clearly above the average level of $g^{(2)}(\infty) = 1$. This means that the X^0 luminescence very quickly recovers upon detection of a cavity photon and then even occurs with an even higher probability than on average.

In order to gain further insight into the nature of cavity feeding, we measured the intensity auto-correlation function of the cavity mode luminescence

$$g^{(2)}_{\text{cav}}(\tau) = \frac{\left\langle : \hat{I}_{\text{cav}}(t)\hat{I}_{\text{cav}}(t+\tau) : \right\rangle}{\left\langle \hat{I}_{\text{cav}} \right\rangle^2} \tag{7.2}$$

using the HBT scheme described in Sec. 3.1.4. Figure 7.3 shows the result for the same device that was used above. Here, the cavity mode was tuned to an even larger detuning of $\Delta\lambda_{\text{cx}} = 11.2$ nm ($\hbar\Delta\omega_{\text{xc}} = 15.3$ meV) with respect to the X^0 line[3] and the system was excited with $P_{\text{ex}} \approx P_{\text{sat}}$ at $\lambda_{\text{ex}} = 838$ nm. Obviously, the emission of the off-resonant cavity mode exhibits weak super-Poissonian statistics with a slight bunching feature of $g^{(2)}_{\text{cav}}(0) = 1.8$ at $\tau = 0$. This result is rather surprising, given that the cavity mode is excited by the QD: despite being fed by a single emitter, the cavity mode itself does not show antibunching.

At first sight, the puzzling interplay of photon correlations, in combination with the occurrence of strong cavity emission over a wide detuning range appears as a complete mystery and led to an ongoing discussion and the development of several controversial models aimed at the explanation of cavity feeding. The following section describes the experimental and theoretical work that results in a full understanding of cavity feeding based on a microscopic model.

7.2. A Model for Cavity Feeding

7.2.1. General Considerations

An important question that has to be addressed in order to gain a theoretical understanding of cavity feeding is, whether off-resonant cavity feeding is an intrinsic feature of any two-level system that couples to external reservoirs (like the semiconductor solid-state environment in this case), whether it is due to the peculiarities

---

[2] The maximum width of time window is given by the inverse repetition rate of the laser $1/f_0 \approx 13$ ns.

[3] The cross-correlation measurement presented in Fig. 7.2 could not be conducted at such large detuning, due to the limited operation range of the correlation setup. Hence the different $\Delta\lambda_{\text{cx}}$ in the two cases.

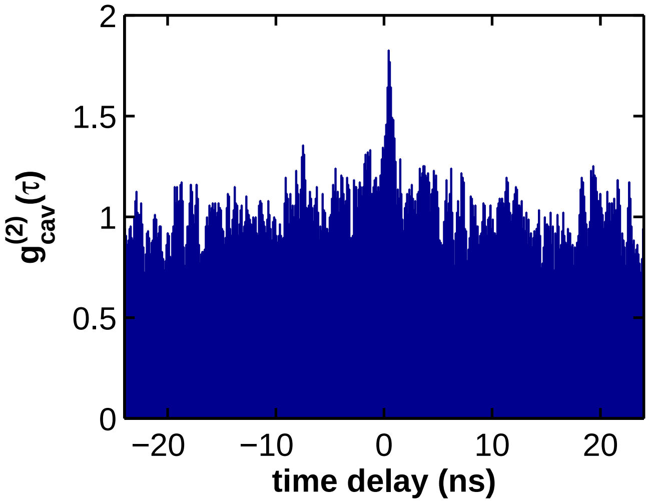

Figure 7.3.: Auto-correlation measurement of cavity PL. Measured auto-correlation curve $g^{(2)}_{\mathrm{cav}}(\tau)$ of the off-resonant cavity-mode emission at a detuning of $\Delta\lambda_{\mathrm{cx}} = 11.2$ nm. Here the pump power was close to the saturation power of the QD.

of photonic crystal cavities, or whether it arises from the apparent deviation of the QD level structure from the simple two-level atom. A generic example for an effect of the first type is coupling of QD excitons to phonons: the excitation energy of a two-level system (like a QD exciton) can be transfered directly to an off-resonant cavity mode with the energy difference provided by or promoted to a phonon in the surrounding semiconductor material. And for energy differences between the QD exciton and the cavity mode of up to ~ 3 meV we find that is indeed the case. A detailed study of this mechanism is given in Sec. 7.3. However, this cannot explain cavity feeding for detunings as large as ~ 25 meV, thus indicating the presence of different mechanisms.

An alternative effect related to the interaction with the environment that was advertised to explain cavity feeding is pure exciton dephasing [115, 116]. In their work, Hughes and Yao [117] related cavity feeding to the spectral response of the dielectric environment in a photonic crystal nanocavity, while still modeling the QD as a two-level atom.

While all these different models were aimed at the explanation of off-resonant cavity PL, the peculiar quantum correlations observed experimentally remained unexplained. In particular, the distinct asymmetry observed in the cross-correlation function between the cavity mode and the exciton emission is not consistent with such a model: in the case of direct off-resonant coupling between a single QD transition and the cavity field one would expect the cross-correlation to exhibit an anti-correlation feature that is symmetric in the time delay due to the mixed character of the two entities.

In contrast, the model presented in this work is based on the assumption that in addition to the discrete excitonic transitions discussed in Sec. 2.2.3 that give rise to the prominent PL emission lines, the QD supports a multitude of additional

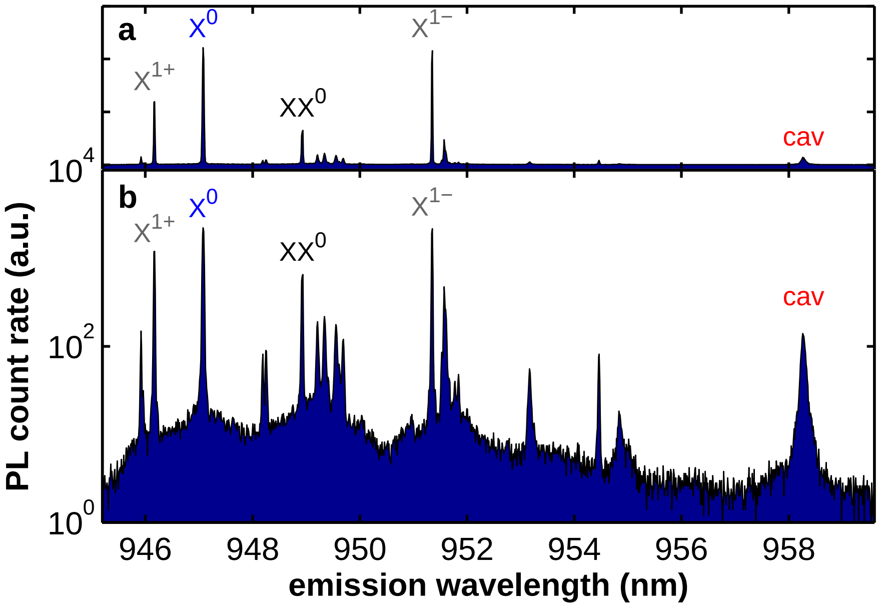

Figure 7.4.: Device PL showing significant QD background emission. a, The device is excited at $\lambda_{\text{ex}} = 838$ nm with $P_{\text{ex}} = 54$ nW, corresponding to approximately half the saturation power. The emission from the neutral exciton (X^0), the biexciton (XX^0), and the positively (X^{1+}) and negatively (X^{1-}) charged trions, are indicated along with the cavity mode. **b**, The same PL spectrum as in **a** on logarithmic scale. The formation of a weak background underlying the QD lines can clearly be seen.

much weaker optical transitions that can give rise to excitation of the cavity mode over a broad spectral range. In this picture, cavity feeding arises from the non-trivial level structure of the QD going beyond that of a standard two-level system. In fact, straightforward PL measurements reveal the presence of a broad emission background related to the QD. Figure 7.4a shows a PL spectrum obtained from the QD-cavity device presented above, in which the cavity has been tuned approximately 15.3 meV to the red of the X^0 using N_2 tuning as introduced in Sec. 4.2.2. Like in the spectra shown previously, the emission of the neutral exciton (X^0), the biexciton (XX^0), and the positively (X^{1+}) and negatively (X^{1-}) charged trions can clearly be seen along with the emission from the uncoupled cavity mode at $\lambda_{\text{cav}} = 958.26$ nm. The same PL spectrum is shown in Fig. 7.4b on a logarithmic scale. Here, the formation of a weak emission background underlying the discrete QD lines can clearly be seen, and the emission intensity of this background is approximately two orders of magnitude weaker than that of the discrete QD emission lines. In this picture, cavity feeding is mediated by this background, since the portion of the background resonant with the cavity mode experiences an enhancement of its optical recombination rate due to the large electromagnetic field density of states on resonance with the cavity mode (*Purcell effect*, see Sec. 2.1.2). The background emission across the cavity mode spectral profile is thus enhanced, thereby leading to the off-resonant cavity mode emission.

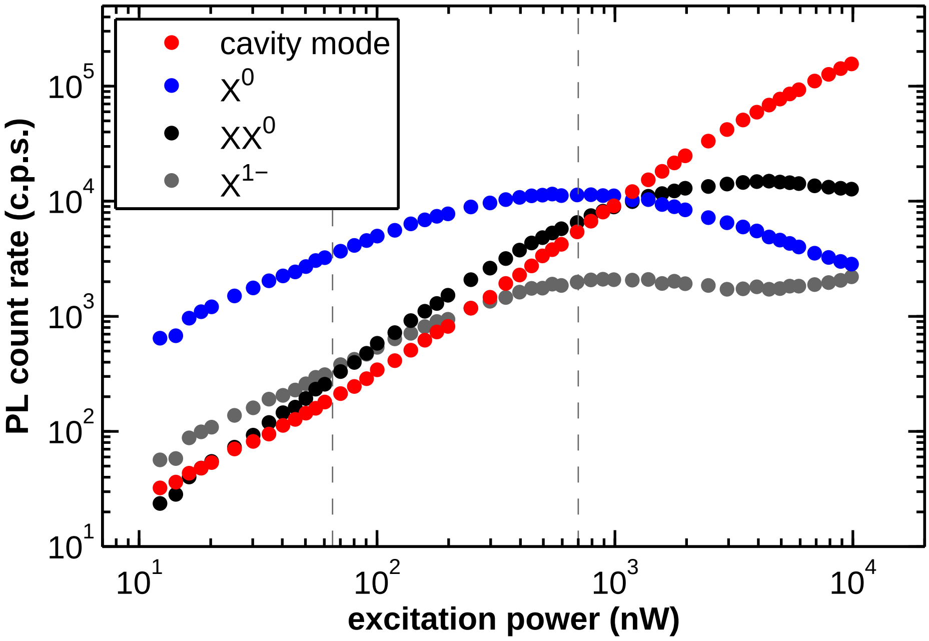

Figure 7.5.: Pump power dependence of photoluminescence of the cavity mode, X^0, XX^0, and X^{1-} emission. The data were obtained by integrating the PL spectra for different excitation powers in ~ 0.3 nm wide windows around the spectral locations indicated in Fig. 7.4.

Following these arguments, unraveling the physical mechanisms behind cavity feeding requires the identification of the QD states that give rise to the QD emission background. In order to obtain a qualitative understanding of the latter, pump-power dependent PL measurements as introduced in Sec. 3.4 were carried out. Figure 7.5 shows the result of such a measurement in a log-log plot, displaying the integrated line intensities of the X^0, XX^0, and X^{1-} lines of the QD together with the off-resonant emission from the cavity mode as a function of pump power. As expected, the X^0 and X^{1-} lines follow an approximately linear pump power dependence below saturation. Moreover, the XX^0 line shows a power-law dependence with an exponent of ~ 1.5, thus reflecting the excited-state nature of the XX^0. In contrast, the pump-power dependence of the cavity mode fed by the broad QD background in Fig. 7.4 is more complex. For extremely low pump powers, it follows a linear power-dependence, similar to the X^0 and the X^{1-} lines. When increasing the pump power, however, the power-dependence becomes superlinear: in between the two vertical dashed lines in Fig. 7.5 the cavity reflects the power dependence of the XX^0 line. Furthermore, the cavity intensity increases far above the saturation levels of both the X^0 and the XX^0. In this regime, we find that the cavity power dependence follows that of the QD p-shell emission, as can be seen in Fig. 7.6. Figure 7.6a shows a low-resolution PL spectrum showing the QD s-, p-, and d-shell together with the cavity mode. Fig 7.6b shows the integrated intensities of the entire QD shells, together with the XX^0 emission and the cavity mode as a function of pump

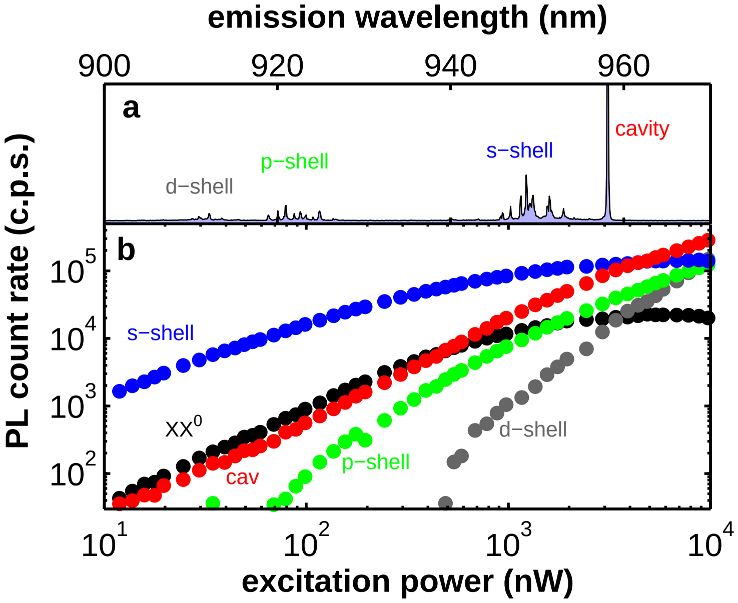

Figure 7.6.: Pump power dependence of higher QD shells. **a**, Low-resolution PL spectrum showing the cavity mode together with the QD s-, p-, and d-shell emission. **b**, Pump power dependence of the integrated shell intensities. For low pump powers the cavity mode follows the s-shell emission (in particular the XX^0 line). For higher pump powers the higher shells “take over”.

power. For low pump powers, the cavity mode follows the s-shell and in particular the XX^0 emission. When the s-shell emission saturates for higher pump powers, the p-shell “takes over” and the cavity mode exhibits a pump power dependence that is essentially that of the p-shell. In combination, these observations suggest that QD background emission leading to cavity feeding originates from higher excitation manifolds of the QD.

In order to understand the mesoscopic origin of the QD background emission responsible for cavity feeding, one needs to consider the full excitation spectrum of electron and hole motional states in the QD. As has been shown in Sec. 2.2.3, the narrow QD lines corresponding to the X^0, XX^0, and $X^{1\pm}$ decay originate from excitonic configurations in which the carriers all occupy their lowest energy single particle states within the QD confinement potential. However, in addition to these states, there is a large variety of higher excited excitonic configurations. For example, an excited state of the neutral exciton X^0 can be created by lifting the electron to a p-shell state. Taking into account all possible single-particle states of both the electron and the hole, one therefore finds a series of excited X^0 states. Furthermore, the same argument holds for any higher *excitation manifold*, in which multiple electron-hole pairs are confined in the QD. As a result, this leads to a QD excitation spectrum consisting of a series of n-manifolds that are separated approximately by the s-shell transition energy, where n refers to the number of electron-hole pairs stored in the QD. This situation is depicted in Fig. 7.7, displaying the result of a calculation (details see below) of the QD level scheme. In this picture, the

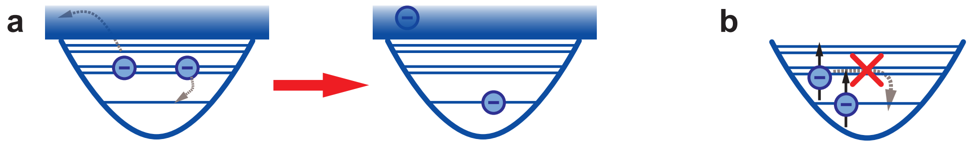

Figure 7.8.: Coupling mechanisms between multi-exciton states. **a**, Example for an Auger-type process in which a state containing two electrons in a p-orbital is mixed with the continuum. **b**, Inhibition of QD intraband-relaxation due to spin selection rules.

formation of different n-manifolds corresponding to different QD occupancies, each consisting of a series of excited states, can clearly be seen. In this setting, the X^0 line corresponds to a transition from the lowest energy state in the $n = 1$ manifold to the ground state ($n = 0$) of the QD ($1 \rightarrow 0$ transition), whereas the decay of the XX^0 relates to a transition between the lowest energy states of the $n = 2$ and the $n = 1$ manifolds ($2 \rightarrow 1$ transition).

Finally, it has been demonstrated that higher energy orbital states in an excitation manifold $n \geq 2$ are subject to strong hybridization with the wetting-layer and bulk continua [118]. As an example consider a state in which the p-shell level of the QD is occupied with two electrons, as indicated in Fig. 7.8a. Such a configuration has the same energy as a state, in which one electron relaxes to an s-shell state, while the other electron makes a transition to the continuum of the wetting-layer. The electronic Coulomb interaction mixes these two configurations, thus forming a hybridized eigenstate that has partly localized character and is partly extended to the continuum of the wetting-layer. The occurrence of such Auger-type processes ensures an effective coupling of certain states in manifolds with $n \geq 2$ to the continuum, which in turn has the effect of leading to an even increased number of accessible states in the QD excitation spectrum.

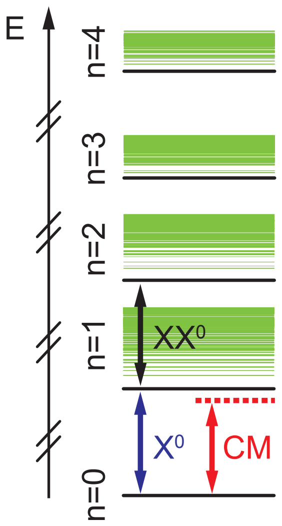

Figure 7.7.: Calculated level spectrum of a QD. Each manifold n contains a series of excited states.

Given the large variety of initial and final states, transitions between these excitation manifolds span a large spectral range, thus resulting in a broad spectral band of QD optical transitions that can potentially take part in feeding the cavity mode. Notably, however, this is only true for transitions starting in the biexciton ($n = 2$) manifold: transitions from $n = 1$ states to the ground state of the QD only contain a few sparse spectral lines, comprising the X^0, the p-shell excitons, and so forth. For initial states in $n \geq 2$ manifolds, however, the $n \rightarrow n - 1$ transitions merge to a quasi-continuum and give rise to the broad QD emission background responsible for cavity feeding. Typically, however, one would expect an excited state in any excitation manifold to undergo fast non-radiative relaxation to the ground state of the corresponding manifold due to LO-phonon mediated intraband relaxation as discussed in Sec. 3.1.1. The occurrence of an appreciable branching of excited state decay into optical transitions is therefore rather surprising. However, it is likely that spin selection rules play a key role in enhancing the stability of excited manifold states with respect to LO-phonon relaxation. As an example, consider the case depicted in Fig. 7.8b, in which the QD is populated by two electrons, one of which is excited to the p-shell and forms a spin triplet with the other electron residing in the s-shell. In such a situation, direct relaxation of the p-shell electron to the s-shell is forbidden due to the Pauli exclusion principle. Since typical spin-flip times in QDs are expected to be significantly longer than the timescales of optical transitions, this effect potentially leads to an increased occupancy of excited multi-exciton states which then contribute to optical emission into the cavity mode.

Following the arguments given above, the presented model requires that the dot is excited to at least an $n = 2$ state in order to make a quasi-continuum transition that can feed the cavity mode. In this situation, one expects the cavity mode luminescence to exhibit a super-linear pump-power dependence that reflects excitation of the QD to an $n = 2$ manifold. In fact, this is exactly what is observed for pump powers above ∼100 nW in Fig. 7.5.

As has been mentioned in Sec. 7.1.1, devices that contain no QD but a wetting layer did not show any significant cavity-mode emission in PL. However, similar arguments like those given above for cavity feeding mediated by a QD also apply for the case of a quantum well: the presence of subbands in the quantum well dispersion actually ensures the existence of a broad-band continuum of optical transitions. Nonetheless, such transitions between excited quantum well states cannot feed a cavity mode, since it is not possible to conserve energy and in-plane momentum simultaneously in such a transition. In the case of the QD, however, in-plane momentum conservation is relaxed, allowing for cavity feeding from transitions between the QD excited states. The presence of the QD is hence crucial and is in this sense similar to the role played by the atomic nucleus in Bremsstrahlung. From these arguments it is also clear that the QD transitions giving rise to cavity feeding occur between states that have a contribution of a state with a wavefunction localized in the QD[4].

While the discussion above is dealing with the case of a neutral QD (i.e. equal numbers of electrons and holes), similar excitation spectra also exist in the case of a charged QD, where a net charging exists due to the presence of extra electrons or holes. In contrast to the neutral QD level spectrum, here also the $n = 0^{\pm}$ manifolds consists of multiple states owing to the excited confined motional states of the extra charge. For charged QDs, cavity feeding can therefore also occur in $1^{\pm} \rightarrow 0^{\pm}$ transitions. Hence, one expects a cavity PL power dependence comparable to that of the X^{1-} or the X^{1+} in a regime where charged QD feeding dominates. This is indeed what we observe for pump powers below ∼100 nW in Fig. 7.5, where

---

[4] Notice that the excited states of a QD coupled to the wetting layer continuum can be divided into three categories: (a) states that are purely localized within the QD, (b) localized states that have a contribution of delocalized wetting-layer states, and (c) extended states with delocalized wavefunctions in the wetting layer. In our arguments, only states of the type (a)&(b) can contribute to cavity feeding.

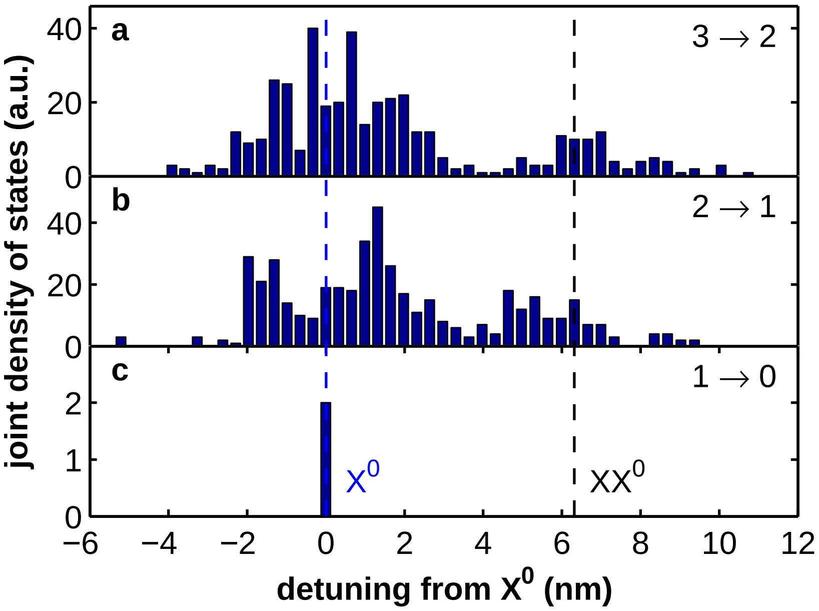

Figure 7.9.: Joint density of states for different manifold transitions. Starting from the calculated level spectrum shown in Fig. 7.7 the joint radiative density of states for transitions between different manifolds has been calculated. Obviously, while the lowest lying 1 → 0 QD transitions only give rise to the X^0 in the spectral window shown (**c**), higher excited manifold give rise to broadband emission, as is obvious from **a** and **b**.

the excitation level of the QD is so low that feeding from excited biexciton states is negligible.

7.2.2. Theoretical Modeling

In order to gain further insight into how the complex QD spectrum (Fig. 7.7) leads to cavity feeding, numerical calculations were performed to determine the extended QD level scheme and to study the classical time dynamics of optical transitions. All the theoretical work along these lines was carried out by Guillaume Tarel and Vincenzo Savona at Ecole Polytechnique Fédérale in Lausanne (Switzerland). By calculating the single particle levels including spin of a truncated parabolic confinement potential, one obtains a realistic model of the QD coupled to the wetting-layer continuum. By including the mutual Coulomb interaction between up to four electron-hole pairs one can then calculate the multi-exciton eigenstates of the QD-wetting layer system. The result of this simulation was shown above in Fig. 7.7. Moreover, from the calculated level spectrum one obtains the joint density of states for optical transitions between different manifolds, as can be seen in Fig. 7.9. This magnitude quantifies the number of available transition in a certain energy window, each weighted by its corresponding oscillator strength. From this graph it is obvious that the 2 → 1 and 3 → 2 transitions occur over a wide spectral range (Fig. 7.9a&b), while decay of the $n = 1$ states only leads to discrete emission lines corresponding to the

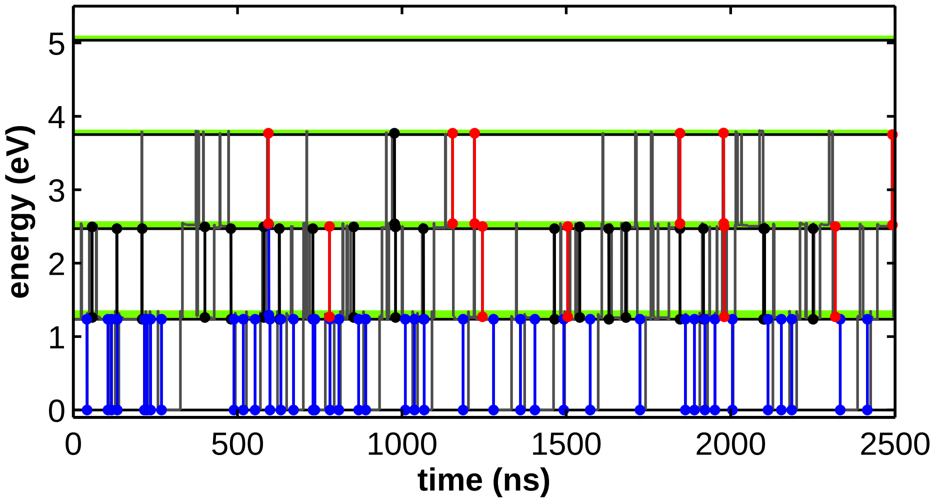

Figure 7.10.: Monte-Carlo random-walk simulation of the QD-cavity system. The gray lines depict random excitation and photon-emission events. Transitions resonant with the cavity mode are highlighted in red color. The blue (black) lines correspond to emission of an X^0 (XX^0) photon. As expected, all cavity feeding events originate from 2 → 1 and 3 → 2 transitions.

X^0 (Fig. 7.9c), the p-shell and higher-lying transitions. Since Fig. 7.9 only shows a narrow spectral window of 18 nm width, only the X^0 transition can be seen in Fig. 7.9c. Evidently, the calculated joint density of states is in good agreement with the qualitative arguments for cavity feeding given above.

Having calculated the level spectrum shown in Fig. 7.7, it is possible to simulate the classical dynamics of the QD-cavity system by numerically performing a Monte-Carlo random walk for a given excitation rate. A typical result of such a simulation is shown in Fig. 7.10, which displays the system energy as a function of time. The random quantum jumps corresponding to excitation and photo-emission events are indicated by vertical lines. Those events that correspond to an optical transition in the frequency window of the cavity mode are indicated by red lines, whereas the X^0 and XX^0 events are shown in blue and black, respectively. Obviously, one can see that all the cavity photons are emitted in 2 → 1 and 3 → 2 transitions; in contrast, no cavity photons are emitted in 1 → 0 transitions due to the energy mismatch of those transitions with the cavity mode. This observation is in perfect agreement with the qualitative arguments given above.

Moreover, from the Monte-Carlo simulations presented here, it is possible to study the spin configurations of the states giving rise to emission of a cavity photon in order to investigate the role that spin selection rules play in ensuring a finite occupancy of excited QD multiexciton states. From our simulations, we indeed find that there exists a positive correlation between states feeding the cavity mode and states in which either the electrons or the holes occupy a spin triplet configuration, in support of our hypothesis. However, a quantitative agreement with a symmetry-based model of carrier spin configurations could not be established. This is most probably due to the rich spin-relaxation dynamics of different multi-excitonic compounds.

We remark here that the simulations presented are restricted to the case of a neutral QD populated with an equal number of electrons and holes. However, we argue that the inclusion of charged exciton states would not affect the general validity of the models or of our findings.

7.2.3. Photon Correlations

As discussed above, the unexpected occurrence of off-resonant cavity PL is accompanied by a subtle interplay between different photon correlation features. This section discusses how these features arise naturally from our model. Moreover, numerically calculated correlation functions are presented that show good qualitative agreement with our experimental findings [81] and those of others [100].

Cavity-X^0 Cross-Correlation In Sec. 7.1.2, the measured normalized cross-correlation function between the cavity mode and the X^0 transition has been presented. There we observed that photons emitted from the cavity and from the trion under consideration are anti-correlated at the level of single quanta. However, in the case of direct channeling of the X^0 energy into the cavity mode, one would expect a symmetric cross-correlation feature[5]. The distinctive asymmetry of the cross-correlation feature shown in Fig. 7.2 together with the occurrence of bunching for $\tau > 0$ must therefore originate from the structure of the background emission feeding the cavity mode.

In fact, these findings are fully consistent with the model presented above. First of all, anti-correlation follows naturally from the fact that cavity feeding proceeds from a different excitation manifold than the X^0 luminescence. Furthermore, the bunching feature for $\tau > 0$ arises since cavity feeding proceeds from higher excited states of the neutral QD. Bunching for $\tau > 0$ is due to the fact that detection of a cavity photon leaves the QD in a state that leads to X^0 emission with higher probability than on average. Indeed, this is exactly what is expected from the model proposed here: in the case of feeding from $2 \rightarrow 1$ transitions of the neutral QD, the emission of a cavity photon projects the QD in an excited state of the $n = 1$ manifold, such that the QD has an enhanced probability to be found in the X^0, which can occur upon an additional non-radiative intraband transition. When increasing the pump power, the average population of the QD is higher, such that the information gained by the detection of a cavity photon is reduced. This is manifested in a reduction of the bunching peak for higher pump powers, which is exactly what we observe experimentally. Figure 7.13a–h displays measured X^0-cavity cross-correlation curves over a wide range of pump powers. While for the lowest pump powers in Fig. 7.13a&b the bunching is clearly visible, it disappears at higher pump power. Moreover, we find that the timescale of cavity PL-recovery upon X^0 detection (i.e. the rising slope for $\tau < 0$) shortens considerably when increasing the pump power. This can be explained by the fact that the rising slope for $\tau < 0$ is related to the excitation rate of the system.

---

[5] A corresponding anti-correlation has been observed between differently charged exciton transitions in [119].

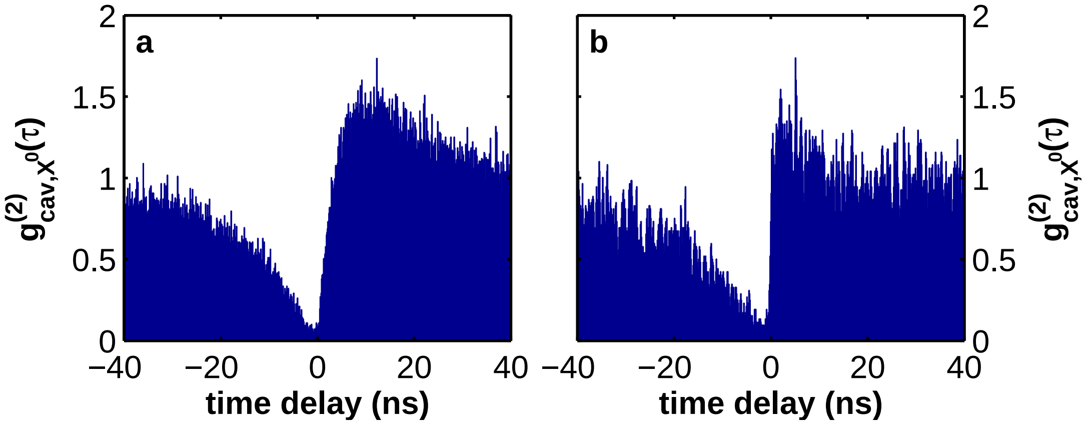

Figure 7.11.: Theoretical and experimental cavity-X^0 cross-correlation curves. **a**, Theoretical simulation of the X^0-cavity cross-correlation function $g^{(2)}_{\mathrm{cav},X^0}(\tau)$ extracted from a simulated Monte-Carlo random walk for an excitation rate corresponding to the one used experimentally. **b**, Measured cross-correlation function, reproduced from Fig. 7.2. Positive time differences refer to X^0 emission upon detection of a cavity photon. For the measurement, the cavity mode was 10.3 meV red detuned from the X^0 transition.

Furthermore, the cross-correlation function from Eq. (7.1) can be extracted from the simulated Monte-Carlo random walks. Figure 7.11a shows the result of such a simulation, where the cavity mode was assumed to be 7 meV red detuned from the X^0 line. The qualitative agreement with the experimental curve is remarkable. In the simulation, we chose a detuning different to the 10 meV used in the experiment, since the joint radiative density of states captured by the simulation strongly decreases for detunings much larger than 7 meV. Moreover, a discrepancy in the exact detuning is not expected to lead to dramatic qualitative changes, in particular since the features of Fig. 7.11 seem to be very robust with respect to detuning: the same qualitative behavior was observed both experimentally and in theory for different values and even for the opposite sign of the QD-cavity detuning. Furthermore the observed behavior was confirmed by experiments with different devices.

The discrepancy in magnitude of the bunching peak as well as the difference in time-constants between the numerical and the experimental results is mainly due to the fact that the spin-flip and the intraband relaxation rates are not well-known and give rise to a certain ambiguity in the simulations. Moreover, the shape of the cross-correlation curve in Fig. 7.11a sensitively depends on the excitation rate of the system. In fact, the relation between this rate assumed in the simulation and the experimental pump laser power is rather difficult to establish.

Cavity Auto-Correlation As shown previously in Sec. 7.1.2, the photon stream emitted by the off-resonant cavity mode did not show the quantum statistics of a single emitter, despite being fed by a single QD. Actually, the auto-correlation function of the cavity mode even exhibited weak bunching at $\tau = 0$, as can be seen in Fig. 7.3. In fact, the occurrence of bunching provides additional proof for cavity

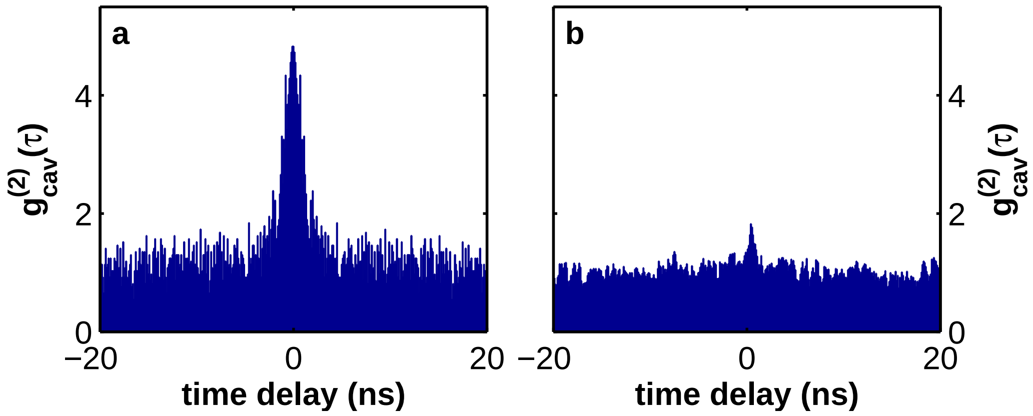

Figure 7.12.: Experimental and theoretical cavity auto-correlation curves. **a**, Auto-correlation function $g^{(2)}_{\text{cav}}(\tau)$ of the cavity mode extracted from the simulation. Feeding from higher excitation manifolds results in the occurrence of bunching for an excitation rate below saturation. **b**, Experimentally measured auto-correlation (reproduced from Fig. 7.3) showing bunching, although less pronounced than in the simulation.

feeding from excited QD states: when the system is driven well below saturation, the likelihood of finding the QD in a $n \geq 2$ manifold state is very small. Detection of a cavity photon, however, projects the QD in a higher excited state, implying in turn that the conditional probability of recurred QD excitation to an $n \geq 2$ state is enhanced and that a second photon-emission event is more likely to occur than on average. In fact, a related bunching feature has been observed before in the auto-correlation function $g^{(2)}_{XX^0}(\tau)$ of the QD biexciton emission, where the occurrence of bunching reflects the excited-state nature of the XX^0 [119].

It has to be mentioned at this point that the cavity auto-correlation trace published previously [81] was obtained at a pump power above saturation. In this case, we expect the bunching feature to be reduced, since the average population of the QD is high. Accordingly, detection of a single cavity photon does not reveal much additional information on the excitation level of the system, such that the probability of detecting a second photon is independent of the first detection event.

This behavior is once again well reproduced in our simulations: Fig. 7.12a shows a cavity auto-correlation trace extracted from Monte-Carlo simulations for the cavity red detuned by 7 meV from the X^0 and for a pump power below saturation. As expected from the qualitative arguments given above, this curve shows strong bunching with $g^{(2)}_{\text{cav}}(0) = 4.8$. Experimentally, however, we only measure $g^{(2)}_{\text{cav}}(0) = 1.8$, as can be seen from Fig. 7.12b. The main reason for this discrepancy lies in the absence of QD charged states in the simulations: the only mechanism that can lead to cavity feeding in our theoretical model is feeding from neutral $n \geq 2$ states, which theoretically implies a bunching feature of arbitrary magnitude when decreasing the pump power. Experimentally, on the other hand, feeding can also occur from charged $1^{\pm} \rightarrow 0^{\pm}$ transitions, for which we do not expect any bunching. In the regime of weak pump power well below saturation, feeding from excited trion states

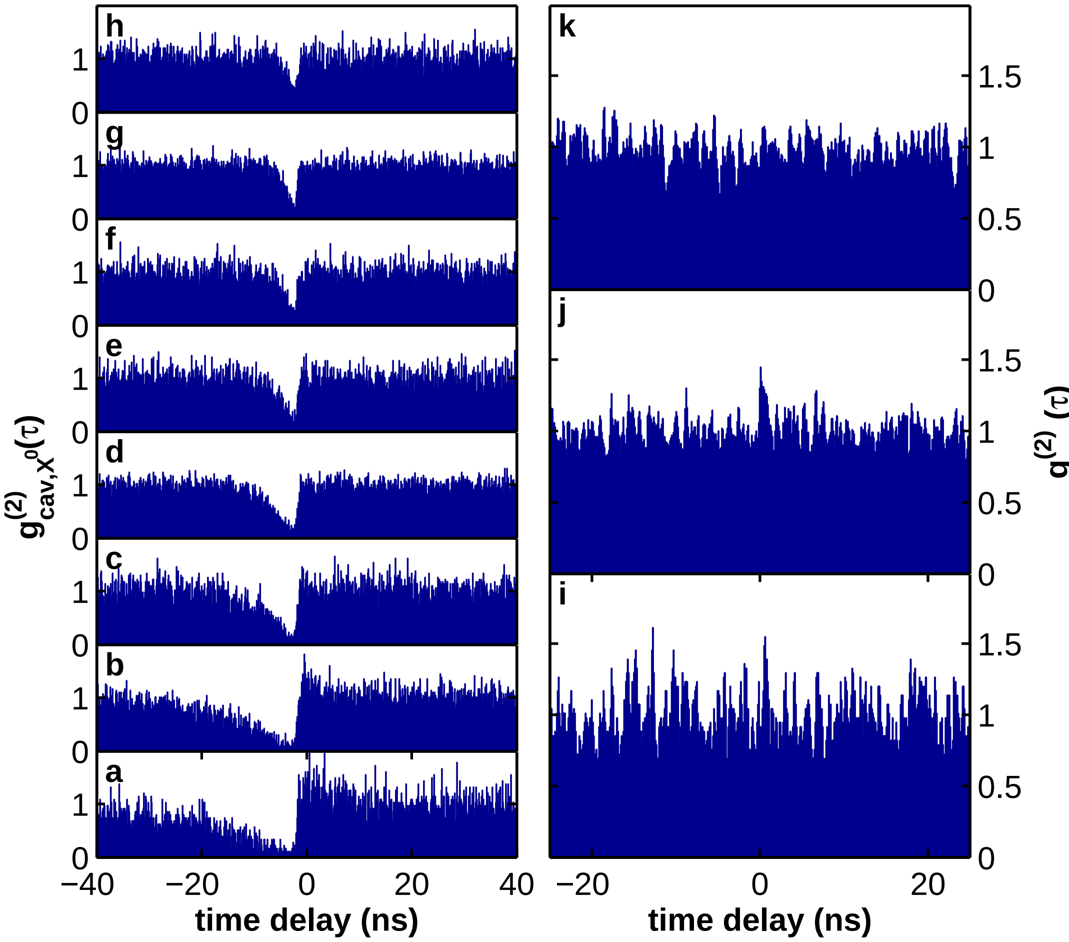

Figure 7.13.: Photon correlations for different pump powers. a–h, Cavity-X^0 cross-correlation for a range of pump powers: $P_{\mathrm{ex}}/P_{\mathrm{sat}} \approx 0.25$ (**a**), 0.5 (**b**), 1 (**c**), 2 (**d**), 2.5 (**e**), 3.5 (**f**), 4 (**g**), and 7 (**h**). Clearly, the main effects of increasing the pump power are the disappearance of the bunching feature for $\tau > 0$ and the shortening of the cavity rise time for $\tau < 0$. **i–k**, Cavity auto-correlation for $P_{\mathrm{ex}}/P_{\mathrm{sat}} \approx 0.25$ (**i**), 0.5 (**j**), and 1 (**k**). As described in the main text, bunching is observed for a pump power close to saturation, while no bunching appears for lower and higher pump powers.

is expected to dominate, such that we even expect a reduction of bunching for lower pump powers. Again, this is exactly what we observe: Fig. 7.13(i–k) shows measured $g^{(2)}_{\mathrm{cav}}(\tau)$ curves for different pump powers. Obviously, the bunching feature persists for pump powers around the QD saturation, whereas bunching disappears for both lower and higher pump powers.

In conclusion, the combination of the experimental and theoretical findings presented in this section demonstrates that far off-resonant cavity feeding takes place due to the finite occupancy of QD states in higher excitation manifolds. This effect ensures efficient cavity-mode emission over a wide range of detunings and explains the puzzling photon-correlation signatures first observed in [81]. Moreover, the mechanism found here potentially has far-reaching implications for the common understanding of QD-cavity systems and potentially even provides further insight into the mechanisms underlying lasing in these structures [75].

7.3. Cavity Feeding Mediated by Acoustic Phonons

Since QDs are embedded in a solid-state environment, they are subject to coupling to lattice vibrations of the surrounding material. While the model presented in the previous sections fully explains the phenomenology of off-resonant cavity feeding for a large range of detunings, we find that coupling of the QD excitons to acoustic phonons introduces an additional channel for off-resonant cavity feeding. In particular, the interaction with longitudinal acoustic (LA) phonons leads to the formation of a weak continuum of phonon sidebands [120–123] that can be resonantly enhanced by the cavity mode [124]. In other terms, the energy stored in a QD exciton is transferred directly to the cavity mode, where the energy difference between the two is carried by an acoustic phonon (see schematic in Fig. 7.14).

We investigate this effect by studying PL from the device used in Sec. 6.3, where the cavity mode is initially ∼1 nm blue detuned from the X^{1+} and can thus be tuned into resonance by cryogenic gas adsorption. Fig. 7.15d shows a PL spectrum of the initial situation obtained for a pump power below saturation, which can be seen from the fact that the XX^0 luminescence is rather weak in this case. In addition to the off-resonant cavity mode, the emission from the X^{1+} and the X^0 can clearly be seen. Starting from this situation, the cavity mode is tuned across resonance with the X^{1+} and the X^0 lines. During tuning, the PL is recorded the result of which can be seen in Fig. 7.15a. The spectra were normalized to their integrals, in order to compensate for the effects of sample drift. Figures 7.15b–d are cuts through the PL scan for the cavity wavelengths indicated by the three dotted horizontal lines. When the cavity mode is tuned to the red side of the X^{1+} line (Fig. 7.15c), the PL intensity of the X^{1+} is greatly diminished as compared to Fig. 7.15d, while the cavity mode is strongly enhanced. The same thing occurs when tuning the cavity mode to the red of the X^0 line, as is the case in Fig. 7.15b with a cavity detuning of +0.3 nm with respect to the X^0. Again, the cavity-mode emission is significantly enhanced at the expense of the X^0 line. This trend is also obvious from the false-color plot of Fig. 7.15a. Here, the line intensities of both the X^{1+} and the X^0 are strongly reduced when being approached by the cavity mode. Figure 7.16 shows the integrated line intensities of the cavity mode and the X^0 as a function of cavity wavelength: the X^0 luminescence (blue line) experiences strong quenching when the cavity mode is ∼ 1 nm red detuned, while in the same regime the cavity PL is strongly enhanced. The spurious broad

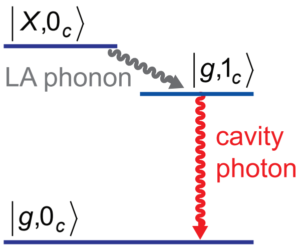

Figure 7.14.: Cavity feeding mediated by LA-phonons. The exciton population is directly transfered to the cavity mode by emission of an acoustic phonon.

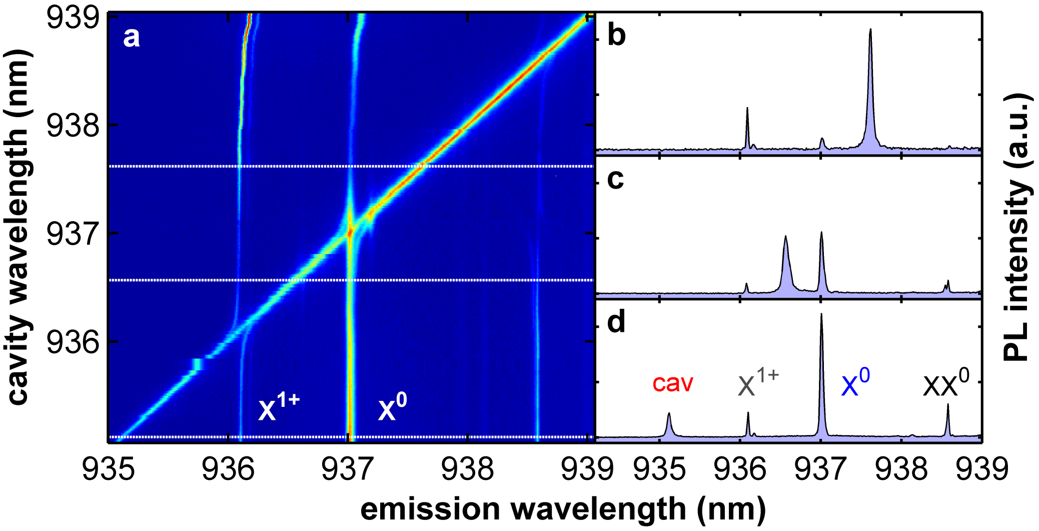

Figure 7.15.: PL spectra when tuning the cavity across resonance with QD excitons. **a**, False-color plot of PL spectra as a function of cavity mode wavelength (vertical axis). The X^{1+} and X^0 lines are labelled in the figure. The horizontal white lines indicate the values of the cavity mode wavelength at which the spectra shown in **b–d** were taken.

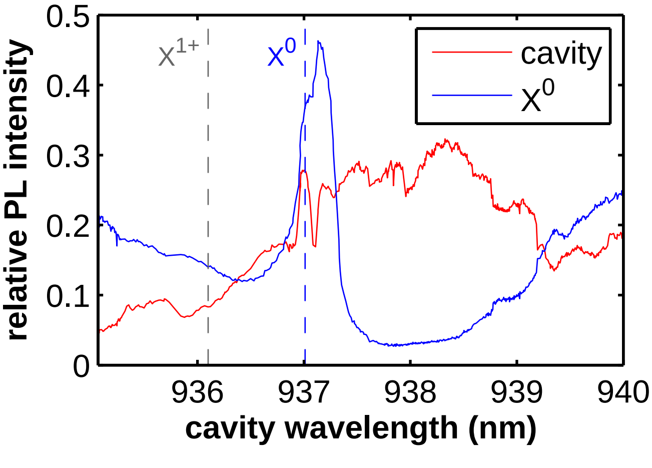

Figure 7.16.: Cavity and X^0 line intensities as a function of cavity wavelength. The X^0 (blue line) is quenched when the cavity mode is red detuned (i.e. for $\lambda_{\mathrm{cav}} = 938$ nm), while the cavity mode (red line) experiences an enhancement due to LA-phonon assisted emission from the X^0 state. The resonant wavelengths of the X^{1+} and the X^0 are indicated by the gray vertical lines.

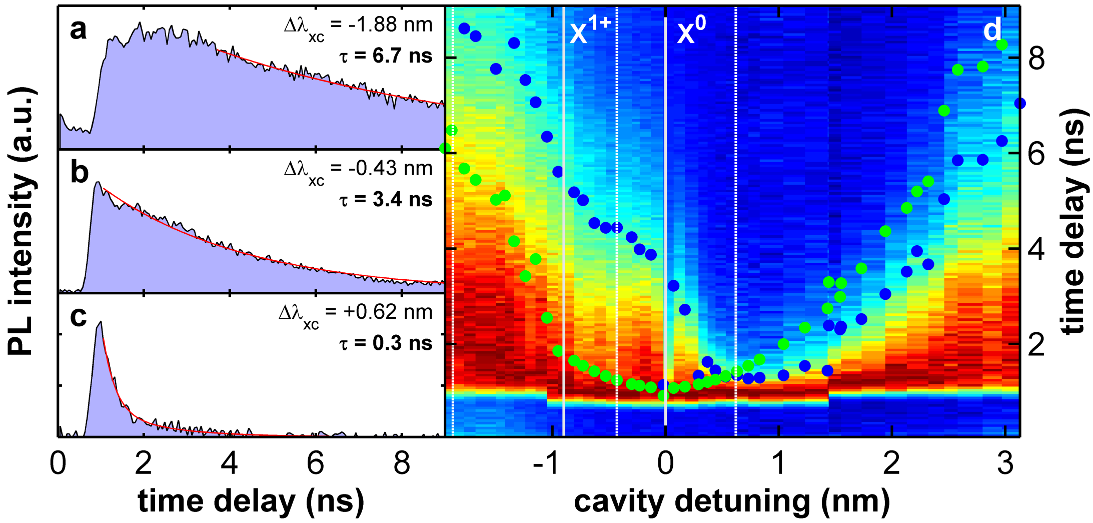

Figure 7.17.: Lifetime of the X^0 as a function of cavity detuning. a–c, TCSPC traces obtained for the detuning values indicated in the corresponding tab. From exponential fits to the data the luminescence decay times τ_{X^0} are determined. **d**, False-color plot of TCSPC traces for different values of the cavity-exciton detuning $\Delta\lambda_{\rm cx}$. The solid vertical lines indicate the spectral locations of the X^{1+} and the X^0, while the dotted vertical lines indicate the detuning values realized in **a–c**. The extracted decay times τ_{X^0} are indicated by blue bullets, the green bullets indicate the expected values according to Eq. (5.2).

peak at the X^0 wavelength is due to the large width of the spectral window used for integration of the X^0 signal[6]. Since we expect a maximum of the phonon density of states to occur around ~1 nm red detuned from the X^0 [120], we attribute the observations made here to direct radiative decay of the X^0 and X^{1+} excitons into the cavity mode via scattering of an LA phonon.

Further evidence in favor of this hypothesis comes from measurements of the X^0 lifetime as a function of cavity detuning using time-correlated single-photon counting (see Sec. 3.1.3). The luminescence decay curve of Fig. 7.17a was obtained when the cavity was $\Delta\lambda_{\rm cx} = -1.9$ nm blue detuned from the X^0. We attribute the initial plateau of the decay curve to the PL pump power being close to saturation[7]. From a single exponential fit to the data (shown as the solid red curve) a luminescence decay time of $\tau_{X^0} = 6.7$ ns is extracted. When tuning the cavity mode in between the X^{1+} and the X^0 lines (corresponding to the situation in Fig. 7.15c), the lifetime decreases significantly and assumes a value of $\tau_{X^0} = 3.4$ ns. More interestingly, for a red-detuning of $\Delta\lambda_{\rm cx} = +0.62$ nm the decay time shortens even further to

---

[6] The window width has to be chosen large enough in order to integrate the entire X^0 line, even in the presence of the temperature-related redshift that occurs for significant amounts of injected N_2.

[7] While the pump power $P_{\rm ex}$ was kept constant for all measurements shown in Fig. 7.17, the saturation power $P_{\rm sat}$ changes during the experiment, since the X^0 lifetime is modified due to coupling to the cavity mode. As a result the ratio $P_{\rm ex}/P_{\rm sat}$ is different for different detunings in Fig. 7.17.

$\tau_{X^0} = 0.3$ ns: although the absolute values of the detuning $|\Delta\lambda_{\mathrm{cx}}|$ are comparable in Figs. 7.17b and 7.17c, the timescales of exciton decay differ significantly.

This asymmetry is particularly obvious from Fig. 7.17d, which shows TCSPC traces like the ones in Figs. 7.17a–c for a large range of detunings in a false-color plot[8]. Here, the ordinate axis denotes the time delays between the excitation laser pulse and the photon detection event. Obviously there is a remarkable asymmetry of the decay dynamics around zero detuning, which is indicated by the solid horizontal line corresponding to the X^0 resonance.

The observed asymmetry is fully consistent with the model of LA-phonon assisted cavity feeding. In the case of a blue detuned cavity mode, excitation of the cavity mode via the X^0 state requires the *absorption* of a phonon, whereas for red detuning cavity excitation can occur via phonon *emission*. At the experiment temperature of nominally $T = 4$ K the phonon system is populated up to an energy of $k_{\mathrm{B}}T \sim 0.5$ meV, such that no phonon absorption should occur for values of $\Delta\lambda_{\mathrm{cx}}$ substantially larger than that. On the other hand, spontaneous phonon emission can occur independently of the population of the phonon bath[9] and can be effective over a larger spectral range, which is determined by the coupling matrix element between QD states and the LA-phonon system. The latter exhibits a distinct cut-off energy that corresponds to a phonon wavevector comparable to the inverse QD confinement length scale [120].

Additional support for the model of LA-phonon mediated cavity feeding comes from pump-power dependent PL measurements carried out in the regime, where strong cavity excitation via the X^0 occurs, e.g. for the detuning value realized in Fig. 7.15d. Figure. 7.18 shows the pump-power dependence of the cavity mode (red bullets) together with that of the X^0 and the XX^0 (blue and black bullets). In contrast to the results for the far off-resonant case (Fig. 7.5), the cavity mode PL here follows a linear pump-power dependence like the X^0 for a very broad range of pump powers. This observation identifies phonon-assisted coupling of the cavity mode to the X^0 transition as a relevant feeding mechanism in the near-resonant regime.

In order to investigate LA-phonon mediated cavity feeding in a more quantitative fashion, the TCSPC traces shown in Fig. 7.17d were fit by exponential decay curves as described in Sec. 3.1.3. The extracted values of the X^0 decay time τ_{X^0} are plotted as a function of detuning (blue bullets in Fig. 7.17d), in which they essentially trace out an *equipotential line* of the false-color plot. Theoretically, the X^0 lifetime for a given detuning can be calculated from the imaginary part of the polariton complex eigenfrequency given in Eq. (5.2). For detunings $\Delta\lambda_{\mathrm{cx}} \gg g, \kappa, \gamma$ this corresponds simply to the detuning-dependent Purcell effect[10], which yields[11]

$$\frac{1}{\tau_{X^0}} = \frac{1}{\tau_{X^0}^{\infty}} + \frac{4g^2}{\kappa}\frac{\kappa^2}{4\Delta\omega_{\mathrm{cx}}^2 + \kappa^2} \tag{7.3}$$

---

[8] In order to obtain this plot, all TCSPC traces were normalized to their peak height to create a uniform color scaling in the plot.

[9] Absorption for a phonon wavevector $\boldsymbol{q}$ is proportional to the population of that mode $N_{\boldsymbol{q}}$, whereas emission of a phonon is proportional to $N_{\boldsymbol{q}} + 1$.

[10] Strictly speaking, the lifetime modification observed here is not due to the Purcell effect, but due to the lifetime of the upper/lower polariton branch. Nonetheless, due to the strong qualitative and quantitative similarity for large detunings we use the term *Purcell effect* here.

[11] This expression simply corresponds to a generalization of Eq. (2.19) for finite detuning.

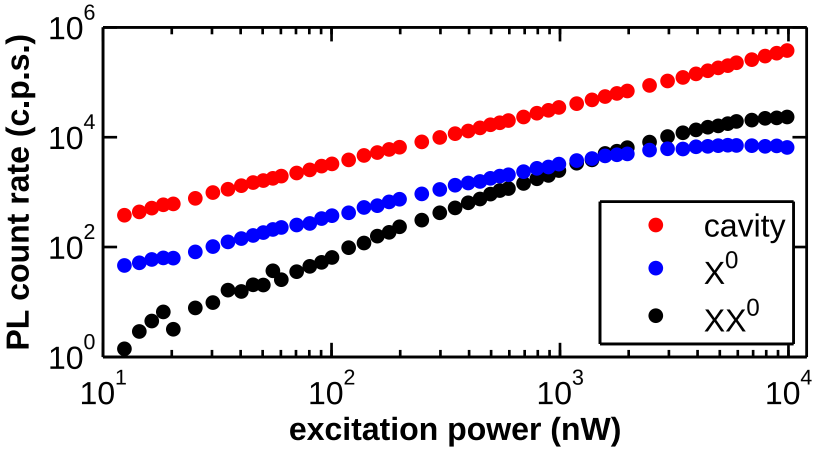

Figure 7.18.: Pump power dependence in the LA-phonon feeding regime. The integrated line intensities of the off-resonant cavity mode is shown together with those of the X^0 and the XX^0 lines. For this measurement the cavity mode was red detuned from the X^0 by $\Delta\lambda_{\rm cx} = +0.62$ nm. Here, the cavity mode follows a linear pump-power dependence.

for the cavity X^0 decay time τ_{X^0}. Here, $\tau_{X^0}^{\infty}$ corresponds to the value of τ_{X^0} in the case of a far off-resonant cavity, however with the QD still well inside the photonic bandgap of the photonic crystal. By assuming $\hbar g = 140$ μeV as extracted from the anticrossing feature of the X^0, $\hbar\kappa = 75$ μeV corresponding to the cavity Q factor of $Q \sim 17\,500$, and $\tau_{X^0}^{\infty} = 20$ ns, we obtain the values indicated by the green bullets in Fig. 7.17d[12]. The most obvious discrepancy between the two curves is the asymmetry of the experimentally determined values around zero detuning, while the theoretical expectation is symmetric.

Again, support for the model of LA-phonon mediated cavity feeding comes from the fact that for red detunings the experimental values of τ_{X^0} are systematically lower than those expected from standard Purcell effect. Surprisingly, the X^0 lifetimes τ_{X^0} for blue detuning (i.e. for $\Delta\lambda_{\rm cx} < 0$) are *longer* than the expected values. Moreover, the false-color plot in Fig. 7.17d shows a distinct elevation in a ± 0.5 nm wide window around $\Delta\lambda_{\rm cx} = 0$. This is most likely due to the non-trivial fine structure of the X^0 that is further complicated by the angular misalignment between the X^0 dipoles and the cavity polarization axes in this device (see discussion in Sec. 6.3). In the experiment, only light polarized parallel to the cavity mode was collected in order to maximize the signal of the exciton component $|X_\theta^0\rangle$ parallel to the cavity mode. However, the emitted light shows a more complicated polarization behavior when the resonance condition is approached: the excitonic component parallel to the cavity mode polarization (i.e. the one primarily collected) is shifted out of the detection window due to vacuum Rabi splitting such that collected signal in this regime stems

---

[12] The asymmetric appearance of the theoretical curve arises from the fact that for fitting of each TCSPC curve a different starting time t_0 was chosen in order to exclude the rising slope and the initial plateau that occurs for the TCSPC traces of long lifetime like the one shown in Fig. 7.17a. This detuning-dependent t_0 was then added to each calculated τ_{X^0} in Fig. 7.17d

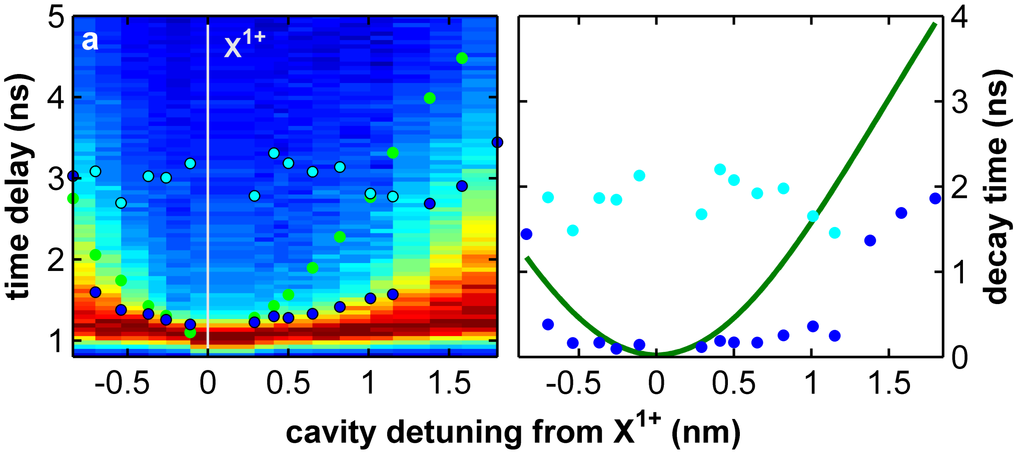

Figure 7.19.: Lifetime of the X^{1+} as a function of cavity detuning. **a**, False-color plot of TCSPC traces for different values of the X^{1+}-cavity detuning. The solid vertical line indicates the spectral location of the X^{1+}. The extracted time constants $\tau^{(1)}_{X^{1+}}$ and $\tau^{(2)}_{X^{1+}}$ are indicated by blue and light blue bullets, respectively. The green bullets indicate the corresponding theoretical values in the absence of LA-phonon coupling. **b**, Comparison of the decay times $\tau^{(1)}_{X^{1+}}$ and $\tau^{(2)}_{X^{1+}}$ with the theoretical curve in the absence of LA-phonon coupling (green line).

from the orthogonal exciton $|X^0_\perp\rangle$. As discussed in Sec. 6.3, the latter undergoes coupling to the cavity mode via the exchange splitting δ. In a window around $\Delta\lambda_{\text{cx}} = 0$, one therefore collects predominantly light from $|X^0_\perp\rangle$, which exhibits a longer decay time as compared to the coupled exciton. The observed luminescence decay traces are then superpositions of the decay curves of the two excitons, where the relative weighting of the two depends on the analyzer setting and the width of the spectral window used for the integration.

The observation of a longer lifetime for blue detuning, however, is not fully understood at this point. A possible explanation could be related to a systematic overestimation of the X^0 lifetimes when they become comparable to the time window that can be used for fitting: due to the large laser repetition rate of $f_0 = 76.6$ MHz and due to the occurrence of the initial plateau in the TCPSC decay curves, the time window that can be used for fitting the data is only $\sim 6 - 7$ ns wide for the long-lived TCSPC trace (as an example see Fig. 7.17a). Obviously this results in a reduced accuracy of the fits if the data exhibits luminescence decay times comparable to that of the time window used.

A possible way to circumvent this problem in future experiments is the use of a different laser source of lower repetition rate. Alternatively, the non-trivial influence of the X^0 fine structure could be avoided by performing detuning-dependent TCSPC measurements on an excitonic transition that does not exhibit any fine structure. Accordingly, we carried out some preliminary measurements on the X^{1+} transition of the QD, as can be seen in Fig. 7.19a. Like in Fig. 7.17d, the green bullets indicate the values obtained from a theoretical estimate of the cavity-induced lifetime of the

X^{1+} line[13], while the blue bullets show the experimental decay times $\tau^{(1)}_{X^{1+}}$ obtained from bi-exponential fits to the decay curves:

$$I_{X^{1+}}(t) = I_{dark} + I^{(1)}_{X^{1+}} \exp\left(-\frac{t-t_0}{\tau^{(1)}_{X^{1+}}}\right) + I^{(2)}_{X^{1+}} \exp\left(-\frac{t-t_0}{\tau^{(2)}_{X^{1+}}}\right). \tag{7.4}$$

Fits using a single exponential did not provide reasonable agreement with the data in this case. We find that the second decay timescale is more or less constant for the recorded detunings and has a value of $\tau^{(2)}_{X^{1+}} \approx 2$ ns, while the fast decay time $\tau^{(1)}_{X^{1+}}$ displays the characteristic lifetime-shortening due to the combined influence of the cavity mode via Purcell effect and LA-phonon coupling. The longer timescale $\tau^{(2)}_{X^{1+}}$ is shown by the light blue bullets in Fig. 7.19a.

The two extracted timescales are also shown in Fig. 7.19b as blue and light-blue bullets, respectively, superimposed with the expected detuning-dependent lifetime estimated from the Purcell effect (solid green line). Like in the case of the X^0, the X^{1+} decay time $\tau^{(1)}_{X^{1+}}$ is substantially shorter than the expected value when the cavity mode is red detuned.

Due to the minimal cavity-mode detuning of ~ -1nm from the X^{1+} line, a smaller range of blue detunings can be addressed here, as compared to the data taken on the X^0. Hence, the measurements presented on the X^{1+} do not allow for very detailed conclusions on the behavior of $\tau_{X^{1+}}$ for blue detuning. Moreover, the detuning steps were chosen larger here as compared to the X^0 case. In order to gain a better understanding of the dynamics of LA-phonon mediated cavity feeding, it is therefore desirable to acquire additional data in the future.

7.3.1. Photon Correlations in the Phonon-Feeding Regime

As outlined in Sec. 7.2.3 and Sec. 7.1.2, the absence of any significant correlations in the photon stream emitted from an off-resonant cavity mode suggested that excitation of the cavity mode does not proceed by direct channeling of the energy of discrete exciton states into the cavity mode. Instead feeding occurs from a quasi-continuum of higher-excited QD states that in particular allow for the occurrence of cascaded emission into the cavity mode. In contrast, in the regime of LA-phonon feeding exactly the former situation is realized: QD excitons can undergo direct decay to a cavity photon by emission (or absorption) of an acoustic phonon. Certainly, in this regime, feeding from higher excited QD manifolds still plays an important role, as the latter mechanism is expected to display only weak dependence on the precise detuning from the QD excitons. However, e.g. for a detuning like the one shown in Fig. 7.15d, the off-resonance cavity PL increases by a factor of $\sim$3–4 as compared to the off-resonant case, implying that LA-phonon feeding surpasses feeding from QD background states by a factor of $\sim$2–3. In this regime, it is hence natural to assume that the photon stream emitted by the cavity mode predominantly exhibits the quantum statistics of the exciton state that provides the majority of cavity feeding. Surprisingly, however, auto-correlation measurements of the phonon-mediated cavity-PL in fact show strong bunching at $\tau = 0$, as can be seen in Fig. 7.20a.

---

[13] Here a coherent coupling strength of $\hbar g = 99$ μeV was used, as extracted from the anticrossing-feature on the X^{1+}.

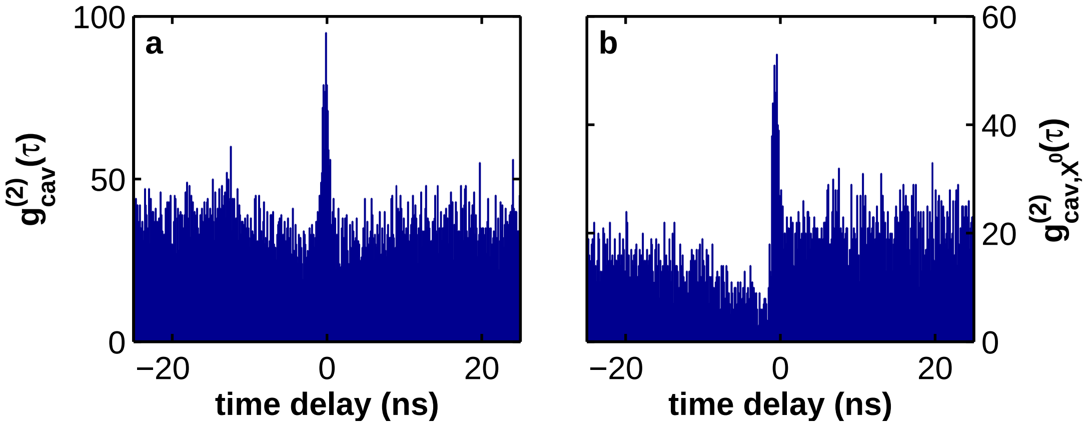

Figure 7.20.: Photon correlations in the LA-phonon feeding regime. a, Cavity auto-correlation $g^{(2)}_{\rm cav}(\tau)$ for a cavity detuning of $\Delta\lambda_{\rm cx} = 0.78$ nm for a pump power below saturation. Surprisingly, a strong bunching peak at $\tau = 0$ appears. **b**, X^0-cavity cross-correlation trace $g^{(2)}_{{\rm cav},X^0}(\tau)$ for the same detuning.

Similarly, photon cross-correlations between the X^0 and the cavity mode in the same regime also reveal unexpected features: Fig. 7.20b shows an experimental cross-correlation trace $g^{(2)}_{{\rm cav},X^0}(\tau)$ obtained in the same regime. Like in the case of far red-detuning (see Fig. 7.11a), this curves exhibits the characteristic asymmetric shape around $\tau = 0$. However, here a sharp bunching peak arises at $\tau = 0$. From a precise measurement of the optical path length differences in the correlation setup we find that this bunching peak is in fact symmetric around $\tau = 0$. On the one hand this observation reflects that the X^0 and cavity emission arise from the same optical transition, on the other hand, the occurrence of bunching is again completely unexpected in this case.

The origin of these puzzling photon-correlation features is not well understood at present. A better understanding of these features therefore requires more refined experiments in the future.

8. Resonant Scattering Spectroscopy

While PL is an extremely powerful technique for detecting all possible optical transitions of a QD in a parallel fashion, it has the significant disadvantage of being completely incoherent. Excitation of the system typically occurs far off-resonance from the spectral emission band and the intra-dot relaxation processes that populate the QD states occur via incoherent loss mechanisms. For quantum optical experiments, however, and in particular for those aimed at the implementation of quantum information processing tasks, it is desirable to selectively address isolated optical transitions of the system in a resonant and coherent way.

In atomic physics a large variety of such techniques exists and are well-developed. Resonant spectroscopy typically relies on the detection of the modification of a probe laser caused by the interaction with an emitter. Absorption spectroscopy of atomic vapors for example is based on this principle. Here, the change of transmission through a gas cell is monitored when tuning the probe laser across resonance with atomic transitions. Naturally, this technique benefits from the large optical density in a gas cell that yields strong attenuation of the probe laser beam. Another approach is based on the measurement and analysis of the scattered light itself, while the excitation laser is fully suppressed. In systems dealing with trapped atoms or ions, this is accomplished by purely geometrical means: the atoms are addressed from different spatial directions for excitation and collection.

Naturally, the implementation of similar techniques for solid-state quantum optics is highly desirable. In contrast to gaseous atomic media, however, resonant excitation of solid-state systems is hampered by the strong back-reflections[1] at the sample surface that typically overwhelm the scattered light containing the desired information by several orders of magnitude[2]. Moreover, while absorption spectroscopy is a straightforward technique for systems of large optical density, the absorption cross-section of a single QD is typically too weak to be observed directly. Typically, the resonant change in transmission of a strongly focused laser beam caused by a single QD exciton amounts to $\sim 10^{-4} - 10^{-3}$ [125], making its obersvation a non-trivial task. Transmission spectroscopy of single QDs hence typically relies on a lock-in technique based on modulation of the QD-laser coupling by periodically shifting the QD on and off resonance with the laser field. The QD resonance frequency can be modified by exploiting the quantum confined Stark effect induced by an electric field aplied via a Schottky-contact on top of the sample surface [59].

---

[1] The large refractive index of GaAs ($n \approx 3.5$) results in an intensity reflection coefficient of approximately 30%.

[2] Obviously, this problem is easily circumvented in PL, where the excitation light can easily be distinguished from the emission by spectral filtering via interference filters or colored glasses.

However, integrating high-Q PC cavities with gates is a highly non-trivial task, since the gate material introduces large absorption and thus demands a more involved sample design. Meanwhile techniques have been developed for gating PC cavities using heavily doped GaAs layers rather than metallic contacts [83, 104].

An alternative ansatz for experiments in cavity QED is resonant spectroscopy on the photonic channel of the cavity mode degree of freedom, rather than on the material channel provided by the QD. The basic idea behind this approach is that resonant coupling to the cavity mode exhibits larger efficiency than coupling to a single QD. The following sections provide an overview over resonant scattering experiments performed in the context of this dissertation, all of which rely on free-space optical spectroscopy realized in reflection geometry. For completeness, it has to be mentioned that large efforts are being made in the community to achieve better coupling to microcavities and other nanostructures by near-field optical means. In particular, the use of fiber-taper based optical waveguides has proven to be of great value for cavity QED [106, 108, 126].

8.1. Reflection Spectrum of a PC Cavity

In atomic cavity QED experiments, resonant spectroscopy typically is performed by monitoring the transmission spectrum of the cavity mode [127]. In the case of a standard Fabry-Pérot resonator, this approach naturally results in strong transmission changes when probing the system with a Gaussian laser beam, since in this setting a good mode overlap of the probe beam and the intra-cavity field can be achieved[3]. PC cavities, on the other hand exhibit a far-field emission that strongly deviates from a Gaussian beam-profile, such that the mode-matching condition cannot be well fulfilled for an incident Gaussian laser beam. Heuristically one can argue that the field distribution of the L3 cavity shown in Fig. 2.11, having a large effective mode index of $n_{\text{eff}} = 2.9$ [65], results in a small overlap with a Gaussian beam in vacuum. In fact, the very design principle followed towards achieving high Q-factors entails a reduction of the cavity mode emission in z direction (see Sec. 2.3.3), such that the coupling to an incident laser beam is expected to be small.

In order to evaluate the efficacy of resonant probing schemes for experiments involving PC cavities, the resonant reflection spectra of several devices were studied. Experimentally, this was achieved with the same setup as for PL measurements, but using a tunable diode laser for excitation of the sample. A major technological difficulty of such experiments stems from the fact that only a limited number of commercially available laser systems offer the feature of mode-hop free tuning over

---

[3] A cavity QED experiment based on QDs embedded in an integrated micropillar-cavity supporting a Gaussian-like cavity mode has been reported on in [128].

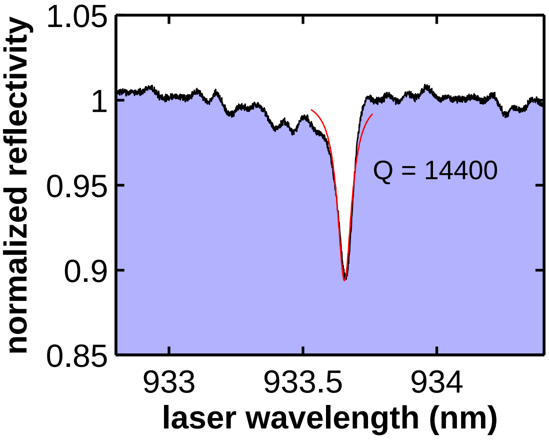

Figure 8.1.: Reflection spectrum of an L3 cavity. The reflectivity dip due to the scattering off the cavity mode can clearly be identified. The red line is a Lorentzian fit to the data.

frequency ranges exceeding a few tens of GHz in the spectral region of the near infrared. The only laser system available at the time was the NewFocus TLB-6319 Velocity™ that allows for mode-hop free wavelength tuning over the entire operation range of $\sim$15 nm.

The excitation laser beam was focused to a diffraction limited spot in the center of the PC cavity using a microscope objective with a numerical aperture of NA = 0.55 that corrects for the aberrations introduced by the cryostat window (see Apendix A). Resonant spectroscopy in reflection geometry relies on the interference between back-reflected laser light and the field scattered by the cavity mode that are superimposed on the detector. In order to maximize this interference signal, it is hence desirable to employ a detector that predominantly collects light from the same optical mode as the excitation beam, while blocking all other optical modes. In the confocal microscopy setup used in this work, this is naturally implemented. The reflection signal is collected with an NA-matched single-mode fiber and then directed to a photodetector that measures the reflected laser light as a function of excitation wavelength.

Figure 8.1 shows the result of such a measurement performed on the same QD-cavity device as used in Chap. 5. For this measurement the probe laser delivered a power of $P_{\mathrm{ex}} \approx 20$ nW to the sample surface. The back-reflected signal is normalized to the average value for large detuning of the probe laser from the cavity mode. Moreover, in order to reduce 1/f noise, the excitation laser intensity was modulated at a frequency of 342 Hz using an acousto-optical modulator (AOM) and the reflected signal from the sample was then analyzed by a lock-in amplifier, yielding a detection bandwidth of 10 Hz. The reflectivity-dip induced by resonant scattering on the cavity mode can clearly be seen at $\lambda_{\mathrm{cav}} = 933.66$ nm and creates a signal contrast of $\approx 10\%$ in this case. Moreover, this feature can be fit by a Lorentzian curve yielding a Q factor of $Q \sim 14\,400$.

As can be seen in Fig. 8.1, the background reflection signal is subject to modulations at the $\sim 1-2\%$ level. These modulations are due to interference effects at the optical elements used for guiding the excitation laser and the collected signal. Although the excitation laser is actively stablized to deliver constant power, a residual modulation is introduced by the transmission through the anti-reflection coatings of the beamsplitters used to steer the beam. Typically they do not exhibit a completely flat wavelength response on a scale of ~ 1 nm. Generally, reflectivity measurements over a tuning range on the order of ~ 1 nm are complicated by the fact that typical plane-parallel optical elements with a thickness in the range of milimeters produce etalon fringes with a free spectral range (FSR) comparable to the spectral features of interest. A key design principle for the optical layout of such experiments is thus the minimization of the number of optical elements immersed into the beam. An additional means to reduce the influence of background etalons comes from spectral filtering of the time-dependent reflectivity signal: in the measurements presented in Fig. 8.1, the finite detection bandwidth of 10 Hz in the employed lock-in scheme results in a smoothing of the reflectivity curve, such that etalons with a FSR significantly lower than ~ 0.05 nm are flattened out.

As mentioned above, the confocal nature of the optical system plays a key role in restricting the signal collection to the mode that is used for resonant excitation of the cavity mode. This hypothesis is supported by control measurements in which the reflected signal was collected using a multi-mode instead of the single-mode fiber. Using this setup, no cavity-related reflection dip could be observed, which is most probably due to the fact that this detection scheme allows for the efficient collection of additional modes with weaker spatial coherence compared to the signal of interest.

Surprisingly, the strong reflection signal observed on this device could not be reproduced on every other device investigated. Attempts made, typically yielded a weak reflectivity change on the order of $\sim 1\%$ or less. In this case, the reflectivity change is on a similar scale as the background modulations, which renders the resonant spectroscopy technique not feasible in this case.

8.2. Crossed-Polarization Resonant Scattering

A potential solution to the problem of inferior mode-matching mentioned above is given by a crossed-polarization scheme, in which the back-reflected laser light can be distinguished from the cavity signal according to its polarization. To this end the excitation beam is linearly polarized at an angle of $+45\,^\circ$ with respect to the polarization direction of the L3 cavity. The polarizer in the detection channel (*analyzer*) then is set to collect linearly polarized light at an angle of $-45\,^\circ$, such that the directly back-reflected laser signal is canceled, while $\sim 50\%$ of the cavity signal can pass [82, 129].

Figure 8.2 shows the result of a resonant scattering measurement using the crossed-polarization technique carried out on the same device that was used in Fig. 8.1. For this measurement the system was driven with a laser power of $P_{\mathrm{ex}} = 100$ nW on the sample surface. The light scattered off the cavity mode is clearly visible as a pronounced peak at $\lambda_{\mathrm{cav}} = 932.5$ nm, which in this case rises to about four times the value of the background signal. Again, the feature is nicely fit by a Lorentzian curve,

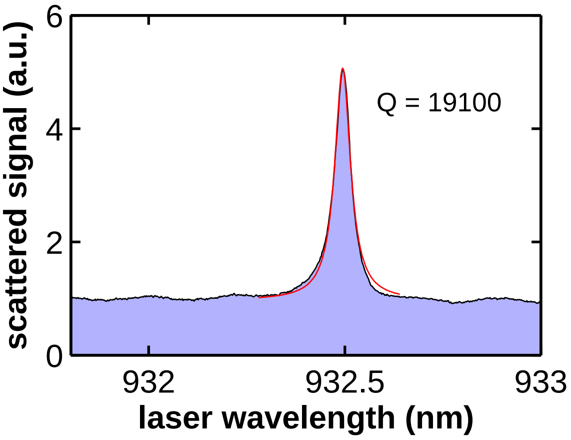

Figure 8.2.: Resonant scattering using a crossed-polarization scheme. The scattering signal of the cavity mode appears as a peak that rises ~ 4 times above the background.

this time yielding a Q-factor of $Q \approx 19\,100$. The difference between this Q factor and the one determined in Fig. 8.1 can most probably be related to the asymmetry of the curve in Fig. 8.1. The slight residual asymmetry of the cavity mode profile in Fig. 8.2 is most probably related to a slight misalignment of the polarizer axes, which results in an interference effect between the cavity signal and the reflected laser light[4].

Moreover, the technique of crossed-polarization RS turns out to be less device-dependent than the direct measurement of reflectivity, as the technique could successfully be applied to several different devices.

8.3. Observation of Vacuum Rabi Splitting

The technique of crossed-polarization RS can be employed to observe vacuum Rabi splitting when tuning the cavity mode on resonance with the X^0 transition of the QD. In this case, the polaritons are probed via their photonic channel, in contrast to PL, where the system is excited via the emitter-part of the QD-cavity system. In order to study strong-coupling physics by resonant excitation we performed RS scans on the device used in Sec. 6.3. In this device, no reflectivity change as shown in Fig. 8.1 could be observed, indicative of an inferior mode-matching as compared to the data shown in Sec. 8.1, such that application of the crossed-polarization technique was necessary. From a comparison of the excitation power sent to the cavity and the back-scattered signal after polarization selection, the total throughput-efficiency is found to be $\sim 10^{-4}$. When assuming a suppression of the scattered cavity light by a factor of 50% at the analyzer and the same coupling efficiency for

---

[4] A related polarization dependence in the resonant-scattering spectra of single molecules has been reported in [130].

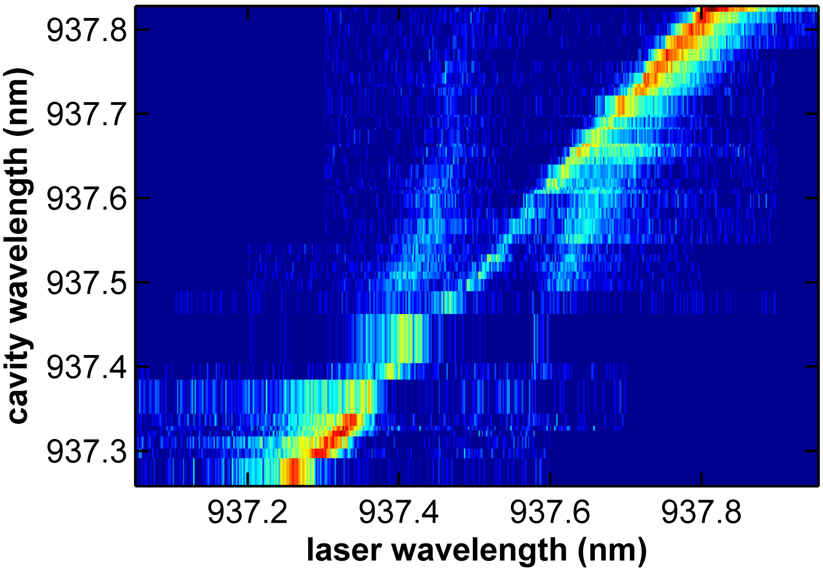

Figure 8.3.: Resonant scattering scan of vacuum Rabi splitting. RS traces taken when the cavity mode is tuned across resonance with the X^0 transition of the QD. The anticrossing feature induced by the vacuum Rabi splitting is clearly visible, together with an unexpected central line arising from resonant scattering at the uncoupled cavity wavelength.

the excitation and the collection ports, the mode-matching here leads to a coupling efficiency of $\eta \approx 1.5\%$ for this device.

When tuning the X^0 on resonance and acquiring RS spectra in this regime, we find that the excitation pump power has to be reduced to the range of $\sim$10–20 pW, in order to observe the polariton states. This corresponds to an excitation power approximately four orders of magnitude smaller than that used in Fig. 8.1 ans Fig. 8.2. In this regime, the scattered signal is in the sub-femtowatt regime, such that detection with standard photodiodes becomes unfeasible. We therefore employed a Si-based APD detector (Perkin Elmer SPCM-AQR-14) that provides a photon detection efficiency of 20%. In the optical setup for RS spectroscopy using APD detection the analyzer is positioned after the collection fiber. This allows us to use polarization paddles for the continuous adjustment of the polarization state of the collected signal, such that we can achieve a suppression of the excitation laser on the order of 1 : 20 000.

The results of RS scans obtained while tuning the cavity mode across the X^0 resonance can be seen in Fig. 8.3. These measurements were obtained for an excitation power of $P_{\text{ex}} = 22$ pW on the sample surface. Far-off resonance, the collected signal amounts to $\approx$2400 counts per second on the APD, corresponding to a signal strength of $\approx$2.4 fW. When the cavity approaches resonance, the characteristic anticrossing indicative of the formation of polaritons can clearly be seen. Figure 8.4a shows a single RS trace obtained on exact resonance with the X^0 line. The splitting of the two outer spectral features amounts to 0.2 nm, corresponding to a vacuum Rabi splitting of $2g = 140$ μeV, in agreement with the PL measurements presented

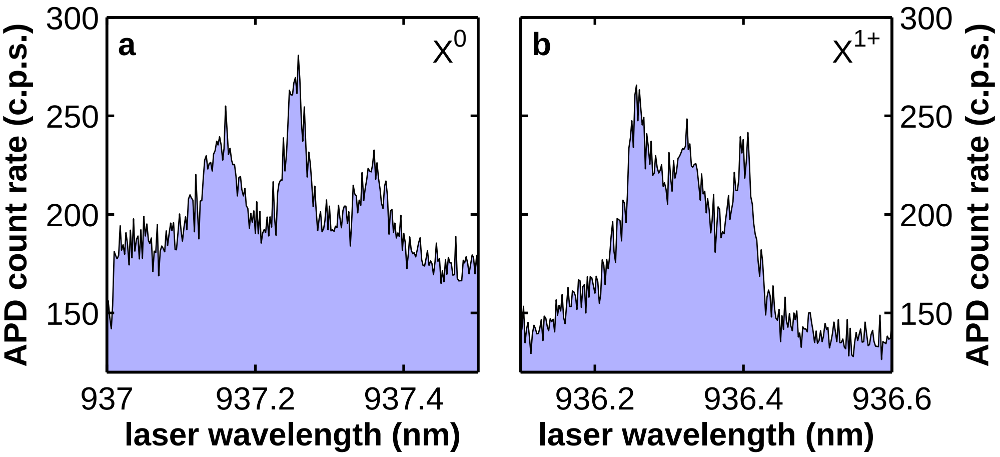

Figure 8.4.: Single RS traces in strong coupling with the X^0 and the X^{1+}. **a**, RS trace showing the vacuum Rabi splitting formed when the cavity mode is tuned on resonance with the X^0 line of the QD. Surprisingly, a peak corresponding to the uncoupled cavity mode appears in the center of the strong-coupling doublet. **b**, Strong coupling RS trace when the cavity is tuned on resonance with the X^{1+}. Surprisingly, polaritons are formed, indicative of charging of the QD.

in Sec. 6.3. Accordingly, we observe a reduction of the scattered intensity on each polariton branch, corresponding to the division of the cavity degree of freedom on two separate spectral features.

Surprisingly, an additional peak is present in the center of the strong-coupling doublet, very much reminiscent of the uncoupled cavity peak in the strong coupling scans in PL reported in previous chapters. Like in the PL scans shown in Figs. 5.3, 6.2, and 6.5, this central peak directly reflects the uncoupled cavity mode: the spectral position is the same as the uncoupled cavity mode and it exhibits a linewidth corresponding to the bare cavity Q factor. However, its occurrence here is not compatible with the behavior expected for a two-level system coupled to the cavity mode that is subject to coherent excitation.

Despite the strong qualitative similarity of the data observed in PL and RS, it has to be noted that the mechanisms underlying the appearance of the central peak are of completely different nature in the two cases. In PL the central cavity peak arises since cavity feeding occurs from excited or charged QD states other than X^0, such that the cavity mode can be excited at times when the QD does not occupy the X^0 state. As a result, the coupled polariton peaks and the uncoupled cavity mode co-exist in the time-integrated PL spectrum. In resonant scattering, however, a signal arising from the uncoupled cavity mode does not arise from cavity mode *emission* but rather from *scattering* off the cavity mode. However, in the presence of vacuum Rabi splitting of the X^0 transition, the only optical transitions that can exist for an empty QD in the absence of additional charges in the ground state are those to the strongly-coupled polariton states $|p_\pm\rangle$.

Following these arguments, the occurrence of a finite scattering signal from the uncoupled cavity mode hence indicates that during part of the integration time the QD does not fulfill a resonance-condition with the X^0 transition, such that the cavity mode reverts to its uncoupled location and thus produces a scattering peak in the center of the anticrossing feature. A potential explanation could be given by random charging events of the QD: if the QD captures e.g. an extra hole, the fundamental optical transition is that to the positively charged trion X^{1+}, such that the QD exciton dipole is shifted off-resonance from the cavity mode. As a result, no polaritons are formed, and the system can scatter at with the uncoupled cavity mode wavelength until the extra charge leaves the QD again. However, the occurrence of charging events in this system is rather surprising: the probe laser is far below the bandgap, the shallow defect states, and the wetting layer, such that the origin of this effects are still unknown.

Additional support for the hypothesis of random QD charging comes from the observation of a strong-coupling related anticrossing feature on the X^{1+} line of the QD that can be probed in RS, as can be seen in Fig. 8.4b. In the absence of any charging events, the QD should be predominantly empty at $T = 4$ K, making the X^0 the only possible optical transition of the QD. The cavity mode — even when resonant with the X^{1+} transition — should not "see" a transition it could strongly couple to. The observation of vacuum Rabi splitting with the X^{1+} therefore indicates that part of the time the QD is charged with an extra hole.

In order to investigate the nature of the processes leading to charging of the QD, we carried out pump power dependent measurements of the strong-coupling feature shown in Fig. 8.4. Figures 8.5a–e show several RS traces obtained for different excitation power. When moving from the lowest pump power of $P_{\text{ex}} = 1.3$ pW in Fig. 8.5a to $P_{\text{ex}} = 9.7$ pW in Fig. 8.5e, one can clearly see that the central peak grows faster than the polariton peaks. Figure 8.5f shows the extracted peak heights as red bullets together with a quadratic fit (blue line) that reproduces the data in a reasonable fashion. The quadratic power dependence of the uncoupled cavity mode scattering peak suggests that the mechanism leading to the appearance of this peak itself depends linearly on the excitation laser power. In the hypothetical model given above, this means that the charge fluctuations of the QD are induced by the probe laser. At this point, however, it is not clear, if this effect relies on the standard interaction of a below-bandgap laser field with the host material, or if it becomes enhanced due to interaction with the cavity mode. A possible experiment could be to perform scans like those shown in Fig. 8.5 in the presence of an additional off-resonant below-bandgap laser.

The quadratic power dependence of the uncoupled cavity mode emission constitutes a particularly surprising observation, since the occurrence of a nonlinearity at pump powers at the picowatt-level is rather unexpected. In fact, the average photon population of the uncoupled cavity mode with decay rate κ, continuously driven with power P_{ex} is given by

$$\left\langle \hat{a}^\dagger \hat{a} \right\rangle = \eta \frac{P_{\text{ex}}}{\hbar\kappa\omega_{\text{av}}}, \tag{8.1}$$

where $\eta \approx 1.5\%$ is the coupling efficiency to the cavity mode. For an excitation power of $P_{\text{ex}} = 10$ pW and a cavity decay rate of $\hbar\kappa = 75$ μeV this yields $\left\langle \hat{a}^\dagger \hat{a} \right\rangle \approx 6 \cdot 10^{-6}$, meaning that two-photon excitation of the cavity should be negligible. Furthermore, from the same argument it is clear that the saturation of the polariton peaks at this

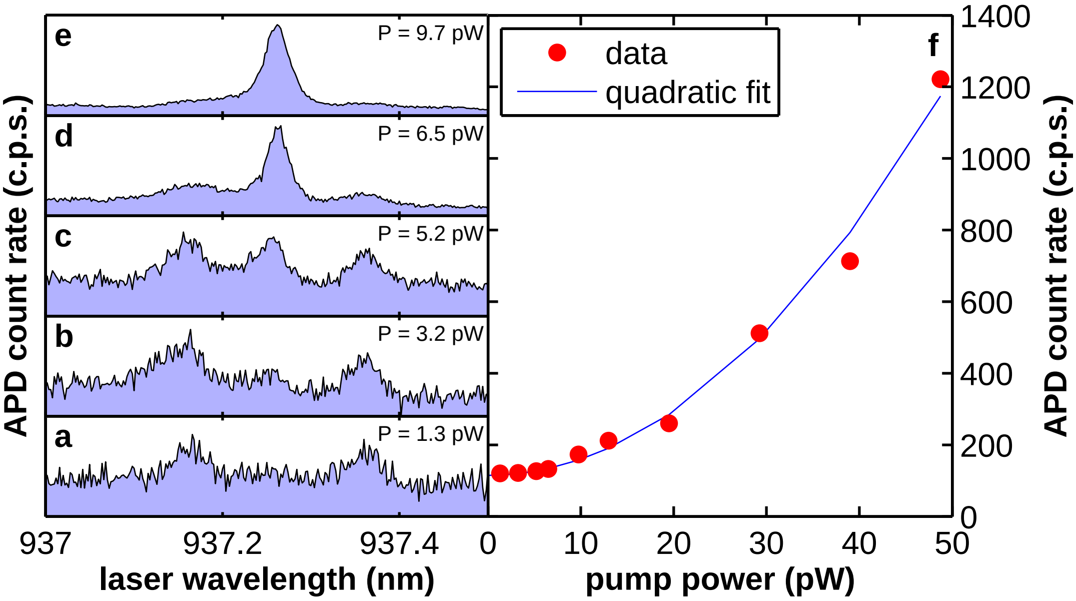

Figure 8.5.: RS power dependence of the uncoupled cavity peak. a-e, RS traces obtained for the pump power indicated in the corresponding tab. Evidently, the central scattering peak increases above the level of the strongly-coupled polariton peaks when the pump power is increased. **f**, Peak height of the central peak as a function of excitation power (red bullets). The blue line shows a quadratic fit to the measured data.

pump power is completely unexpected: when defining saturation of the polaritons as the situation when the average population of the resonantly addressed polariton reaches unity, the resonant saturation power is given by

$$P_{\text{sat}} = \hbar\omega\frac{\kappa+\gamma}{2} \approx \hbar\omega\frac{\kappa}{2\eta}, \tag{8.2}$$

which yields $P_{\text{sat}} = 750$ nW. However, in the experiment presented here, the polariton states saturate at a pump power nearly five orders of magnitude smaller than the theoretical one. Given the low photon population of the cavity field, a nonlinear optical effect seems to be very unlikely to account for the experimental observations. Potentially, however, the quadratic power dependence is related to the dynamics of the charge states the QD is excited to by the probe laser. However, in order to verify this hypothesis, further investigations are required.

8.4. Broadband Resonant Scattering

As mentioned above, one of the main technological limitations for the implementation of the resonant scattering technique arises from the fact that only a limited number of commercially available tunable laser sources provide the mode-hop free tuning range required for those experiments. An alternative method to study resonant scattering spectra is to excite the system with a broadband light source and to

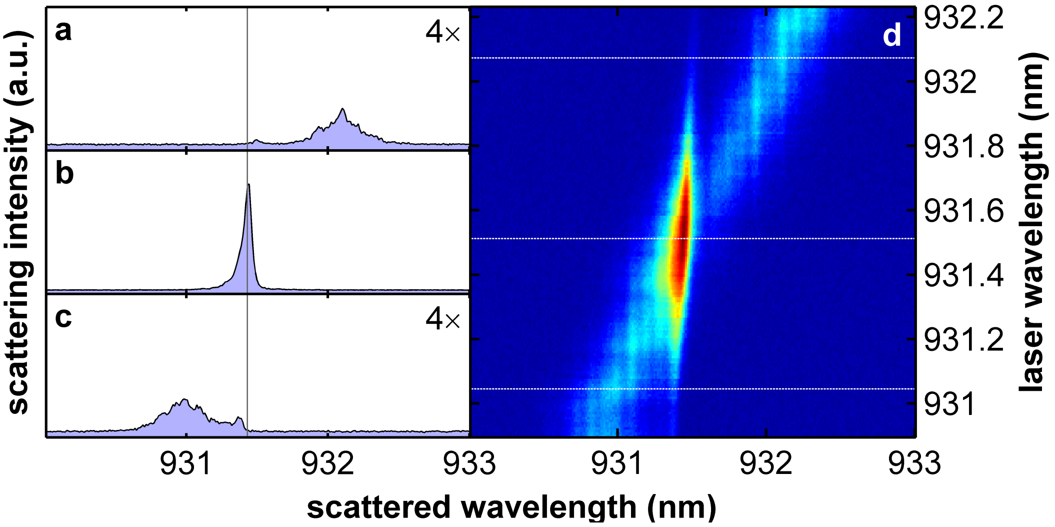

Figure 8.6.: Broadband RS spectra of an L3 cavity in crossed polarization. **a**–**c**, In **a**&**c** the pulse is off-resonant from the cavity mode (the small peak at ~931.4 nm). In **b** the excitation pulse is on resonance with the cavity mode, leading to a strong enhancement of the scattering signal. For better visibility, the vertical scale in **a**&**c** has been offset by a factor of four. **d**, False-color plot of broadband RS spectra (logarithmic color scale). The white dotted lines indicate detunings realized in **a**–**c**. The horizontal modulation on the excitation pulse arises from an etalon effect of the collection optics.

subsequently measure the spectral distribution of the scattered light [129]. We call this method *broadband RS*. In this work, excitation of the system was achieved using a mode-locked titanium-sapphire laser that provides pulses with a duration of ~1 ps that hence exhibit a spectral width of ≈0.4 nm. The laser is focused onto the cavity structure and the back-reflected signal is passed through the crossed polarization setup introduced Sec. 8.2. Finally, the signal is measured in the spectrometer.

Figure 8.6 shows several broadband reflectivity spectra acquired using this technique. In Fig. 8.6a the broad excitation laser pulse is blue detuned from the cavity mode (the small feature at ~ 931.4 nm). When the laser pulse is tuned into resonance, the scattering signal from the cavity mode becomes more pronounced. The scattering signal of the cavity mode is approximately a factor of 13 stronger than the background signal arising from the imperfectly filtered excitation pulse. The slight asymmetry of the cavity mode profile can be attributed to an interference effect arising from a slight misalignment of the analyzer [130] as mentioned above. Finally, in Fig. 8.6c the excitation pulse is tuned further to the red, such that the scattering signal from the cavity mode decreases again. Fig. 8.6d shows several broadband RS spectra obtained when tuning the excitation laser pulse in a false-color plot (logarithmic color scale). The broad diagonal feature corresponds to the excitation laser pulse that is tuned from red to blue detuning in the experiment. The slight horizontal ripple can be attributed to an etalon effect introduced by plane-parallel optical elements in the optical path of the collected signal. The bright feature around 931.4 nm arises from resonant scattering at the cavity mode.

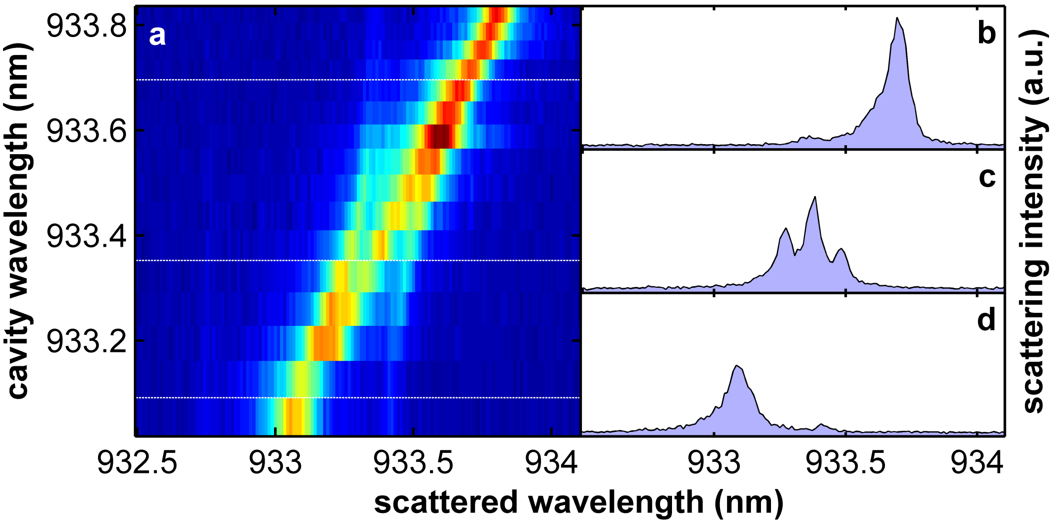

Figure 8.7.: Broadband RS of vacuum Rabi splitting. **a**, False-color plot obtained when scanning the cavity mode across resonance with the X^0 transition of the QD while continuously monitoring broadband RS. The excitation pulse here was moved along with the tuning cavity mode during the experiment. **b**, Cuts through **a** at the cavity mode wavelengths indicated by the dotted horizontal lines.

The feature is slightly tilted, since these measurements were obtained under mode walking conditions, where the cavity mode was subject to a weak wavelength drift as a function of time.

The technique of broadband RS can be straightforwardly applied to the study of vacuum Rabi splitting using the same device as in Sec. 8.3. To this end we recorded broadband RS spectra while tuning the cavity mode across resonance with the X^0 line of the QD using mode walking. The excitation pulse was in this measurement continuously tuned along with the cavity mode. Figure 8.7a shows a series of broadband-reflectivity spectra taken in a false-color plot. Obviously, the data shows qualitatively the same behavior as the results shown in Fig. 8.3: the anticrossing of the polaritons is clearly visible together with an unexpected central peak that arises from the uncoupled cavity mode. Figures 8.7b–d show cuts through Fig. 8.7a at the cavity wavelenghts indicated by the white dotted lines. The vacuum Rabi splitting on resonance can nicely be seen in Fig. 8.7c.

The spectra shown in Fig. 8.7 were obtained at an average pump power of $\approx$5 pW. Due to the pulsed nature of the laser excitation, the peak intensity incident on the structure is certainly significantly larger, giving rise to significant scattering from the uncoupled cavity mode. Investigations of this feature at even lower pump power require exceedingly long integration times, as the signal level collected from the structure then is in the sub-femtowatt regime. This problem is mainly due to the pulse separation of $\approx$ 13 ns of the excitation laser, which is orders of magnitude longer than the decay time of the polaritons $(2(\kappa + \gamma)^{-1})$ on resonance and the ringdown time of the cavity (κ^{-1}). Moving to a smaller duty cycle by increasing the laser repetition rate could provide a means towards the overall increase of the collected signal.

9. Conclusion and Outlook

In conclusion, this dissertation provides a detailed study of cavity-QED systems comprised of single self-assembled quantum dots coupled to photonic-crystal defect microcavities. The technique of active cavity positioning by AFM metrology presented in Chap. 4 allows for the deterministic fabrication of coupled devices in the strong coupling regime that exhibit genuine quantum dynamics. Making use of strong coupling, we study the fine structure of different excitonic states in the QD, thus gaining novel insights into QD physics. Moreover, we unravel the physics behind off-resonant cavity feeding, which is a common feature of all cavity-QED systems based on QDs. Based on detailed experimental and theoretical investigations, we relate this effect to the fundamental mesoscopic nature of the QD confinement itself. In this sense, coupling to a high-Q cavity mode does not only allow us to implement controlled light-emitter coupling at the single photon level, but also enables us to probe the mesoscopic environment of the QD in an unconventional fashion.

This thesis answers many but certainly not all the questions arising from its findings. Quite a few open questions remain and will hopefully stimulate future work. Although the microscopic model of cavity feeding presented in Chap. 7 describes the dynamics for large detunings in great detail, the regime of LA-phonon mediated cavity feeding exhibits a few features that are not yet well understood. On the one hand, we are lacking a quantitative model to predict the modification of the emitter lifetime shown in Fig. 7.17. Moreover, in the regime of strong LA-phonon feeding, we observe rather unexpected photon correlations. In particular, the super-Poissonian statistics observed on the light emitted by the cavity mode in this regime is in complete disagreement with our model of direct cavity feeding from single QD excitons. At this point, it is not even clear, whether this observation arises from the nature of phonon coupling itself or from the subtle interplay between the two cavity feeding mechanisms.

Recent work suggested the occurrence of lasing in microcavity structures containing QDs [75]. Naturally, our findings on cavity feeding are expected to have strong impact on the understanding of the gain mechanisms provided by an ensemble of QDs. In fact, even lasing from single-QD structures could in principle be envisioned.

As preliminary measurements done on one of our devices have shown linewidth narrowing together with a change of the quantum statistics of the emitted light, the question arises whether stimulated emission plays a significant role in this regime.

Other effects related to cavity feeding still lack an explanation. Here, we mention "cavity draining" and the occurrence of the third peak in PL, which is a feature exclusively observed in our group. The understanding of its occurrence, or its absence in other systems is clearly desirable.

A key problem that has to be addressed in the context of resonant spectroscopy is the observation of a nonlinearity of the uncoupled cavity mode at the level of picowatt optical powers (Sec. 8.3). The mechanism giving rise to an uncoupled cavity peak despite being in the vacuum-Rabi split regime (Fig. 8.3 and Fig. 8.7) again promises to unveil fundamental properties of self-assembled QDs. Moreover, several key quantum optical experiments can potentially be conducted using resonant spectroscopy.

One key demonstration would be the direct probing of the anharmonicity of the Jaynes-Cummings ladder. While the quantum nature of our strongly coupled devices was shown in Sec. 5.3, this experiment only provides indirect proof for the anharmonic structure of the coupled atom-photon system. A direct observation could be achieved by the use of a two-color resonant probing scheme, along the lines of similar experiments conducted on superconducting cavity-QED devices in the microwave range [131]. Such an experiment would complement nicely the photon-blockade effect [111] observed both in atomic [8, 9] and QD-based systems [132].

A technological limitation for resonant scattering spectroscopy is given by the low efficiency of free-space coupling between the cavity field and an incident laser beam. There are two alternative routes to overcome this problem. On the one hand, advanced cavity designs aimed at more directional emission from the cavity mode (at the expense of Q) could lead to stronger laser-cavity coupling in free-space approaches. Preliminary experiments along these line have been reported in Ref. [133]. On the other hand, near-field coupling to the cavity can be achieved by a fiber-taper waveguide and can yield significantly better coupling efficiencies to microcavities [134]. Strong coupling in such a system was reported in Ref. [108].

Finally, more advanced sample designs that combine photonic crystal cavities with electrical gates [40, 83, 104] promise the combination of cavity QED with spin physics [18]. This would open the route towards the implementation of quantum nondemolition measurements [135] of the electron spin or, more generally, quantum computation with spins in cavities [5].

A. Optical Setup

This section describes in detail the optical setup used for both PL and RS measurements presented in this thesis. Figure A.1 shows a schematic setup of the system. The list given below describes the optical elements used following the beam-line from the output couplers of the excitation lasers to the input fiber coupler of the collection arm.

- **F1, F2**: Two optical fibers (Thorlabs P3-980A-FC-5 and P3-830A-FC-5) for coupling laser light at ∼940 nm (1) and ∼800 nm (2).

- **FC1, FC2**: Two output fiber couplers for PL and RS measurements using aspheric lenses (Thorlabs C280TME-B, $f = 18.40$ mm) and a z axis translation stage that allows for focus adjustment by changing the distance between the fiber tip and the lens.

- **P1, P2**: Glan-laser polarizers (Newport 10GL08AR.16) for fixing the polarization of the excitation light to the plane perpendicular to the table (vertical polarization).

- **B1, B2**: 90:10 beamsamplers (Newport 10B20NC.2) for each arm that reflect 10% (for vertical polarization) of the light towards the sample via Fresnel reflection. For horizontal polarization the splitting ratio is 99:1.

- **D1, D2**: The transmitted signal is measured using switchable-gain amplified photodetectors (Thorlabs PDA10A-EC) for active intensity stabilization and modulation.

- **OD1, OD2**: Exchangeable absorptive neutral optical-density filters to attenuate the lasers after the pick-off for intensity stabilization.

- **M1**: Steering mirror for the PL laser (Newport 10D20BD.2).

- **L1**: Focusing lens (Thorlabs LE1830-C with $f = 200$ mm) for defocusing the PL excitation laser on the sample surface. This allows for wide-field illumination of the sample for obtaining PL micrographs.

- **B3**: 50:50 beamsplitter (Thorlabs BSW08) for superimposing the two excitation arms. Each arm can be steered independently.

- **B4**: 90:10 beamsampler (Newport 10B20NC.2) directing the total excitation light to the sample.

- **D3**: The transmitted signal is monitored on an optical powermeter (Newport 1830-C) in order to estimate the laser power incident on the sample.

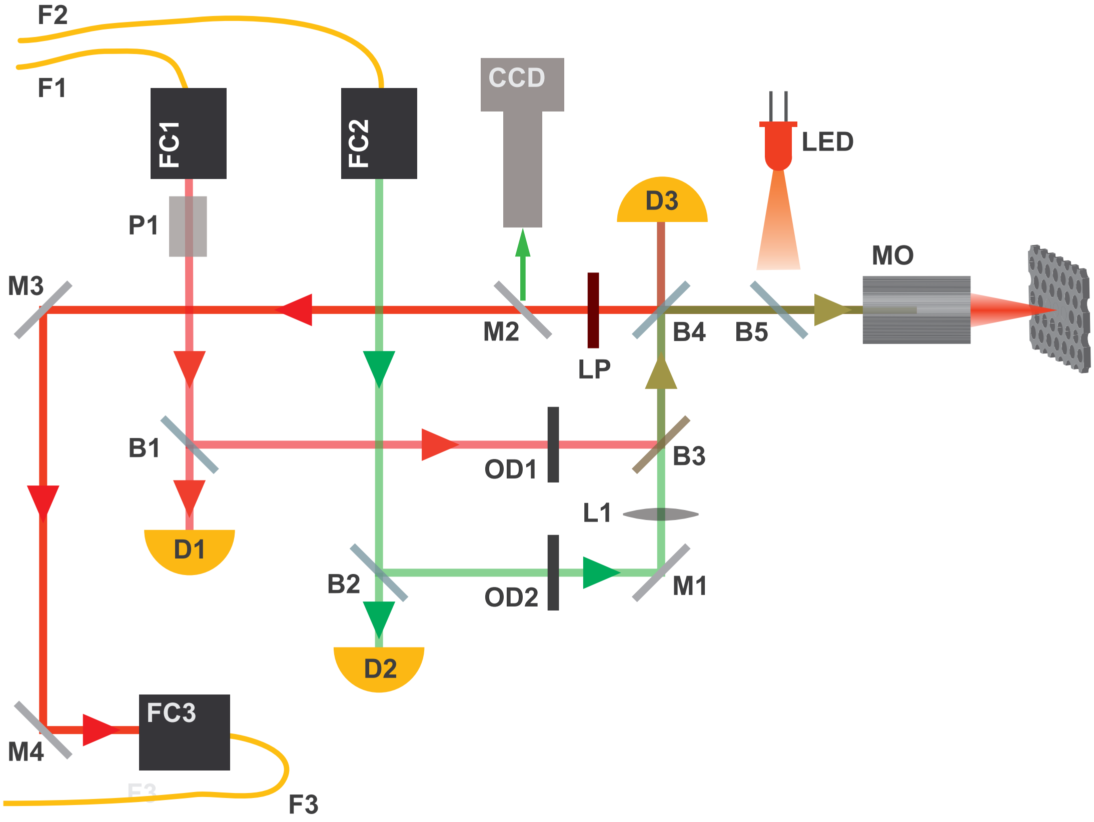
F2
F1
FC1
FC2
CCD
LED
P1
D3
MO
M3
M2
LP
B4
B5
B1
OD1
B3
L1
D1
B2
OD2
M1
D2
FC3
M4
F3
F3

Figure A.1.: Schematic of the confocal microscope setup. Details of the elements are given in the text.

- **B5**: 90:10 beamsplitter (Newport 10B20NC.2) that couples light from the LED (centered at $\lambda = 940$ nm) to the sample for illumination in wide-field imaging.

- **MO**: 50× ($f = 4$ mm), NA = 0.55 microscope objective (Nikon CF Plan 50X CR, EPI) which corrects for imaging errors introduced by the 0.7 mm thick cryostat window. The microscope objective is mounted on a z translation stage equipped with a piezo actuator.

- **LP**: Longpass filter (Thorlabs FEL0900, transmitting for $\lambda > 900$ nm) to suppress the back-reflected excitation laser.

- **M2**: A flip mirror for directing the image to the camera unit for imaging the sample surface.

- **CCD**: CCD camera (Watec 120N) with adjustable integration time, focused to infinity by an $f = 200$ nm best-form lens (Thorlabs LBF254-200-B).

- **M3, M4**: Two silver mirrors (Thorlabs P01) steering the collected light to the collection fiber coupler FC3.

- **FC3**: A fiber coupler analogous to the output couplers F1&F2 couples the collected light from the sample into a single-mode fiber (Thorlabs P3-980A-FC-5). Again, we use a $f = 18.4$ mm lens for focusing the signal onto the fiber tip. The ratio of the focal lengths of 18.4/4 between the focusing lens and the microscope objective roughly matches the ratio of the NAs of the microscope objective (NA = 0.55) and the single mode fiber (NA = 0.14).

Laser Sources Dependent on the specific application, we make use of several laser sources:

- The main excitation laser for our PL measurements is a MIRA™900 titanium:sapphire laser. The nominal operation wavelength covers a range of 750–1000 nm, easily tunable by a birefringent filter. Being designed for mode-locked operation, the MIRA™does not provide a single emission frequency in CW mode, but rather lases in a few longitudinal modes, with the intensity distribution among them fluctuating. However, this issue does not have significant relevance for the off-resonant excitation of a semiconductor sample. The MIRA™can be mode-locked in picosecond mode, in order to provide a continuous train of pulses of ~ 1 ps duration at a repetition rate of $f_0 = 76$ MHz.

- As an easy alternative for PL excitation, we occasionally use a free-running laser diode at $\lambda = 780$ nm.

- As an alternative for pulsed PL excitation for TCSPC measurements, a pulsed laser diode from PicoQuant GmbH. is available that is centered at $\lambda = 780$ nm and has a variable repetition rate from 5 MHz to 80 MHz.

- For resonant scattering we use an external-cavity diode-laser system in the Littmann-Metcalf configuration (NewFocus TLB-6319 Velocity™). This laser provides mode-hop free tuning over the entire operating wavelength range between 930–946 nm.

All lasers are coupled to single-mode fibers.

Active laser-power stabilization As most laser sources are subject to intensity noise that can further be enhanced within the optical setup, e.g. by acoustic or mechanical noise, a feedback system actively controls the laser power. This also allows for the computerized control of the laser power.

Modulation of the laser intensities was achieved by passing the laser through an acousto-optical modulator (AOM) in a double-pass configuration. After the AOM, the beam is directed to the microscope by a single-mode fiber. The AOM together with a home-built PID controller and the monitoring photodetectors D1&D2 constitute a servo loop for stabilizing the laser power.

Bibliography

[1] D. F. Walls and G. J. Milburn, *Quantum Optics* (Springer-Verlag, Berlin Heidelberg, 2007). 1

[2] H. Mabuchi and A. C. Doherty, *Cavity Quantum Electrodynamics: Coherence in Context*, Science **298**, 1372 (2002).

[3] J. M. Raimond, M. Brune, and S. Haroche, *Manipulating quantum entanglement with atoms and photons in a cavity*, Reviews of Modern Physics **73**, 565 (2001). 1

[4] T. Wilk, S. C. Webster, A. Kuhn, and G. Rempe, *Single-Atom Single-Photon Quantum Interface*, Science **317**, 488 (2007). 1

[5] A. Imamoglu, D. D. Awschalom, G. Burkard, D. P. DiVincenzo, D. Loss, M. Sherwin, and A. Small, *Quantum information processing using quantum dot spins and cavity QED*, Physical Review Letters **83**, 4204 (1999). 1, 110

[6] S. Gleyzes, S. Kuhr, C. Guerlin, J. Bernu, S. Deleglise, U. Busk Hoff, M. Brune, J.-M. Raimond, and S. Haroche, *Quantum jumps of light recording the birth and death of a photon in a cavity*, Nature **446**, 297 (2007). 1

[7] C. J. Hood, T. W. Lynn, A. C. Doherty, A. S. Parkins, and H. J. Kimble, *The Atom-Cavity Microscope: Single Atoms Bound in Orbit by Single Photons*, Science **287**, 1447 (2000). 2

[8] K. M. Birnbaum, A. Boca, R. Miller, A. D. Boozer, T. E. Northup, and H. J. Kimble, *Photon blockade in an optical cavity with one trapped atom*, Nature **436**, 87 (2005). 110

[9] B. Dayan, A. S. Parkins, T. Aoki, E. P. Ostby, K. J. Vahala, and H. J. Kimble, *A Photon Turnstile Dynamically Regulated by One Atom*, Science **319**, 1062 (2008). 2, 110

[10] F. Brennecke, T. Donner, S. Ritter, T. Bourdel, M. Kohl, and T. Esslinger, *Cavity QED with a Bose-Einstein condensate*, Nature **450**, 268 (2007). 2

[11] A. Wallraff, D. I. Schuster, A. Blais, L. Frunzio, R. S. Huang, J. Majer, S. Kumar, S. M. Girvin, and R. J. Schoelkopf, *Strong coupling of a single photon to a superconducting qubit using circuit quantum electrodynamics*, Nature **431**, 162 (2004). 2

[12] A. Blais, R.-S. Huang, A. Wallraff, S. M. Girvin, and R. J. Schoelkopf, *Cavity quantum electrodynamics for superconducting electrical circuits: An architecture for quantum computation*, Physical Review A **69**, 062320 (2004). 2

[13] P. Michler, A. Imamoglu, M. D. Mason, P. J. Carson, G. F. Strouse, and S. K. Buratto, *Quantum correlation among photons from a single quantum dot at room temperature*, Nature **406**, 968 (2000). 2

[14] C. Santori, D. Fattal, J. Vuckovic, G. S. Solomon, and Y. Yamamoto, *Indistinguishable photons from a single-photon device*, Nature **419**, 594 (2002). 2

[15] A. Zrenner, E. Beham, S. Stufler, F. Findeis, M. Bichler, and G. Abstreiter, *Coherent properties of a two-level system based on a quantum-dot photodiode*, Nature **418**, 612 (2002). 2

[16] X. Li, Y. Wu, D. Steel, D. Gammon, T. H. Stievater, D. S. Katzer, D. Park, C. Piermarocchi, and L. J. Sham, *An All-Optical Quantum Gate in a Semiconductor Quantum Dot*, Science **301**, 809 (2003). 2

[17] R. J. Warburton, C. Schaflein, D. Haft, F. Bickel, A. Lorke, K. Karrai, J. M. Garcia, W. Schoenfeld, and P. M. Petroff, *Optical emission from a charge-tunable quantum ring*, Nature **405**, 926 (2000). 2, 18

[18] M. Atature, J. Dreiser, A. Badolato, A. Hogele, K. Karrai, and A. Imamoglu, *Quantum-Dot Spin-State Preparation with Near-Unity Fidelity*, Science **312**, 551 (2006). 2, 15, 18, 110

[19] M. Atature, J. Dreiser, A. Badolato, and A. Imamoglu, *Observation of Faraday rotation from a single confined spin*, Nature Physics **3**, 101 (2007). 2, 18

[20] B. D. Gerardot, D. Brunner, P. A. Dalgarno, P. Ohberg, S. Seidl, M. Kroner, K. Karrai, N. G. Stoltz, P. M. Petroff, and R. J. Warburton, *Optical pumping of a single hole spin in a quantum dot*, Nature **451**, 441 (2008). 2

[21] D. Brunner, B. D. Gerardot, P. A. Dalgarno, G. Wust, K. Karrai, N. G. Stoltz, P. M. Petroff, and R. J. Warburton, *A Coherent Single-Hole Spin in a Semiconductor*, Science **325**, 70 (2009). 2

[22] A. V. Khaetskii and Y. V. Nazarov, *Spin relaxation in semiconductor quantum dots*, Physical Review B **61**, 12639 (2000). 2

[23] D. Press, T. D. Ladd, B. Zhang, and Y. Yamamoto, *Complete quantum control of a single quantum dot spin using ultrafast optical pulses*, Nature **456**, 218 (2008). 2, 18

[24] T. Steinmetz, Y. Colombe, D. Hunger, T. W. Hansch, A. Balocchi, R. J. Warburton, and J. Reichel, *Stable fiber-based Fabry-Perot cavity*, Applied Physics Letters **89**, 111110 (2006). 2

[25] M. Fujita, S. Takahashi, Y. Tanaka, T. Asano, and S. Noda, *Simultaneous inhibition and redistribution of spontaneous light emission in photonic crystals*, Science **308**, 1296 (2005). 2

[26] A. Badolato, K. Hennessy, M. Atature, J. Dreiser, E. Hu, P. M. Petroff, and A. Imamoglu, *Deterministic Coupling of Single Quantum Dots to Single Nanocavity Modes*, Science **308**, 1158 (2005). 20, 40, 41, 46, 53

[27] S. Noda, M. Fujita, and T. Asano, *Spontaneous-emission control by photonic crystals and nanocavities*, Nature Photonics **1**, 449 (2007). 2

[28] T. Yoshie, A. Scherer, J. Hendrickson, G. Khitrova, H. M. Gibbs, G. Rupper, C. Ell, O. B. Shchekin, and D. G. Deppe, *Vacuum Rabi splitting with a single quantum dot in a photonic crystal nanocavity*, Nature **432**, 200 (2004). 2, 20, 40, 45, 53, 61

[29] J. P. Reithmaier, G. Sek, A. Loffler, C. Hofmann, S. Kuhn, S. Reitzenstein, L. V. Keldysh, V. D. Kulakovskii, T. L. Reinecke, and A. Forchel, *Strong coupling in a single quantum dot-semiconductor microcavity system*, Nature **432**, 197 (2004). 19, 45

[30] E. Peter, P. Senellart, D. Martrou, A. Lemaitre, J. Hours, J. M. Gerard, and J. Bloch, *Exciton-photon strong-coupling regime for a single quantum dot embedded in a microcavity*, Physical Review Letters **95** (2005). 2, 19, 40, 53, 61

[31] B.-S. Song, S. Noda, T. Asano, and Y. Akahane, *Ultra-high-Q photonic double-heterostructure nanocavity*, Nature Materials **4**, 207 (2005). 2, 20

[32] K. Hennessy, A. Badolato, A. Tamboli, P. M. Petroff, E. Hu, M. Atature, J. Dreiser, and A. Imamoglu, *Tuning photonic crystal nanocavity modes by wet chemical digital etching*, Applied Physics Letters **87**, 021108 (2005). 2, 46, 47

[33] K. Hennessy, C. Hogerle, E. Hu, A. Badolato, and A. Imamoglu, *Tuning photonic nanocavities by atomic force microscope nano-oxidation*, Applied Physics Letters **89**, 041118 (2006).

[34] S. Strauf, M. T. Rakher, I. Carmeli, K. Hennessy, C. Meier, A. Badolato, M. J. A. DeDood, P. M. Petroff, E. L. Hu, E. G. Gwinn, et al., *Frequency control of photonic crystal membrane resonators by monolayer deposition*, Applied Physics Letters **88**, 043116 (2006). 47

[35] S. Mosor, J. Hendrickson, B. C. Richards, J. Sweet, G. Khitrova, H. M. Gibbs, T. Yoshie, A. Scherer, O. B. Shchekin, and D. G. Deppe, *Scanning a photonic crystal slab nanocavity by condensation of xenon*, Applied Physics Letters **87**, 141105 (2005). 2, 47

[36] R. Loudon, *The Quantum Theory of Light* (Oxford Science Publications, 2000). 6, 31

[37] Y. Yamamoto and A. Imamoglu, *Mesoscopic Quantum Optics* (Wiley & Sons, 1999). 6

[38] J.-M. Gerard and B. Gayral, in *Confined Photon Systems*, edited by H. Benisty, J.-M. Gerard, R. Houdre, J. Rarity, and C. Weisbuch (Springer-Verlag, Berlin Heidelberg, 1998). 6, 9

[39] E. T. Jaynes and F. W. Cummings, *Comparison of quantum and semiclassical radiation theories with application to the beam maser*, Proceedings of the IEEE **51**, 89 (1963). 6

[40] A. Laucht, N. Hauke, J. M. Villas-Boas, F. Hofbauer, M. Kaniber, G. Bohm, and J. J. Finley, *Dephasing of quantum dot exciton polaritons in electrically tunable nanocavities*, arXiv:cond-mat/0904.4759 (2009). 9, 110

[41] L. C. Andreani, G. Panzarini, and J.-M. Gerard, *Strong-coupling regime for quantum boxes in pillar microcavities: Theory*, Physical Review B **60**, 13276 (1999). 9

[42] M. O. Scully and M. S. Zubairy, *Quantum Optics* (Cambridge University Press, 1997). 9

[43] D. Englund, D. Fattal, E. Waks, G. Solomon, B. Zhang, T. Nakaoka, Y. Arakawa, Y. Yamamoto, and J. Vuckovic, *Controlling the spontaneous emission rate of single quantum dots in a two-dimensional photonic crystal*, Physical Review Letters **95** (2005). 9, 56, 61

[44] S. M. Tan, *A computational toolbox for quantum and atomic optics*, Journal of Optics B: Quantum and Semiclassical Optics **1**, 424 (1999). 10

[45] P. Michler, A. Kiraz, C. Becher, W. V. Schoenfeld, P. M. Petroff, L. D. Zhang, E. Hu, and A. Imamoglu, *A quantum dot single-photon turnstile device*, Science **290**, 2282 (2000). 11, 32

[46] I. N. Stranski and L. Von Krastanow, Abhandlungen der Mathematisch-Naturwissenschaftlichen Klasse **146**, 797 (1939). 11

[47] D. Leonard, M. Krishnamurthy, C. M. Reaves, S. P. Denbaars, and P. M. Petroff, *Direct formation of quantum-sized dots from uniform coherent islands of InGaAs on GaAs surfaces*, Applied Physics Letters **63**, 3203 (1993). 11

[48] S. Fält, Ph.D. thesis, ETH Zürich (2007). 12

[49] J. M. Garcia, T. Mankad, P. O. Holtz, P. J. Wellman, and P. M. Petroff, *Electronic states tuning of InAs self-assembled quantum dots*, Applied Physics Letters **72**, 3172 (1998). 12

[50] J. M. Luttinger, *Quantum Theory of Cyclotron Resonance in Semiconductors - General Theory*, Physical Review **102**, 1030 (1956). 14

[51] M. Bayer, G. Ortner, O. Stern, A. Kuther, A. A. Gorbunov, A. Forchel, P. Hawrylak, S. Fafard, K. Hinzer, T. L. Reinecke, et al., *Fine structure of neutral and charged excitons in self-assembled In(Ga)As/(Al)GaAs quantum dots*, Physical Review B **65**, 195315 (2002). 16

[52] R. J. Young, R. M. Stevenson, A. J. Shields, P. Atkinson, K. Cooper, D. A. Ritchie, K. M. Groom, A. I. Tartakovskii, and M. S. Skolnick, *Inversion of exciton level splitting in quantum dots*, Physical Review B **72**, 113305 (2005). 17

[53] O. Stier, M. Grundmann, and D. Bimberg, *Electronic and optical properties of strained quantum dots modeled by 8-band kp theory*, Physical Review B **59**, 5688 (1999). 17

[54] R. M. Stevenson, R. J. Young, P. See, D. G. Gevaux, K. Cooper, P. Atkinson, I. Farrer, D. A. Ritchie, and A. J. Shields, *Magnetic-field-induced reduction of the exciton polarization splitting in InAs quantum dots*, Physical Review B **73**, 033306 (2006). 17

[55] O. Benson, C. Santori, M. Pelton, and Y. Yamamoto, *Regulated and Entangled Photons from a Single Quantum Dot*, Physical Review Letters **84**, 2513 (2000). 17

[56] T. M. Stace, G. J. Milburn, and C. H. W. Barnes, *Entangled two-photon source using biexciton emission of an asymmetric quantum dot in a cavity*, Physical Review B **67** (2003). 17

[57] N. Akopian, N. H. Lindner, E. Poem, Y. Berlatzky, J. Avron, D. Gershoni, B. D. Gerardot, and P. M. Petroff, *Entangled Photon Pairs from Semiconductor Quantum Dots*, Physical Review Letters **96**, 130501 (2006). 17

[58] R. M. Stevenson, R. J. Young, P. Atkinson, K. Cooper, D. A. Ritchie, and A. J. Shields, *A semiconductor source of triggered entangled photon pairs*, Nature **439**, 179 (2006). 17, 67

[59] A. Hogele, B. Alen, F. Bickel, R. J. Warburton, P. M. Petroff, and K. Karrai, *Exciton fine structure splitting of Single InGaAs self-assembled quantum dots*, Physica E-Low-Dimensional Systems & Nanostructures **21**, 175 (2004). 18, 98

[60] A. Hogele, S. Seidl, M. Kroner, K. Karrai, R. J. Warburton, B. D. Gerardot, and P. M. Petroff, *Voltage-Controlled Optics of a Quantum Dot*, Physical Review Letters **93**, 217401 (2004). 18

[61] M. Ediger, P. A. Dalgarno, J. M. Smith, B. D. Gerardot, R. J. Warburton, K. Karrai, and P. M. Petroff, *Controlled generation of neutral, negatively-charged and positively-charged excitons in the same single quantum dot*, Applied Physics Letters **86**, 211909 (2005). 18, 28

[62] B. Urbaszek, R. J. Warburton, K. Karrai, B. D. Gerardot, P. M. Petroff, and J. M. Garcia, *Fine Structure of Highly Charged Excitons in Semiconductor Quantum Dots*, Physical Review Letters **90**, 247403 (2003). 18, 67

[63] K. J. Vahala, *Optical microcavities*, Nature **424**, 839 (2003). 19

[64] G. Khitrova, H. M. Gibbs, M. Kira, S. W. Koch, and A. Scherer, *Vacuum Rabi splitting in semiconductors*, Nature Physics **2**, 81 (2006). 19

[65] K. Hennessy, Ph.D. thesis, University of California Santa Barbara (2006). 19, 20, 21, 22, 41, 44, 53, 98

[66] A. Loffler, J. P. Reithmaier, G. Sek, C. Hofmann, S. Reitzenstein, M. Kamp, and A. Forchel, *Semiconductor quantum dot microcavity pillars with high-quality factors and enlarged dot dimensions*, Applied Physics Letters **86**, 111105 (2005). 19

[67] D. Press, S. Gotzinger, S. Reitzenstein, C. Hofmann, A. Loffler, M. Kamp, A. Forchel, and Y. Yamamoto, *Photon Antibunching from a Single Quantum-Dot-Microcavity System in the Strong Coupling Regime*, Physical Review Letters **98**, 117402 (2007). 19, 61

[68] A. E. Bate, *Note on the whispering gallery of St Paul's Cathedral, London*, Proceedings of the Physical Society **50**, 293 (1938). 19

[69] C. V. Raman and G. A. Sutherland, *On the Whispering-Gallery Phenomenon*, Proceedings of the Royal Society of London. Series A **100**, 424 (1922). 19

[70] B. Gayral, J. M. Gerard, A. Lemaitre, C. Dupuis, L. Manin, and J. L. Pelouard, *High-Q wet-etched GaAs microdisks containing InAs quantum boxes*, Applied Physics Letters **75**, 1908 (1999). 19

[71] P. Vukusic and J. R. Sambles, *Photonic structures in biology*, Nature **424**, 852 (2003). 20

[72] S. John, *Strong localization of photons in certain disordered dielectric superlattices*, Physical Review Letters **58**, 2486 (1987). 20

[73] E. Yablonovitch, *Inhibited Spontaneous Emission in Solid-State Physics and Electronics*, Physical Review Letters **58**, 2059 (1987). 20

[74] O. Painter, R. K. Lee, A. Scherer, A. Yariv, J. D. O'Brien, P. D. Dapkus, and I. Kim, *Two-Dimensional Photonic Band-Gap Defect Mode Laser*, Science **284**, 1819 (1999). 20, 22

[75] S. Strauf, K. Hennessy, M. T. Rakher, Y. S. Choi, A. Badolato, L. C. Andreani, E. L. Hu, P. M. Petroff, and D. Bouwmeester, *Self-Tuned Quantum Dot Gain in Photonic Crystal Lasers*, Physical Review Letters **96**, 127404 (2006). 40, 61, 88, 109

[76] T. Yoshie, O. B. Shchekin, H. Chen, D. G. Deppe, and A. Scherer, *Quantum dot photonic crystal lasers*, Electronics Letters **38**, 967 (2002).

[77] H. Altug, D. Englund, and J. Vuckovic, *Ultrafast photonic crystal nanocavity laser*, Nature Physics **2**, 484 (2006). 20

[78] M. Notomi, A. Shinya, S. Mitsugi, G. Kira, E. Kuramochi, and T. Tanabe, *Optical bistable switching action of Si high-Q photonic-crystal nanocavities*, Optics Express **13**, 2678 (2005). 20

[79] T. Tanabe, M. Notomi, S. Mitsugi, A. Shinya, and E. Kuramochi, *All-optical switches on a silicon chip realized using photonic crystal nanocavities*, Applied Physics Letters **87**, 151112 (2005). 20

[80] Y. Akahane, T. Asano, B.-S. Song, and S. Noda, *Investigation of high-Q channel drop filters using donor-type defects in two-dimensional photonic crystal slabs*, Applied Physics Letters **83**, 1512 (2003). 20

[81] K. Hennessy, A. Badolato, M. Winger, D. Gerace, M. Atature, S. Gulde, S. Falt, E. L. Hu, and A. Imamoglu, *Quantum nature of a strongly coupled single quantum dot-cavity system*, Nature **445**, 896 (2007). 20, 48, 51, 71, 84, 86, 88

[82] D. Englund, A. Faraon, I. Fushman, N. Stoltz, P. Petroff, and J. Vuckovic, *Controlling cavity reflectivity with a single quantum dot*, Nature **450**, 857 (2007). 40, 45, 61, 100

[83] A. Laucht, F. Hofbauer, N. Hauke, J. Angele, S. Stobbe, M. Kaniber, G. Bohm, P. Lodahl, M. C. Amann, and J. J. Finley, *Electrical control of spontaneous emission and strong coupling for a single quantum dot*, New Journal of Physics **11**, 023034 (2009). 20, 46, 98, 110

[84] J. D. Joannopoulos, R. D. Meade, and J. N. Winn, *Photonic Crystals* (Princeton University Press, 1995). 20

[85] S. Noda, A. Chutinan, and M. Imada, *Trapping and emission of photons by a single defect in a photonic bandgap structure*, Nature **407**, 608 (2000). 21

[86] Y. Akahane, T. Asano, B.-S. Song, and S. Noda, *High-Q photonic nanocavity in a two-dimensional photonic crystal*, Nature **425**, 944 (2003). 21, 22, 51

[87] L. C. Andreani, *Photonic Bands and Radiation Losses in Photonic Crystal Waveguides*, physica status solidi (b) **234**, 139 (2002). 22

[88] L. C. Andreani and M. Agio, *Photonic bands and gap maps in a photonic crystal slab*, IEEE Journal of Quantum Electronics **38**, 891 (2002). 22

[89] K. Yee, *Numerical solution of inital boundary value problems involving maxwell's equations in isotropic media*, IEEE Transactions on Antennas and Propagation **14**, 302 (1966). 22

[90] J. Vuckovic, M. Loncar, H. Mabuchi, and A. Scherer, *Design of photonic crystal microcavities for cavity QED*, Physical Review E **65** (2002). 22

[91] J. Vuckovic, M. Loncar, H. Mabuchi, and A. Scherer, *Optimization of the Q factor in photonic crystal microcavities*, IEEE Journal of Quantum Electronics **38**, 850 (2002). 22

[92] C. P. Michael, K. Srinivasan, T. J. Johnson, O. Painter, K. H. Lee, K. Hennessy, H. Kim, and E. Hu, *Wavelength- and material-dependent absorption in GaAs and AlGaAs microcavities*, Applied Physics Letters **90**, 051108 (2007). 23

[93] W. H. Chang, H. S. Chang, W. Y. Chen, T. M. Hsu, T. P. Hsieh, J. I. Chyi, and N. T. Yeh, *Optical control of the exciton charge states of single quantum dots via impurity levels*, Physical Review B **72**, 233302 (2005). 27

[94] X.-Q. Li, H. Nakayama, and Y. Arakawa, *Phonon bottleneck in quantum dots: Role of lifetime of the confined optical phonons*, Physical Review B **59**, 5069 (1999). 27

[95] E. A. Zibik, L. R. Wilson, R. P. Green, G. Bastard, R. Ferreira, P. J. Phillips, D. A. Carder, J. P. R. Wells, J. W. Cockburn, M. S. Skolnick, et al., *Intraband relaxation via polaron decay in InAs self-assembled quantum dots*, Physical Review B **70**, 161305 (2004). 27

[96] T. Grange, R. Ferreira, and G. Bastard, *Polaron relaxation in self-assembled quantum dots: Breakdown of the semiclassical model*, Physical Review B **76**, 241304 (2007). 27

[97] H. J. Kimble, M. Dagenais, and L. Mandel, *Photon Anti-Bunching in Resonance Fluorescence*, Physical Review Letters **39**, 691 (1977). 32

[98] E. Moreau, I. Robert, L. Manin, V. Thierry-Mieg, J. M. Grard, and I. Abram, *Quantum Cascade of Photons in Semiconductor Quantum Dots*, Physical Review Letters **87**, 183601 (2001). 33

[99] A. Badolato, Ph.D. thesis, University of California Santa Barbara (2005). 39

[100] M. Kaniber, A. Laucht, A. Neumann, J. M. Villas-Boas, M. Bichler, M. C. Amann, and J. J. Finley, *Investigation of the nonresonant dot-cavity coupling in two-dimensional photonic crystal nanocavities*, Physical Review B **77**, 161303 (2008). 40, 53, 61, 74, 84

[101] K. Hennessy, A. Badolato, P. M. Petroff, and E. Hu, *Positioning photonic crystal cavities to single InAs quantum dots*, Photonics and Nanostructures - Fundamentals and Applications **2**, 65 (2004). 40, 44

[102] Q. Xie, A. Madhukar, P. Chen, and N. P. Kobayashi, *Vertically Self-Organized InAs Quantum Box Islands on GaAs(100)*, Physical Review Letters **75**, 2542 (1995). 40

[103] G. S. Solomon, J. A. Trezza, A. F. Marshall, and J. J. S. Harris, *Vertically Aligned and Electronically Coupled Growth Induced InAs Islands in GaAs*, Physical Review Letters **76**, 952 (1996). 40

[104] F. Hofbauer, S. Grimminger, J. Angele, G. Bohm, R. Meyer, M. C. Amann, and J. J. Finley, *Electrically probing photonic bandgap phenomena in contacted defect nanocavities*, Applied Physics Letters **91**, 201111 (2007). 46, 98, 110

[105] K. Srinivasan and O. Painter, *Mode coupling and cavity-quantum-dot interactions in a fiber-coupled microdisk cavity*, Physical Review A **75** (2007). 47

[106] K. Srinivasan and O. Painter, *Optical fiber taper coupling and high-resolution wavelength tuning of microdisk resonators at cryogenic temperatures*, Applied Physics Letters **90**, 031114 (2007). 48, 98

[107] M. Winger, A. Badolato, K. J. Hennessy, E. L. Hu, and A. Imamoglu, *Quantum Dot Spectroscopy Using Cavity Quantum Electrodynamics*, Physical Review Letters **101**, 226808 (2008). 48, 61

[108] K. Srinivasan and O. Painter, *Linear and nonlinear optical spectroscopy of a strongly coupled microdisk-quantum dot system*, Nature **450**, 862 (2007). 53, 61, 98, 110

[109] J. J. Childs, K. An, M. S. Otteson, R. R. Dasari, and M. S. Feld, *Normal-Mode Line Shapes for Atoms in Standing-Wave Optical Resonators*, Physical Review Letters **77**, 2901 (1996). 55

[110] V. Savona, L. C. Andreani, P. Schwendimann, and A. Quattropani, *Quantum well excitons in semiconductor microcavities: Unified treatment of weak and strong coupling regimes*, Solid State Communications **93**, 733 (1995). 57

[111] A. Imamoglu, H. Schmidt, G. Woods, and M. Deutsch, *Strongly Interacting Photons in a Nonlinear Cavity*, Physical Review Letters **79**, 1467 (1997). 57, 110

[112] I. A. Merkulov, A. L. Efros, and M. Rosen, *Electron spin relaxation by nuclei in semiconductor quantum dots*, Physical Review B **65**, 205309 (2002). 67

[113] S. Seidl, B. D. Gerardot, P. A. Dalgarno, K. Kowalik, A. W. Holleitner, P. M. Petroff, K. Karrai, and R. J. Warburton, *Statistics of quantum dot exciton fine structure splittings and their polarization orientations*, Physica E: Low-dimensional Systems and Nanostructures **40**, 2153 (2008). 68

[114] M. Winger, T. Volz, G. Tarel, S. Portolan, A. Badolato, K. Hennessy, E. Hu, A. Beveratos, J. Finley, V. Savona, et al., *Mesoscopic cavity-QED: The physics behind off-resonant cavity excitation by a single quantum dot*, arXiv:cond-mat/0907.1881 (2009). 71

[115] M. Yamaguchi, T. Asano, M. Fujita, and S. Noda, *Theoretical analysis of light emission from a coupled system of a photonic nanocavity and a quantum dot*, physica status solidi (c) **5**, 2828 (2008). 76

[116] M. Yamaguchi, T. Asano, and S. Noda, *Photon emission by nanocavity-enhanced quantum anti-Zeno effect in solid-state cavity quantum-electrodynamics*, Optics Express **16**, 18067 (2008). 76

[117] S. Hughes and P. Yao, *Theory of quantum light emission from a strongly-coupled single quantum dot photonic-crystal cavity system*, Optics Express **17**, 3322 (2009). 76

[118] K. Karrai, R. J. Warburton, C. Schulhauser, A. Hogele, B. Urbaszek, E. J. McGhee, A. O. Govorov, J. M. Garcia, B. D. Gerardot, and P. M. Petroff, *Hybridization of electronic states in quantum dots through photon emission*, Nature **427**, 135 (2004). 80

[119] A. Kiraz, S. Falt, C. Becher, B. Gayral, W. V. Schoenfeld, P. M. Petroff, L. Zhang, E. Hu, and A. Imamoglu, *Photon correlation spectroscopy of a single quantum dot*, Physical Review B **65**, 161303 (2002). 84, 86

[120] L. Besombes, K. Kheng, L. Marsal, and H. Mariette, *Acoustic phonon broadening mechanism in single quantum dot emission*, Physical Review B **63**, 155307 (2001). 88, 90, 91

[121] P. Borri, W. Langbein, S. Schneider, U. Woggon, R. L. Sellin, D. Ouyang, and D. Bimberg, *Ultralong Dephasing Time in InGaAs Quantum Dots*, Physical Review Letters **87**, 157401 (2001).

[122] E. A. Muljarov and R. Zimmermann, *Dephasing in Quantum Dots: Quadratic Coupling to Acoustic Phonons*, Physical Review Letters **93**, 237401 (2004).

[123] I. Favero, G. Cassabois, R. Ferreira, D. Darson, C. Voisin, J. Tignon, C. Delalande, G. Bastard, P. Roussignol, and J. M. Gerard, *Acoustic phonon sidebands in the emission line of single InAs/GaAs quantum dots*, Physical Review B **68**, 233301 (2003). 88

[124] G. Tarel and V. Savona, *Emission spectrum of a quantum dot embedded in a nanocavity*, physica status solidi (c) **6**, 902 (2009). 88

[125] B. Alen, F. Bickel, K. Karrai, R. J. Warburton, and P. M. Petroff, *Stark-shift modulation absorption spectroscopy of single quantum dots*, Applied Physics Letters **83**, 2235 (2003). 98

[126] K. Srinivasan, P. E. Barclay, and O. Painter, *Fabrication-tolerant high quality factor photonic crystal microcavities*, Optics Express **12**, 1458 (2004). 98

[127] I. Schuster, A. Kubanek, A. Fuhrmanek, T. Puppe, P. W. H. Pinkse, K. Murr, and G. Rempe, *Nonlinear spectroscopy of photons bound to one atom*, Nature Physics **4**, 382 (2008). 98

[128] M. T. Rakher, N. G. Stoltz, L. A. Coldren, P. M. Petroff, and D. Bouwmeester, *Externally Mode-Matched Cavity Quantum Electrodynamics with Charge-Tunable Quantum Dots*, Physical Review Letters **102**, 097403 (2009). 98

[129] M. W. McCutcheon, G. W. Rieger, I. W. Cheung, J. F. Young, D. Dalacu, S. Frederick, P. J. Poole, G. C. Aers, and R. L. Williams, *Resonant scattering and second-harmonic spectroscopy of planar photonic crystal microcavities*, Applied Physics Letters **87**, 221110 (2005). 100, 106

[130] I. Gerhardt, G. Wrigge, P. Bushev, G. Zumofen, M. Agio, R. Pfab, and V. Sandoghdar, *Strong Extinction of a Laser Beam by a Single Molecule*, Physical Review Letters **98**, 033601 (2007). 101, 106

[131] J. M. Fink, M. Goppl, M. Baur, R. Bianchetti, P. J. Leek, A. Blais, and A. Wallraff, *Climbing the Jaynes-Cummings ladder and observing its root n nonlinearity in a cavity QED system*, Nature **454**, 315 (2008). 110

[132] A. Faraon, I. Fushman, D. Englund, N. Stoltz, P. Petroff, and J. Vuckovic, *Coherent generation of non-classical light on a chip via photon-induced tunnelling and blockade*, Nature Physics **4**, 859 (2008). 110

[133] M. Toishi, D. Englund, A. Faraon, and J. Vuckovic, *High-brightness single photon source from a quantum dot in a directional-emission nanocavity*, arXiv:cond-mat/0904.1262 (2009). 110

[134] K. Srinivasan, P. E. Barclay, M. Borselli, and O. Painter, *Optical-fiber-based measurement of an ultrasmall volume high- Q photonic crystal microcavity*, Physical Review B **70**, 081306 (2004). 110

[135] P. Grangier, J. A. Levenson, and J.-P. Poizat, *Quantum non-demolition measurements in optics*, Nature **396**, 537 (1998). 110

List of Publications

1. K. Hennessy, A. Badolato, M. Winger, D. Gerace, M. Atatüre, S. Gulde, S. Fält, E. L. Hu, and A. Imamoğlu, *Quantum nature of a strongly coupled single quantum dot-cavity system*, Nature **445**, 896 (2007)
2. A. Högele, C. Galland, M. Winger, and A. Imamoğlu, *Photon antibunching in the photoluminescence spectra of a single carbon nanotube*, Physical Review Letters *100*, 217401 (2008).
3. M. Winger, A. Badolato, K. J. Hennessy, E. L. Hu, and A. Imamoğlu, *Quantum Dot Spectroscopy Using Cavity Quantum Electrodynamics*, Physical Review Letters **101**, 226808 (2008).
4. A. Badolato, M. Winger, K. J. Hennessy, E. L. Hu, and A. Imamoğlu, *Cavity QED effects with single quantum dots*, Comptes Rendus Physique **9**, 850 (2008).
5. M. Winger, T. Volz, G. Tarel, S. Portolan, A. Badolato, K. J. Hennessy, E. L. Hu, A. Beveratos, J. Finley, V. Savona, and A. Imamoglu, *Mesoscopic cavity-QED: the physics behind off-resonant cavity excitation by a single quantum dot*, submitted to Physical Review Letters (2009).

Acknowledgements

In my last year of undergraduate studies at ETH I signed up for a course on quantum information held by Ataç. Fascinated by what he presented, and by the way he did so, I decided to join his group for doing my diploma thesis and was lucky enough to get the opportunity to stay over for PhD. Now, in the end of this four-year endeavor I am looking back to an exciting period of learning loads of physics and technology, developing uncountable skills in the lab, meeting dozens of great people, and packing my backpack over and over again to travel the world for conferences and workshops. For giving me the opportunity to experience all this, I am greatly indebted to my supervisor Ataç Imamoğlu. His impassionate way of discussing physics together with his optimistic and positive attitude continuously managed to awaken my excitement, even when things weren't moving along well. I am also grateful to Ataç for creating a wonderful playground for me by giving me the opportunity to build and run my own lab. Thank you for giving me the freedom to independently follow my ideas, while still keeping up your continuous support in a benevolent and friendly way.

Certainly, any achievement in modern science is based on team-work, and hence my journey was greatly influenced by numerous colleagues and friends that turned the quantum photonics group not only into an inspiring scientific environment but also into a fun place to be. In "order of appearance" my thank goes first to Mete who introduced me to quantum dots, optics, and gypsy punk. Antonio was a great officemate over the years. Thank you for the great company on our sushi-trips in California and for putting me up at your place. Thank you Stephan/Timo for telling me absolutely *everything* about lasers and optics. The short period of interaction we've had in G8 gave me essentially all the skills I needed for my future experimental work. And thanks for all those endless chats and the great time we've had! Perk, you rocked! Your pragmatic and ever-motivated approach kept me going many times. Thanks for the trips to the gym, for teaching me proper L.A.-slang, for billions of Scoville-units, and for the quantum of craziness you added to the group. Thank you Dario for being the most awesome photonic-crystal-simulatramatron alive, for making me appreciate a good Sfogliatella, and for all the fun we've had here and on our legendary conference trip in 2007. Thank you Dora for providing sunshine in dark lab days and the exciting field trips in and around Zürich! Thank you Parisa for giving me the unique opportunity to discover the magic land of Persia. Thanks Andreas for surviving your diploma work and even being motivated for PhD in spite of being supervised by me. Thanks for your great work in the lab and for helping me keeping my *Vorarlbergerian* alive.

An extra big thank you goes to Thomas who joined this project at a later stage. It is not a coincidence that the time after he joined became the most productive and intense period of my PhD. In fact, it was your continuous support, both practically and mentally, that made this time both fruitful and a lot of fun. Thanks for proofreading this thesis and for calming me down when I was going furious when writing. Thank you too for those late-night ABBA&cookie sessions in G8, for listening to my lamentations about this and that and for being a great friend.

Finally, I want to thank all the other followers of Ataç — present and past — for doing their bit in making this group a great, open-minded, creative, and cheerful place.

Next, I would like to acknowledge Sandro Tiegermann and Hansruedi Scherrer from the physics department lab service team for their support in building a system that allows for ultimate command over photonic crystal cavity wavelengths.

Also outside ETH several people deserve a big thank you. My thanks goes to Oskar Painter and Kartik Srinivasan for hosting us twice at Caltech, for the insights into their work we were generously given and for the opportunity to catch a glimpse of life and work on another continent. Moreover, I want to thank Guillaume Tarel and Vincenzo Savona for the great collaboration we've had on the cavity feeding project. Guillaume, thanks for your great work and for those Megabytes of Skype-text we exchanged. Thank you, Vincenzo, for supporting this project and for co-examining my PhD.

Believe it or not, there is also life outside the lab! For making the latter pleasant and enjoyable I wish to thank all my friends here in Zürich. This includes my old combatants from undergrad (Martin/Hans, Fabian, Sebi, Emanuel, Philipp, etc...), the Gsibergerian crew (Robert, Marc, Dominik, Andi, and many more), and all the other great people that have influenced my ways.

Finally, I would like to express my deepest gratitude to my parents at this point who supported my ways from the very beginning with love and courtesy. Thank you for your invaluable support over all the years and for always being there and helping out wherever an whenever you could! And last but not least there is Angela, my long-standing soulmate and wife-to-be. Thank you for giving me confidence and cheering me up over and over again, for actually being really excited about what crazy physicists do, and for your wonderful friendship and priceless love.

Curriculum Vitae

Personal Details

Name	Martin Winger
Date of Birth	24th of September, 1982
Place of Birth	Feldkirch, Austria
Nationality	Austrian
email	wingerm@phys.ethz.ch

Education

1992-2000	Bundesgymnasium Bludenz
2000	Matura (high school diploma)
2000-2005	Undergraduate studies of physics at ETH Zürich
2005	Diploma in Physics. Diplomawork titled *Towards spin-flip Raman scattering in self-assembled quantum dots*
2005-2009	PhD student at ETH Zürich

Experience

Languages	German, English, French
Techniques	Spectroscopy techniques, optical microscopy, cryogenics and vacuum, lasers, electronics, atomic force microscopy
Programming	Matlab, Mathematica, LabVIEW

October 2, 2009

List of Figures

2.1. The basic system of cavity QED . . . 6
2.2. System eigenstates on resonance . . . 8
2.3. Simulated PL spectra in the weak and the strong coupling regimes . . . 10
2.4. QD level scheme . . . 11
2.5. SK growth . . . 12
2.6. QD level structure . . . 13
2.7. X^0 level scheme . . . 16
2.8. XX^0 level scheme . . . 17
2.9. SEM picture of different types of microcavities . . . 19
2.10. Triangular-lattice photonic crystal . . . 20
2.11. The L3 microcavity . . . 22
2.12. Cavity fabrication procedure . . . 23

3.1. Photoluminescence spectroscopy . . . 26
3.2. A typical PL setup . . . 26
3.3. PL spectrum of a single QD . . . 28
3.4. PL pump power dependence . . . 29
3.5. TCSPC measurement on a QD neutral exciton . . . 30
3.6. Hanbury-Brown–Twiss Setup . . . 32
3.7. X^0 auto-correlation . . . 33
3.8. XX^0–X^0 cross-correlation measurement . . . 34
3.9. The grating spectrometer . . . 37
3.10. Setup for photon cross-correlation measurements . . . 38

4.1. Signature of a buried QD on the sample surface . . . 40
4.2. PL micrographs in different density regions of a QD sample . . . 41
4.3. Microscope image of gold markers . . . 42
4.4. AFM height trace used for QD mapping . . . 43
4.5. Technical issues relevant for the AFM-mapping procedure . . . 44
4.6. Results of active cavity positioning . . . 45
4.7. Digital etching of a PC cavity . . . 47
4.8. Cavity tuning by gas adsorption . . . 48

5.1. A QD-cavity device . . . 51
5.2. PL spectra of the QD-cavity device . . . 52
5.3. Observation of vacuum Rabi splitting . . . 54
5.4. Observation of lifetime reduction . . . 56
5.5. Measured auto-correlation of the strongly coupled system . . . 58
5.6. Spectral filtering of a single polariton . . . 59

6.1. Typical PL spectrum . . . 62

6.2. Strong-coupling anticrossing curves for different QD lines. 63
6.3. The cavity mode interacting with the X^0 64
6.4. Comparison of X^0 dynamics for different emission polarization 65
6.5. Anticrossings for a device with cavity-X^0 angular misalignment . . . 69

7.1. PL spectra showing cavity feeding 72
7.2. QD-cavity cross-correlation measurement 74
7.3. Auto-correlation measurement of cavity PL 76
7.4. Device PL showing significant QD background emission 77
7.5. Pump power dependence of photoluminescence 78
7.6. Pump power dependence of higher QD shells 79
7.8. Coupling mechanisms between multi-exciton states 80
7.7. Calculated level spectrum of a QD 80
7.9. Joint density of states for different manifold transitions 82
7.10. Monte-Carlo random-walk simulation of the QD-cavity system 83
7.11. Theoretical and experimental cavity-X^0 cross-correlation curves . . . 85
7.12. Experimental and theoretical cavity auto-correlation curves 86
7.13. Photon correlations for different pump powers 87
7.14. Cavity feeding mediated by LA-phonons 88
7.15. PL spectra when tuning the cavity across resonance with QD excitons 89
7.16. Cavity and X^0 line intensities as a function of cavity wavelength . . . 89
7.17. Lifetime of the X^0 as a function of cavity detuning 90
7.18. Pump power dependence in the LA-phonon feeding regime 92
7.19. Lifetime of the X^{1+} as a function of cavity detuning 93
7.20. Photon correlations in the LA-phonon feeding regime 95

8.1. Reflection spectrum of an L3 cavity 99
8.2. Resonant scattering using a crossed-polarization scheme 101
8.3. Resonant scattering scan of vacuum Rabi splitting 102
8.4. Single RS traces in strong coupling with the X^0 and the X^{1+} 103
8.5. RS power dependence of the uncoupled cavity peak 105
8.6. Broadband reflectivity spectrum of an L3 cavity 106
8.7. Broadband RS of vacuum Rabi splitting 107

A.1. Schematic of the confocal microscopy setup . . . . B

Index

Q factor, 8
V_{eff}, 6
XX^0, 17, 28
  entanglement, 17
  polarization correlation, 17
X^0, 15, 28
  fine structure, 16
X^{1+}, 18, 28
X^{1-}, 18, 28
N_2 tuning, 49

abbreviations, xi
AFM, 41
analyzer, 100
angle correction, 44
antibunching
  definition, 31
APD, 30
  operation principle, 38
artificial atom, 11
avalanche photodiode, 30

bandgap, 27
bandgap energies, 11
biexciton, 17, 28
Bloch-theorem, 21
broadband RS, 106

cavity draining, 72
cavity feeding, 53, 71
cavity QED, 5
  definition, 1
  theory, 5
citric acid, 46
cross-correlation
  XX^0–X^0, 33
  QD-cavity, 74
cryostat window, 48

dephasing, 9
deterministic coupling, 40
digital etching, 46
dopants, 27

elastic strain relaxation, 11
electric field operator, 6
exchange interaction, 16

FDTD, 22
fine structure
  investigation, 61

gas adsorption, 47

H1 cavity, 21
HBT, 31

intensity correlation function, 31

Jaynes-Cummings Hamiltonian, 6
  eigenstates, 7

L3 cavity, 21
lattice misfit, 11
lifetime measurement, 29
lithographic tuning, 43
LO phonons, 27
luminescence, 25
luminescence decay curve, 30
Luttinger Hamiltonian, 14

master equation, 8
methods, 25
microcavity, 2
microdisc, 19
microdisk, 2
micropillar, 2, 19
mode volume, 6
mode walking, 47
molecular beam epitaxy, 12

neutral exciton, 15, 28

PC cavities, 18

PCI-growth, 12
Perk, 44
phonon bottleneck, 27
photoluminescence, 25
    power dependence, 29
    principle, 25
    scheme, 26
    spectrum, 27
photon blockade, 57
photonic bandgap, 21
    lifetime enhancement, 56
photonic crystal
    natural, 20
photonic crystal defect cavities
    overview, 18
piezoelectric field, 17
PL, 25
PL micrograph, 36, 41
polariton, 54
    definition, 7
polaron-effect, 27
Purcell effect, 9
    figure of merit, 9
    regime, 9

QD, 2
quality factor, 8
quantum dot
    landmark experiments, 2
quantum dots
    growth, 11
    overview, 11

resonant scattering, 25, 97
RHEED, 12
RS, 97

S1 cavity, 21
SEM, 40, 41
Setup
    Details, A
stacking, 40
Stranski-Krastanow growth, 11
strong coupling, 8, 10
    figure of merit, 11
    observation, 51
strong coupling regime
    definition, 10
sub-Poissonian statistics, 31

TAC, 38
TCSPC, 29
time-correlated single photon counting, 29
time-to-amplitude converter, 38
trion, 17, 28

vacuum Rabi splitting
    anticrossing, 7
    definition, 7

weak coupling, 8
    definition, 9
wetting layer, 11
whispering gallery mode, 19

x-y splitting, 16